

INTEGRATED PIEZOELECTRIC TRANSDUCER ARRAYS FOR ON CHIP
COMMUNICATION AND SENSING

A Dissertation

Presented to the Faculty of the Graduate School

of Cornell University

In Partial Fulfillment of the Requirements for the Degree of

Doctor of Philosophy

by

Jason Thomas Hoople

May 2016

© 2016 JASON THOMAS HOOPLE

INTEGRATED PIEZOELECTRIC TRANSDUCER ARRAYS FOR ON CHIP
COMMUNICATION AND SENSING

JASON THOMAS HOOPLE, Ph. D.

Cornell University 2016

Most modern computer systems are fabricated using CMOS technologies. These systems utilize metal wire interconnects to communicate between different computational blocks. As these systems scale to smaller critical dimensions, new technologies are needed to increase computational power and efficiency as well as overall system capability. Moore's Law, an observational rule which states that the number of integrated transistors on chip doubles every 18 months, has long been responsible for these advancements in computer systems. Revolutionary new technologies could allow for an increase in computer systems with so called "More than Moore" improvements to system functionality and performance.

This dissertation presents a novel integrated CMOS technology for generating, and sensing ultrasonic waves in the silicon substrate of CMOS chips. The technology advancement which has made such a system possible is the advent of CMOS compatible piezoelectric materials, specifically aluminum nitride. Thin film ultrasonic piezoelectric transducers are fabricated on silicon and used to generate and detect ultrasonic waves at frequencies in the 1-3 GHz range.

One application for this technology is a novel communication pathway for CMOS circuits which uses the silicon substrate as a channel for which to communicate data to another physical location on the chip. The speed of sound in silicon (~8433 m/s) results in ultrasonic wavelengths in the range of 10 μm to 1 μm (1 GHz to 10 GHz), allowing for the use of far field communication techniques such as phased arrays for

software reconfigurable channels. Ultrasonic waves are modulated at a frequency of 2.7 GHz and used to communicate at a data rate of 120 megabits per second.

An additional application of this system is a measurement system which can be used to characterize the ultrasonic properties of various materials. Such a system is developed to measure a human fingerprint. When an ultrasonic wave reflects off of the silicon surface the amplitude and phase depends on the material on the other side. Measurements conducted showed signal levels of 700 μV at the valley of a fingerprint and on the order of 300-400 μV at a fingerprint ridge ridge, showing a measureable contrast which could be used to image a fingerprint.

BIOGRAPHICAL SKETCH

Jason Hoople was born on June 11th 1986 in Ithaca, New York. His father, Christopher Hoople was a graduate student in Electrical and Computer Engineering at Cornell University at the time. He spent most of his formative years in Irondequoit, a suburb of Rochester NY, the eldest of three children. At a young age he showed his hints at his future career in electrical engineering by tearing apart any electrical device which no longer worked properly. After graduating from West Irondequoit High School in 2004, he started at Rochester Institute of Technology (RIT) in the Electrical Engineering program. He graduated from RIT in 2009 with both a Bachelor's and a Master's degree in Electrical Engineering. In 2010 he began his doctoral education under the supervision of Prof. Amit Lal. He has since been researching the use of integrated gigahertz frequency piezoelectric transducers with CMOS for sensing and communication applications.

To My Mother and Father

ACKNOWLEDGMENTS

I would like to acknowledge the many graduate students who have been a part of SonicMEMS in my tenure including; Kwame Amponsah, Ching-Ping Janet Shen, Yue Shi, Hadi Housseinzadegan, Venkata Siva Prasad Pulla, Sarvani Piratla, Yuerui “Larry” Lu, Ved Vishwas Gund, Sachin Prakash Nadig, Visarute “Earth” Pinrod, Tiffany St. Bernard, Mamdouh Osmam Mahmoud Mohamed Abdelmejeed, and Leanna Pancoast. A special thank you to the Po-Chen Cheng, my co-conspirator and gym buddy. Additionally a special thanks is in order for Justin Kuo, the Robin to my Batman, I may have been able to do it without you, but you certainly made it much easier. Additionally special recognition goes to Serhan Mehmet Ardanuç, for keeping me calm and functional through the tough times. Outside of SonicMEMS, I would like to thank Rose Agger and Hazal Yüksel, Tanay Gosavi, Bob Bell and Phil Gordan.

I would also like to acknowledge Scott Coldren, Sue Bulkley and Daniel Richter for their patience and help through the stressful times. Of course I mustn't forget the incomparable Patty Gonyea.

Perhaps the most important person to acknowledge in my development here would be my academic advisor, Prof. Amit Lal. Though we may have our differences, I cannot ignore how much I have learned and grown under your tutelage. I really do appreciate everything that you have done and all the ways that you have helped me in this journey. If nothing else, I have a lifetime of amazing stories about what it was to be your graduate student. I would also like to extend my gratitude to my committee members, Prof. Clifford Pollock and Prof. Alyosha Molnar for all the support, advice and assistance through the stressful times.

Additional thanks to the funding agencies, the IARPA TIC program. With special thanks to Dr. Dennis Polla and Dr. Carl McCants, the program managers. In addition I would like to acknowledge the help from Dr. Troy Olsson when he was at Sandia

National Labs with the aluminum nitride process, and Dr. Ron Polcawich at Army Research Lab with the thin film PZT process.

Finally, I would like to thank my family, for my mom and dad and siblings for their unwavering love and support. I would also like to acknowledge my extended family, including my Aunt Carol and Uncle Martin and cousins Ashley and Jenna, as well my Uncle Joe and Aunt Anne and cousins Andy and Amy, and my Uncle Mike.

Table of Contents

Chapter 1	1
1.1 On chip communication and security	1
1.2 Metal Wire Interconnects	3
1.3 Optical Interconnects.....	5
1.4 On Chip RF Interconnects	7
1.5 Ultrasonic Interconnects	8
1.6 History of Electronically Controlled Ultrasonics	9
1.7 Chip obfuscation.....	15
1.8 Dissertation Scope	17
Chapter 2	19
2.1 Introduction to Ultrasound and Nomenclature	19
2.2 Acoustic waves in silicon	19
2.3 Wave equation for elastic solids.....	21
2.4 Acoustic Impedance	24
2.5 Material Boundary Conditions	26
2.6 Acoustic Losses	28
Chapter 3	32
3.1 Piezoelectric Materials	33
3.2 Piezoelectric Transducers.....	36
3.3 Thin Film Bulk Acoustic Resonators (FBAR)	41
3.4 Highly Overtone Bulk Acoustic Resonator	43

3.5 Transducer Power Transfer	45
3.6 KLM Model.....	57
3.7 Transducer Noise Figure	69
Chapter 4	74
4.1 Radiation Impedance	75
4.2 Transducer Radiation Pattern	78
4.3 Array Factor.....	89
Chapter 5	96
5.1 Introduction	96
5.2 Ultrasonic Communication Link Budget.....	98
5.3 Transducers.....	103
5.4 Single Transducer Pair Communication Channel	104
5.5 Phased Array Communication Channel	109
5.6 Conclusions and Future Work	112
Chapter 6	113
6.1 Introduction	113
6.2 Integrated Circuits	114
6.2.1 Receiver Amplifier	115
6.2.2 Phase Rotator.....	123
6.3 Sandia 350nm Tapeout Layout and Experimental Results.....	130
Chapter 7	133

7.1 Proposed System	136
7.2 Transducers Layout	138
7.3 Theory of Operation	140
7.4 Experimental Setup	143
7.5 Experimental Results.....	146
7.6 Conclusion and Future Work.....	148
Chapter 8	149
8.1 Piezoelectric Polymer Transducers	149
Chapter 9	155
Chapter 10 References.....	170

LIST OF FIGURES

Figure 1.1: Integrated optical interconnects, waveguides are implemented and defined lithographically [23]	5
Figure 1.2: Galton's whistle, one of the first devices used to generate ultrasound waves. It was used for testing human hearing ranges, and as a training tool for dogs [36].	9
Figure 1.3: Illustration of the piezoelectric effect. (a) The direct piezoelectric effect, a strain on the piezoelectric material generates a charge between the two plate (b) A charge applied to the two plates generates a strain within the material	10
Figure 1.4: Ultrasonic digital delay line memory, utilized in the UNIVAC-I computer system [9]	12
Figure 2.1: Illustration of the two different wave types for elastic solids. (a) Unperturbed one-dimenisonal elastic material (b) Longitudinal wave (c) shear wave	20
Figure 2.2: Illustration of a compressional wave traveling through an elastic material	21
Figure 2.3: Illustration of an acoustic boundary between two materials. The arrows with T represent a stress wave travelling the regions. Z_{01} and Z_{02} are the acoustic impedance in each region. β_1 and β_2 are the wavenumbers in each region.	26
Figure 2.4: Acoustic Loss in silicon as a function of frequency.	31
Figure 3.1: Illustration of piezoelectric transducer model, the system is modeled as a three port device, two acoustic ports representing each face of the transducer and one electric port.....	36
Figure 3.2 Electrical input impedance of an AlN FBAR	41
Figure 3.3 Electrical input impedance of an AlN HBAR on a silicon substrate	44
Figure 3.4: Expanded view of the FBAR and HBAR input impedances near the fundamental resonance peak of the transducer.....	44
Figure 3.5: Input impedance for microsonar transducer.....	47
Figure 3.6: Driving Setup	48
Figure 3.7 Value of $H(\pi f / f_0)$ normalized to the value at the resonance frequency f_0 , the legend shows which curve corresponds to different ηr	50

Figure 3.8: Center frequency of the impedance response with respect to impedance ratio.....	51
Figure 3.9: Maximum value of $H(\beta_{al})$ as a function of the ratio of Z_2 and Z_C	52
Figure 3.10: Bandwidth of $H(\pi f / f_0)$	53
Figure 3.11: Performance metrics of power conversion as a function of impedance ratio η_r , (a) Center Frequency (b) peak value of the response (c) Bandwidth, taken as the half power point (d) Product of the peak value and the bandwidth.....	54
Figure 3.12 Performance metrics of power conversion as a function of coupling efficiency k_t , (a) Center Frequency (b) peak value of the response (c) Bandwidth, taken as the half power point (d) Product of the peak value and the bandwidth.....	55
Figure 3.13: Mason and Redwood models	57
Figure 3.14 KLM Model	58
Figure 3.15: Wave generation from transducer	59
Figure 3.16: ABCD representation of the transducer in transmission.....	60
Figure 3.17: ABCD representation of transducer under receive	61
Figure 3.18: Ideal transducer magnitude response function.....	62
Figure 3.19: Transducer cross section with annotated thickness ranges for design space	63
Figure 3.20: Effect of AlN film thickness on transfer function.....	64
Figure 3.21: Effect of the silicon dioxide backing layer	65
Figure 3.22: Effect of the top Mo electrode	65
Figure 3.23: Effect of bottom silicon dioxide layer	66
Figure 3.24: Effect of bottom electrode layer	66
Figure 3.25: Simulation of full stack sweeping bottom oxide layer.....	68
Figure 3.26: Measured acoustic communication channel magnitude response of designed stack.....	69
Figure 4.1: Power factor of Equation (4.7) as a function of radius normalized to wavelength λ	77

Figure 4.2: Setup for Green’s Function method	79
Figure 4.3: Point sources representing the method of images.....	81
Figure 4.4: Plots of radiation pattern at different distances from the transducer	84
Figure 4.5: Plot of on axis value of intensity from radiation pattern of a circle	85
Figure 4.6: Diffraction loss as a function of distance S	87
Figure 4.7: Radiation pattern of a transducer (or multiple transducers).....	88
Figure 4.8: Phased array system setup, the effect of the array at the target point is determined by superposition of the elements in the array	89
Figure 4.9: Array factors for N = 5 elements, varying spacing between elements	92
Figure 4.10: Array factors for $\lambda/2$ spacing, varying the number of elements in the array	93
Figure 5.1: Conversion loss figure	100
Figure 5.2: BER plot.....	102
Figure 5.3: Transducer Cross section	103
Figure 5.4: Optical image of the AlN transducer array	104
Figure 5.5: PZFlex FEA Sims	104
Figure 5.6: Pulse Echo measurements, comparison with simulation	106
Figure 5.7: Single transducer pair communication channel demonstrating 7 Mbits/second. The red-channel is the receive voltage, and the blue channel is the input bit stream to the RF switch.....	107
Figure 5.8: Communication channel frequency response – calculated response compared to measured response.....	108
Figure 5.9: SONAR Die and PCB	109
Figure 5.10: Transmit Circuit.....	110
Figure 5.11: Phasing Plots	111
Figure 5.12: Sample time capture of phasing plots	111

Figure 6.1: Inverter Based Receiver LNA. The feedback resistor biases the inverter in the active gain region.....	116
Figure 6.2: Sketch of the voltage transfer characteristic of a CMOS inverter. The highlighted red region is the region of high gain.....	116
Figure 6.3: Small signal model for double g_m inverter amplifier	117
Figure 6.4: Schematic for the receiver in 65 nm technology node	120
Figure 6.5: Simulated Voltage Magnitude Transfer for 65 nm Amplifier	121
Figure 6.6: Frequency response of 65 nm receiver amplifier.....	121
Figure 6.7: Schematic of 350 nm Amplifier.....	122
Figure 6.8: Frequency Response of the 350 nm receive amplifier.....	123
Figure 6.9: Circuit Schematic of the Phase Rotator Transmit Circuit.....	124
Figure 6.10: Schematic for 4-Bit differential current DAC	126
Figure 6.11: Flip Flops for local quadrature clock generation	127
Figure 6.12: Phase rotator output phase as a set by a 6-bit phase DAC.....	128
Figure 6.13: Measurement Results of 28 nm Phase Rotator over a single quadrant..	128
Figure 6.14: Results from 28 nm phase rotator	129
Figure 6.15: Transducer location with integrated amplifier	131
Figure 6.16: Frequency Transfer Characteristic of the 1-D Channel with integrated amplifier	132
Figure 7.1: Cross section of skin surface layer.....	134
Figure 7.2: Proposed integrated CMOS and Ultrasonic Transducers. The pulses are reflected off the back surface of the silicon chip and the phase and amplitude of the reflected signals are related to the material on the other side.....	137
Figure 7.3: Cross section for piezoelectric transducers	139
Figure 7.4: Optical capture of array of square transducers.....	139
Figure 7.5: Line array of transducers for finger swipe fingerprint reader	140

Figure 7.6: Frequency dependence of the reflection coefficient when loss is taken into consideration.....	143
Figure 7.7: Illustration of experiment setup, where a rubber fingerprint phantom is attached to a mechanical manipulator and scanned across the sensitive area on the back of the silicon chip.....	144
Figure 7.8: Schematic of 16 pixel fingerprint interrogation system.....	145
Figure 7.9: Circuit setup for finger print swipe setup	145
Figure 7.10: Results of fingerprint mechanical scan	146
Figure 7.11: Frequency dependent result reflection coefficient for 3 different materials	147
Figure 7.12: Frequency scans of reflection co-efficients for different fruits showing different frequency dependent behavior	147
Figure 8.1: PVDF-TrFE spin coat samples. Left image is spun at 1000 rpm for 30 s. Right sample is spun at 2000 rpm for 120s	150
Figure 8.2: Transducer surface with wire bond marks left. These show how the bonder pressed against the film to create these pits.....	151
Figure 8.3: Transducers fabricated with bond sites away from the PVDF-TrFE layer	152
Figure 8.4: Process flow for PVDF-TrFE Transducers.....	153
Figure 8.5: Pulse echo response fabricated transducers	154

LIST OF TABLES

Table 2.1: Summary acoustic properties of common CMOS materials.....	25
Table 3.1: Dimensional units of the piezoelectric coefficients	34
Table 3.2: Summary of common piezoelectric material properties.....	36

Chapter 1

INTRODUCTION

1.1 *On chip communication and security*

The current era in history is often referred to as the information age, brought about by the advent of CMOS microchips that are vehicles for computation and communication. Early computational devices were limited by the performance of switches used for Boolean logic, motivating research into smaller, faster and lower power transistors. Just as important as the transistors themselves is the performance of communication channels between devices. The performance of any computational action, depends on how quickly information can be moved to it and how quickly it can pass the result on. The connection between the processor and memory has long been recognized as a limit to the performance of computer systems [1]. This is exemplified in Amdahl's Law, where the peak performance of a parallel system is limited by operations which cannot be parallelized, such as access to the memory [2]. As the performance of transistors have improved over the past six decades the overall system performance no longer depends on the individual transistor but is instead limited by the communication pathways made of metal interconnects [3] - [8].

The technologies enabling the information age, computers, wireless devices and the internet, have allowed for unprecedented sharing of information globally. This has led to globalization of nearly everything, including semiconductor device manufacturing. While much of the computer systems utilizing transistors were pioneered in the United States, with companies such as Bell Labs, Texas Instruments and Intel; in the past 10-20 years a great deal of semiconductor manufacturing has been developed in foreign countries. Some of these sites are deemed untrusted, and as

such CMOS designs which are sensitive to U.S. security cannot be fabricated there. The two biggest risks are that a potential enemy can (1) copy designs and (2) tamper with designs. These modified chips if used in Department of Defense (DoD) systems may lead to early malfunction. Furthermore after chips are fabricated and in use there are scenarios where sensitive information on chip needs to be protected from hackers or other parties to which data should not be given to.

This thesis puts forth a novel methodology for on chip communication and sensing using integrated piezoelectric transducers to generate and detect ultrasonic pulses in the chip substrate. As a transmitter, thin film piezoelectric transducers can operate at high frequencies of 1 – 10 GHz, allowing for high throughput channels. Silicon is a single crystal material, as such it has very low acoustic loss allowing for low power communication links. Since, the speed of sound in silicon is on the order of 10,000 m/s, therefore the wavelength of sound is in the 1-10 μm range. The silicon ultrasound channel with thickness much greater than wavelength can be treated as the far field. Far field operation enables the implementation of phased arrays for reconfigurable channels. These links can be programmed and can disappear without power to the chip. The acoustic channels can hide communication links such that hardware copying of the circuits does not produce an operating chip.

The remainder of this chapter explores the origin of on chip communication problems in more depth. First the origin of the problem with metal interconnects will be examined, along with limitations of interconnects and the reasons for their prevalence. Two alternative technologies have already been explored, optical waveguide interconnects and near field on chip RF wireless interconnects which will be introduced and compared here. The technologies enabling on chip ultrasonic communication links will be introduced. Finally, the problems associated with security in untrusted foundries will be examined and ultrasonic links as a potential solution.

1.2 *Metal Wire Interconnects*

The first “wiring problem” involved the complexity of connecting a large number of components together. The first computers and electronic circuits utilized vacuum tubes which are large, consume great amounts of power, fragile, and subject to manufacturing variability. Even with vacuum tube system, such as the UNIVAC [9] a large number of wires are needed to connect the components usually consisting of physical wires. As the active unit, the transistor [10] greatly reduced the size, power and manufacturing reliability, compared to vacuum tube, but; it only exaggerated the wiring problem since the density of elements increased.

A big breakthrough in solving this problem was when Jack Kilby presented the first “Chip” in 1958 [11]. Kilby had fabricated a simple oscillator circuit, where all components, transistors and passive elements were fabricated on a single piece of germanium, but they still used hand soldered wires for connections. Parallel to this, Jean Hoerni had developed a process for protecting sensitive bipolar devices by coating them with silicon dioxide [12]. This inspired Robert Noyce to develop and patent the idea for planar, monolithic processing [13]. This was the birth of the integrated circuit, and this manufacturing method has been iterated and improved upon to this day with transistor counts approaching 1 Billion with even greater number of wires connecting the transistors using 7-8 layers of interconnect wires.

With rapid advances in active device density it was not long until the wired interconnects became a source of bandwidth limits to system performance. As wires and discrete components shrunk in physical size, the capacitance between elements and the resistance of metal traces, even at the circuit board level were increasing. Wires were no longer “free” and needed to be considered in optimal design [14], when trying to operate circuits at the highest possible speed. As the integrated circuit

technology matured, the integrated circuit itself became a subject of study. As early as 1974, the trend in transistor size and performance having already been established [15], the effect of wire delay on performance was being studied [16]. Later the trends between device performance and interconnect performance were compared and it was found that the delays due to gates were shrinking faster than the delays due to interconnects [4]. At this point though, the system delay was still dominated by device delay.

The basic unit used in these computing systems is the transistor, which is an electrical device, operated by electrical charge, current, and voltage. In order to connect two devices together, the only option is a metal wire. It is this fact, that a lot of research was placed on reducing the resistivity of the metals used for planar processes (resistance) as well as the dielectric constant for the inter metal isolation dielectric (capacitance), but into the 1990s these efforts would encounter fundamental limits [6]. Furthermore a limit on the bit rate capacity of a metal trace was determined based on the aspect ratio of the wires $B \sim B_0 A/l^2$, where B is the maximum bit rate, B_0 is approximately 10^{15} bits per second, A is the cross sectional area of the metal wire and l is the wire length [17].

Modern understanding of the performance limit to metal wire interconnects was brought about by the observation that chip designs were dominated by short, local wiring. The local wire interconnects do scale with size, since the smaller transistors can be placed closer together [7] [8] [18]. Furthermore, through the TIC program it was simulated that a 28 nm front end with 45 nm back end resulted in the system performance of a 45 nm system [19]. This placed the focus of the limitation of interconnects on system performance onto long interconnects of the system, which are traditionally buffered with repeaters through the system. Additionally multicore systems, and nodes in network on chips systems, require long wire interconnects,

recognize these long wires as the limit in overall system performance [20]. A popular target of these alternative connections is the clock signal, since it requires precise timing to each element and is carried throughout most of the chip.

1.3 *Optical Interconnects*

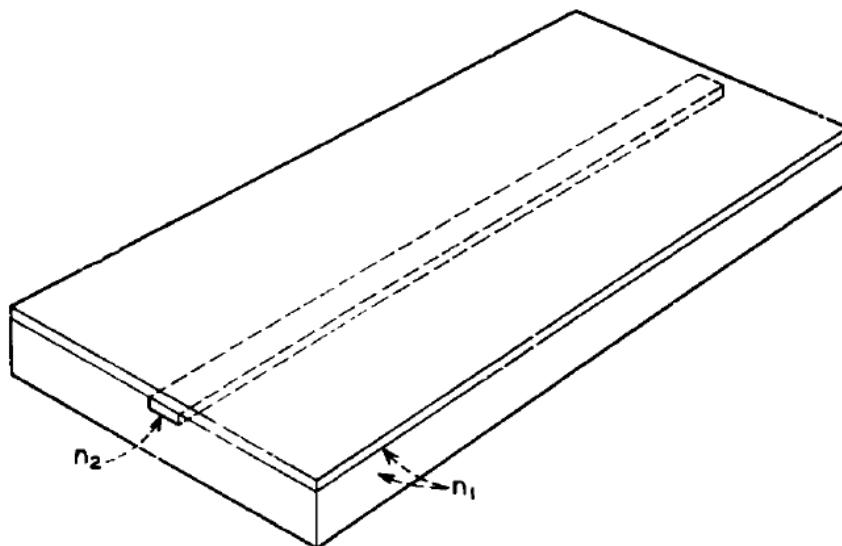


Figure 1.1: Integrated optical interconnects, waveguides are implemented and defined lithographically [23]

A popular proposal for the supplementing or replacing wired interconnects on chip is the use of optical waveguides. The first laser [21] had a wavelength of 694.3 nm, which corresponds to an operating frequency of approximately 432 THz. This means that if a fractional bandwidth of only a 0.2% could be obtained than the resulting bandwidth would be a 1 THz which is much greater than possible with wires. The problem with adopting optics at the time of the lasers invention, is that fiber optic fibers, had attenuations on the order of 1000 dB/km. It was the work of Nobel prize winner Charles C. Kao, who established the theory for light attenuation in fiber optic

cables which resulted in a theoretical lower limit of less than 20 dB/km. It was the introduction of the laser, and the theory behind fiber optic attenuation which sparked the modern telecommunications development [22]. It is these properties of an optical signal communication connection, near infinite bandwidth, and loss nearly independent of length (especially at chip scale) which strongly motivates the use of on-chip optics instead of on chip wiring.

The idea of integrating photonic waveguides on smaller substrates began shortly after the advent of the laser. First the idea was proposed for use at a printed circuit board level, creating a highly integrated system with the laser for a plethora of applications [23]. It was a seminal paper by Joseph W. Goodman, which proposed optics as a complementary form of on chip communication [3]. He showed ways in which fiber optic or integrated wave guides could complement system function as a clock distribution or other global signals.

There are many additional benefits for use of optical interconnects on chip [24]-[26]. Optical interconnects are immune to crosstalk and electromagnetic interference, an argument which many believe is strong for the use of optics, but is difficult to quantify [24]. Optics does not have an equivalent to inductance and the design troubles that inductance adds to electrical interconnects. Wave reflection and impedance matching are trivial in optics compared to electrical matching techniques.

Even with the reported benefits offered by optical interconnects, they have failed to supplant traditional interconnects on-chip. One of the biggest shortcomings is the lack of an optical switch, which preforms as well as the transistor, in terms of size, speed, and energy efficiency. Since metal wire interconnects performance depends on the length of the wire, it stands to reason that there is some length over which wire interconnects offer superior performance to optical. The location of this cross over point is on the order of multiple centimeters to meters, which is greater than integrated

chip lengths [27]. This limit may be brought to lower lengths with the introduction of better optic components, such as optical sources on chip. But while the theoretical performance has always been promising the on-chip optics technology continues to lack necessary advancements in integrating on chip components, to compete with status-quo CMOS and metal interconnects [24].

1.4 *On Chip RF Interconnects*

Another technology to supplement wired interconnects is RF on-chip pulses. An early paper on RF communication is [28] proposed using a multi-chip module with an RF microstrip transmission line or coplanar waveguide nearby, or even free space pulse propagation to act as a bus for multiple chips, or multiple cores in the same chip to communicate over. While at first, it may seem like a non-solution, in that it requires a transmission line, which is itself a metal interconnect, since it is physically larger and part of the packaging it is possible to design a very low loss LC transmission line while on chip wired interconnects behave as a distributed RC network. The preference of the transmission line compared to free space is in confining the electromagnetic field and thereby reducing losses to the ambient.

This idea can be further expanded to utilize both baseband and RF-signaling techniques across CMOS channels to improve throughput [29]. While research is progressing in the RF interconnect field [30] [31], there are a few problems which have so far been difficult to overcome in making them ubiquitous. Even though the transmission line itself is low loss, by using it as a bus, discontinuities along the channel from multi access points greatly degrade signals [29]. Furthermore the silicon substrate itself is usually doped and conductive loss due to proximity to transmit and receive elements further degrades signal quality. Attempts have been made to put

these LC transmission lines on chip [31], however it is still difficult to deal with large silicon conductive losses.

1.5 *Ultrasonic Interconnects*

Ultrasonic wave propagation offers a potential additional information channel for advanced ULSI systems. (1) Since the speed of sound is much slower than the speed of light, ultrasound propagating in the silicon wafer can be viewed as a far-field phenomenon at high enough frequencies (i.e. Greater than 100 MHz). It is possible to use far field RF wave-front forming techniques, used for electromagnetic waves in free space and apply it to ultrasound in the silicon wafer. One of the most interesting of these is phased array beam-forming, a technique used in Radio Detection and Ranging (RADAR) and at much lower frequencies in traditional Sound Navigation and Ranging (SONAR), where the communication channel could be reconfigured electronically to different physical locations in the system. (2) Since silicon is a single crystal material with very few dislocations, the ultrasonic loss is small. Typical loss is 5 dB/mm at 10 GHz, and especially for on-chip distances it is competitive with wired interconnects, in terms of bandwidth and energy per bit. This last statement is proven in this thesis.

This thesis demonstrates ultrasonic interconnects in CMOS with thin film piezoelectric transducers. (1) Advances in thin film piezoelectric materials and devices have resulted in transducers capable of operation at GHz frequencies. (2) Modern CMOS nodes of 28 nm and 14 nm are small enough that it is possible to build transmit and receive circuits which fit underneath piezoelectric transducers. (3) Any technology hoping to compete or supplement CMOS must use materials and processes which are compatible with CMOS manufacturing. Aluminum nitride transducers have been fabricated on CMOS in the past [32] and the technology is being adapted at foundries.

What follows is a brief history of the developments that are the foundation of ultrasonic communication links.

1.6 *History of Electronically Controlled Ultrasonics*



Figure 1.2: Galton's whistle, one of the first devices used to generate ultrasound waves. It was used for testing human hearing ranges, and as a training tool for dogs [36].

Since ultrasound is by definition sound at frequencies higher than can be heard, there was little interest in studying it, as there was no application through much of human history. In 1883 Dr. Francis Galton published “Inquiries into Human Faculty and its development” a small section of which focused on testing the limits of human hearing [33]. Dr. Galton developed what effectively was a slide whistle which could go to the threshold of human hearing and above. A sample can be seen in Figure 1.2. He utilized this to characterize an individual’s range of hearing and amused himself with testing the limits of animals as well. One of the seminal works in the scientific study of sound was “The Theory of Sound” by John William Strutt, 3rd Baron

Rayleigh [34], where he detailed a rigorous mathematical treatment of sound waves. A small section was dedicated to experiments with sound above the audible range using a “sensitive-flame” to visualize the effects. This “sensitive-flame” developed into a teaching tool which could be used to teach students wave phenomenon such as reflection, interference, standing waves and measuring wavelengths [35].

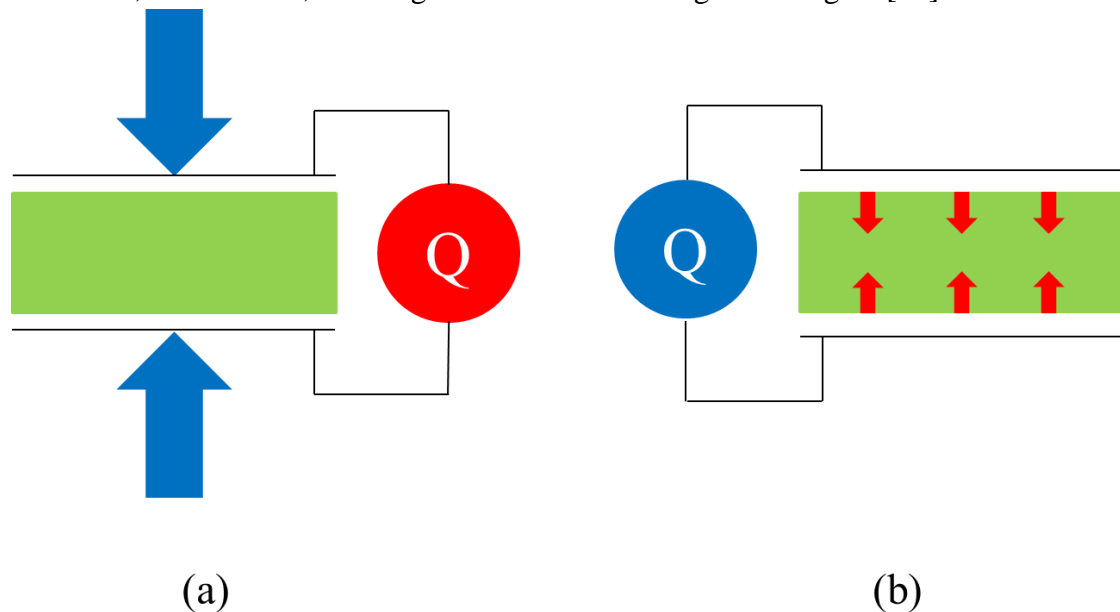


Figure 1.3: Illustration of the piezoelectric effect. (a) The direct piezoelectric effect, a strain on the piezoelectric material generates a charge between the two plate (b) A charge applied to the two plates generates a strain within the material

Around this same time Pierre and Jacques Curie discovered piezoelectricity. In 1880 they published work on the discovery that certain crystal materials would generate charge with the application of a strain, known as the direct piezoelectric effect [37]. Gabriel Lipman, realized from the Curie’s work, published the theory of the inverse piezoelectric effect based on thermodynamics [38]. Upon this revelation the Curie’s were able to immediately confirm the existence of such an effect [39]. This

effect was studied extensively over the next 30 years culminating in the publication of Woldemar Voigt's text on crystallography [40].

During World War I, significant military research was aimed at finding a method for detecting submarines. The problem was that the attenuation of light in water is so high over the distances required that it was not possible to "see" submarines in the traditional sense. Due to the low attenuation of ultrasound in water over the distances of interest, Paul Langevin of France, was the first to successfully demonstrate SONAR [41]. Here he used a quartz piezoelectric transducers machined as steel/quartz composite designed to work at frequencies above the audible range.

Following from Dr. Langevin's success, the U.S. government began work on its own submarine detection research. Most piezoelectric work up until this time was concerned with static effects. Ultrasound however required a study of the dynamic behavior of piezoelectric devices. It was during this time the Walter Cady developed the first crystal oscillator [42]. He noticed that by connecting a crystal to a wideband amplification circuit, there was a large response at the output of the amplifier near the mechanical resonance of the piezoelectric crystal. He quickly patented the idea [43], as well as published the developments shortly after [44] [45]. There are two important classes of devices which resulted from this work on crystal resonators: frequency references and crystal filters. A common problem with telecommunication of that time was channel drift, where the frequency reference would shift slightly and interfere with a neighboring channel. Additionally there was a very limited channel bandwidth and spacing used for voice information, which required sharp filters. Circuits made with purely electrical components had a much higher loss factor, than what was possible with ultrasonic filters. This discovery was so important, it is estimated that during World War II, some 30 Million of quartz resonators were produced for the war [41]. Additionally quartz resonators replaced pendulums in the bureau of standards for

frequency reference until the advent of the atomic clock. Even today crystal resonators are used in nearly every modern computer system.

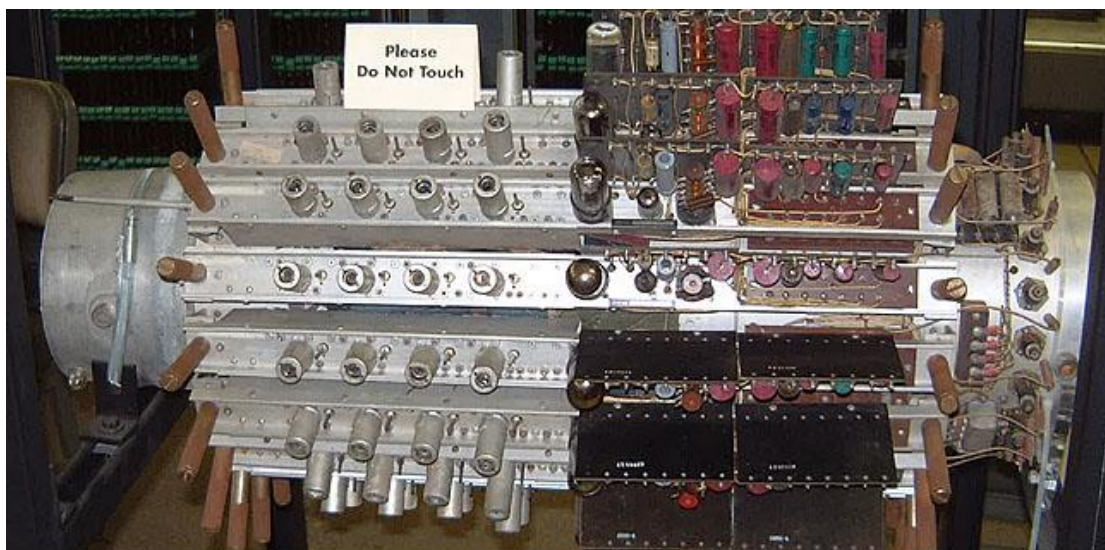


Figure 1.4: Ultrasonic digital delay line memory, utilized in the UNIVAC-I computer system [9]

One of the major technical pushes going into World War II was the use of RADAR for detection of objects. Here another application of ultrasound was found in a delay line. Perhaps the most cited reference into its use for RADAR systems is Emslie and McConnel's book "Radar Systems Engineering" [46]. For Moving Target Indication RADAR, it became challenging to differentiate between a moving target and fixed targets as each would appear on the screen with the same intensity. By having a delay line with time delay equal to the pulse repetition rate it is possible to subtract out the stationary targets, thereby only displaying the moving targets on the screen. Using passive electric components, such as inductors and capacitors, only allows a very small delay, and bandwidth. If a transmission line cable were implemented, due to the speed of electric signals it would need to be very long, which

results in large loss and limited bandwidth. There are two benefits for using ultrasonic delay lines compared to purely electrical components, (1) the slower speed allows for a physically smaller waveguide, (2) the lower loss allows for better signal quality and bandwidth. The first successful demonstration of this principle was done by Shockley, (co-inventor of the transistor) at Bell Labs in the 1930s. J. Presper Eckert, one of the inventors of ENIAC, inspired by Shockley's work, improved upon the design by using mercury instead of water as the delay medium [47]. After working on RADAR he changed course to working full time on computer processing and found a new application for the delay line as a form of digital memory storage. The sequential access memory, an ultrasonic delay line memory, was the memory used for ENIAC and was used in computing systems until it was replaced by transistor based random access memory, and magnetic bubble memory.

At this point in time many of the major applications of piezoelectric devices had been discovered and the major advancements from this point are related to improvement in performance; fabrication techniques, quality factor, center frequency, and physical size of devices. While it may be pessimistic to say that from these early developments to present day have been more about optimization than innovative new solutions, it is these optimizations which have rendered the on-chip SONAR a possibility for discussion.

It has long been the dream of alchemists and wizards to grow their own crystals. While much work was done in crystal growth in the early 20th century, it was in the realm of academic curiosity. Much of the quartz crystals used by the U.S. Military during World War II were obtained from mines in Brazil [48]. This generated a lot of interest in perfecting a growth method to ensure U.S. strategic independence. An added benefit being that synthetic growth techniques could produce much higher quality crystals than those found naturally. Perhaps the most desirable of these

resonators is the longitudinal mode resonator due to the existence of a single resonant frequency. Often, practical concerns in fabrication lead to the use of other modes to obtain the higher frequencies [49]. In 1942, Warren P. Mason reported that for longitudinal devices the frequency range of operation was 50 to 500 KHz, using bulk quartz [50]. By 1982, then modern processes were able to thin quartz to about 25 μm , which had a resonance at roughly 60 MHz. In order to push up to 100 MHz and into the GHz operating regions requires films less than 5 μm , and depending on the material, less than 1 μm [49].

Taking a bulk material and thinning it does not allow for a practical fabrication method, especially for CMOS integration. Thin film processing, a technology developed along with transistors, would allow for the creation of thin films. One of the earliest efforts involved thin film cadmium sulfide (CdS) on top of a quartz substrate [51]. This composite structure allowed for the half mode resonance of the CdS film to match the nine-halves mode resonance of the quartz, to leverage the higher frequency of the CdS with the temperature stability and high quality factor of the quartz substrate. This was followed shortly by the same transducer on top of a silicon substrate [52]. The importance of this development on silicon is that it shows a device which could be integrated with active electronics, a goal started so long ago and still discussed today.

The problem however with both of these devices is that they are highly over-moded, that is, the substrate is thick enough such that many resonant modes exist at near the frequency of interest, whereas, established earlier, a single resonant mode is desired. This can be accomplished by thinning the supporting system (silicon and quartz) only in the area of interest to form a membrane. While many developments took place to improve the processing, one work in specific is of note and that is the work by Ruby from 1994, where he developed a Thin Film longitudinal mode resonator in aluminum nitride [53]. In this process they developed devices with quality

factors of over 1000 and resonant frequencies between 1.5 GHz and 7.5 GHz. The reason this reference was chosen is that the work later led to the implementation of a duplexer using aluminum nitride bulk acoustic transducers [54]. This particular publication further led to the commercialization of a device which is still in use in today's modern handsets. This has further helped to transition aluminum nitride from a laboratory curiosity to a manufacturing process with an infrastructure to support it. Finally a note-worthy publication is from Olsson [32] which presented an arrangement of different RF filters and accelerometers in a process, developed at Sandia, which is compatible with the CMOS stack.

1.7 Chip obfuscation

Due to the prohibitive expense of building a modern semiconductor fabrication facility (estimates are at \$5-\$10 billion USD [55] [56]), many companies now rely on a few large foundries often located overseas. Chip company powerhouses such as LSI logic, Texas Instruments, and even AMD (who spun off their fab to Global Foundries), now depend on external foundries for advanced technology nodes [57]. Some of these locations are considered untrusted, and as designs are sent overseas the designs may be copied, with untrusted foundries selling the designs as their own, or tamper with the layout, adding what is known as a hardware trojan [55].

There are many ways in which IP can be stolen along the entire production chain for semiconductor devices. Modern CMOS design has many stages required to manage ~1 Billion transistors per chip [56]. As such there are many ways to alleviate the designs of such complex systems. Entire companies have formed as a support system, providing companies with building blocks, such as basic gates, to more complex digital logic such as registers and clocking elements. End users can use the components, which have already been fabricated and tested, in their designs, along

with automated routing programs to build these large complex systems. Even if a user was building an entire custom circuit without additional IP, when they send it to a foundry, it has access to the entirety of the design. It could sell these designs as their own IP, or simply fabricate additional chips and sell them [58]. It is estimated that the semiconductor industry loses as much as \$4 billion USD annually, via stolen IP [55]. This is additionally troubling in defense applications where enemies could gain access to advanced U.S. technology, reducing reliability of U.S. defense systems.

Another troubling aspect of the system is the possibility of hardware trojans. When a foundry gains access to the designs, it could add additional circuitry for intentional failure. While there have been many theorized types of trojan attacks { [56] [59] [60] }, the two functions which are most alarming are the kill switch and the back door [59]. The kill switch is a function where either after a certain period of time the circuit disables the entire chip, or after a certain command or bit stream is detected then the chip stop operating. One could envision a mission critical application where a missile fails to detonate or a pilot loses control of the plane due a kill switch. The back door attack would allow an enemy to either access classified data or communications, or give some degree of control of the circuits function, while the chip is operating.

Much work in trusted electronics has been from a purely theoretical stand point, however there a few incidents reported in the news which cause great alarm. In 2007 an Israeli air strike on Syria was not detected by the supposedly state of the art Syrian radar. While nothing was made public it is highly suspected that a back door access was used to shut down the Syrian radar [56]. Another incident in 2014 involved an American contractor in a criminal scheme to sell refurbished untrusted components to the U.S. government for use on a nuclear submarine [60]. Aside from these handfuls of incidents, with no confirmed hardware Trojans, there has been no news made public on the discovery of hardware trojans. Even so the U.S. government is clearly taking

this threat seriously with programs such as the DARPA TRUST program [61] and the IARPA TIC program [62].

One solution that has been put forth by the IARPA TIC program is the use of split fab manufacturing. In this scenario state of the art transistors and the first few metal layers, front end of the line, are fabricated in an untrusted foundry, and the back end of line metal layers are fabricated in a trusted foundry. Since the metal wires on the higher levels have less strict design rules, an older foundry should be able to finish fabrication. This way, the only information the untrusted foundry gets is a sea of transistors, with little understanding on how they are connected, making both copying and tampering much more difficult.

Ultrasonic communication links allows for an additional layer of obfuscation. The links themselves are effectively an abstract layer of communication. If they are utilized as a reconfigurable phased array, then the direction of the links is unknown from a physical level. Even if the entire chip is fabricated in an untrusted foundry, the piezoelectric layer could be fabricated at a trusted site helping to obscure the functionality of the chip. Additionally the new guidelines for the ITRS [63] suggest that future systems will make progress through the use of heterogeneous integration of different technologies.

1.8 *Dissertation Scope*

The remainder of the thesis is outlined as follows. Chapter 2 covers the basics of ultrasonic waves propagation, with a focus on implementing GHz waves inside the silicon substrate. Chapter 3 demonstrates ultrasonic transducer design with an emphasis on the use of piezoelectric transducers for the generation and detection of ultrasound in silicon, using microfabrication techniques. Chapter 4 demonstrates the effect of diffraction on wave propagation from ultrasonic transducers, and the design

of a phased array system for controllably steering ultrasonic beams. Chapter 5 describes and quantifies an ultrasonic link which was physically implemented. This system used aluminum nitride transducers to send a bit stream at a rate of 120 Megabits per second. The link budget was estimated using energy loss due to diffraction, conversion and inherent material losses. Chapter 6 describes the efforts to integrate the piezoelectric transducers directly with CMOS circuitry on a single die. Demonstrating the capability to measure ultrasonic response with on-chip amplifiers. Chapter 7 describes a sensor platform using integrated piezoelectric transducers for measuring material properties, and the use of the system in imaging a fingerprint phantom.

Chapter 2

ULTRASONIC TECHNICAL BACKGROUND

2.1 Introduction to Ultrasound and Nomenclature

The micro-sonar, the focus of this thesis is a system composed of multiple ultrasonic transducers. As such, it is important to explore the properties of the individual transducers. This chapter will explore the generation, propagation and detection of ultrasonic waves into a silicon substrate. The transducers studied here are thin film piezoelectric transducers made using thin film microfabrication techniques. A one dimensional wave model will be used, following Mason's model [64]. From the 1-D model, transducer design methodology will be developed for aluminum nitride transducers on silicon. The precision of microfabrication techniques on a silicon substrate allows for additional freedom in designing the transducer frequency response. Since the micro-sonar operates in three dimensional space, 2-D and 3-D models will be derived for wave propagation from the transducer. This leads to the design of phased arrays for reconfigurable communication channels, in future chapters.

2.2 Acoustic waves in silicon

As illustrated in Figure 2.1, there are two types of acoustic waves which can propagate in elastic solids. If we consider an infinitesimal volume of the elastic solid as a "particle," then the motion of the particle with respect to the direction the wave travels is what distinguishes the two wave types. For longitudinal or compressional waves, particles move in the direction of the traveling wave, as seen in Figure 1b, moving in the positive and negative z direction. Shear or transverse waves, occur

when the particle moves perpendicular to the direction of travel as seen in Figure 2.1c, the wave is travelling in the z-direction while the particles move in the x or y direction.

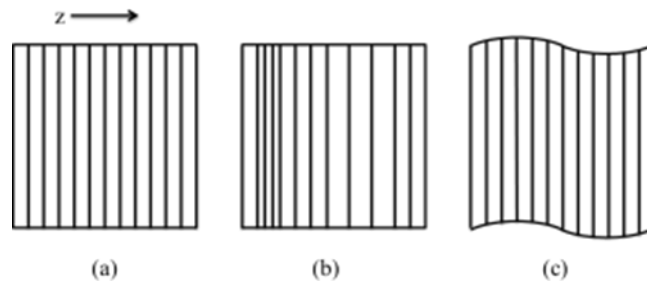


Figure 2.1: Illustration of the two different wave types for elastic solids. (a) Unperturbed one-dimensional elastic material (b) Longitudinal wave (c) shear wave

While it was the work of Lord Rayleigh which first quantified sound waves in his seminal piece [65], it was research in earthquakes, where some of the nomenclature on waves originates. Much of the early earthquake research involved studying surface waves propagating in an elastic half space [65]-[67], the waves actually felt during an earthquake. While SAW devices utilize surface waves, the focus of this thesis is on waves propagating in the bulk of the material. It was Richard Dixon Oldham who postulated that the earth featured a stiff core and a softer mantle [68]. When an earthquake starts it launches two bulk waves in addition to the surface wave. These travel through the earth, reflect off the core and return to the surface. The first wave detected was known as the primary wave or P-wave, and is a longitudinal wave. Longitudinal waves travel faster than shear waves. The second wave to arrive is known as the secondary wave or S-wave, and is a shear wave. A further classification of S-waves are the SH and the SV waves which stand for Shear-Horizontal and Shear-

Vertical, classifying them based on the polarization. For the purposes of this thesis, P-waves and longitudinal waves will be used as synonyms for the remainder of the text.

The waves of interest are the P-waves, as the transducer design developed here are for transducers whose primary mode of operation is the generation of longitudinal waves. Acoustic waves in solids are often modeled only with the wave of interest, however in truth both wave types exist and often are coupled together. The derivations in this section are simplified to one-dimensional, isotropic homogenous solid materials. As stated before this is done for the simplicity of visualization and the fact that the complexity of higher dimensions and anisotropic materials do not have closed form solutions and require simulation. As this is a wave phenomenon, a lot of the development here is directly analogous to electromagnetic waves. The difference in stress, force per area, is directly analogous to the electrical potential difference (voltage). Likewise the particle velocity (velocity of a particle not wave velocity) is directly analogous to the electrical current.

2.3 Wave equation for elastic solids

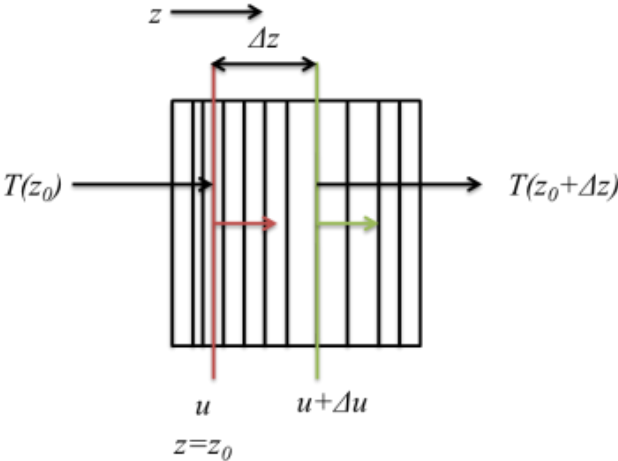


Figure 2.2: Illustration of a compressional wave traveling through an elastic material

Consider two planes or “particles” running perpendicular to a travelling transverse wave as shown in Figure 2. The at rest location of each particle is $z = z_0$ and $z_0 + \Delta z$. As the wave passes through these planes, each particle moves a small distance u and $u + \Delta u$ respectively. The variable u is known as the particle displacement. If Δu is equal to zero, then no wave is travelling and instead the entire solid has undergone a gross displacement. Strain is defined as the fractional change in size of a physical body then we can calculate the strain as (2.1)

$$S = \lim_{\Delta z \rightarrow 0} \frac{(u + \Delta u) - u}{\Delta z} = \frac{du}{dz} \quad (2.1)$$

Where the symbol S will be used from here on to represent the strain. As the wave moves through the material, stretching and compressing regions, there must also be an associated force. In an elastic material the strain can be related to the stress through Hooke’s law:

$$T = c_{11} \cdot S \quad (2.2)$$

Where T is stress, with units of Newtons per meter squared, and c_{11} is the elastic coefficient. In general materials may not be isotropic and as such have different elastic properties for different directions, here c_{11} is a single constant used for the 1-dimensional case along a single axis of the material. Using this expression one can determine the stress at each of the planes z_0 and $z_0 + \Delta z$.

$$T(z_0) = c_{11} \frac{du}{dz} \Big|_{z_0} \quad (2.3)$$

$$T(z_0 + \Delta z) = c_{11} \left. \frac{du}{dz} \right|_{z_0 + \Delta z} \quad (2.4)$$

The net force upon the region bounded by the two planes is :

$$F_{spatial} = A \cdot (T(z_0 + \Delta z) - T(z_0)) \quad (2.5)$$

The difference in stress is multiplied by the cross sectional area of the planes, A . This is a spatially dependent force with independent variable z_0 . While this accounts for spatial variations in force, it must also obey Newton's second law of motion:

$$F_{temporal} = m \cdot a = \rho_{m0} \cdot A \cdot \Delta z \cdot \frac{d^2u}{dt^2} \quad (2.6)$$

The mass is represented by the product of the uncompressed density, ρ_{m0} , and the volume, $A \cdot \Delta z$. The acceleration is the second time derivative of particle displacement. The spatial and temporal forces must equate:

$$F_{spatial} = F_{temporal} \quad (2.7)$$

$$E \cdot \frac{\left(\left. \frac{du}{dz} \right|_{z_0 + \Delta z} - \left. \frac{du}{dz} \right|_{z_0} \right)}{\Delta z} = \rho_{m0} \cdot \frac{d^2u}{dt^2} \quad (2.8)$$

Again the limit as Δz goes to zero yields the final form of the one dimensional wave equation.

$$\frac{d^2u}{dz^2} = \frac{1}{V_a^2} \frac{d^2u}{dt^2} \quad (2.9)$$

Where V_a is the speed of sound in the material with units of m/s, and is obtained by:

$$V_a = \sqrt{\frac{c_{11}}{\rho_{m0}}} \quad (2.10)$$

As seen in this expression, the speed of sound depends on the material properties of the solid. Another important wave property for future derivations is the wave number or propagation constant:

$$\beta_a = \frac{\omega}{V_a} \quad (2.11)$$

These expressions are of course valid for 1-dimensional motion of transverse waves; a more complete treatment would result with a similar expression using tensor notation, rather than a single variable. The derivation for shear waves has a near identical form, the difference being the stiffness constant used [69].

2.4 *Acoustic Impedance*

As stress is analogous to voltage and particle velocity (the time derivative of particle displacement) is analogous to current, the ratio of the two is an acoustic analog of electrical impedance.

$$Z = -\frac{T}{v} \quad (2.12)$$

And just like electromagnetic plane waves, for acoustic plane waves different materials have different characteristic impedances, derived from a forward traveling wave:

$$Z_0 = -\frac{T_f}{v_F} = \sqrt{\rho_{m0}c_{11}} \quad (2.13)$$

The characteristic acoustic impedance quantity has units of pressure per velocity or a Rayl which is a $\text{kg/m}^2\text{s}$ in SI units. The acoustic impedance of some common materials useful for ultrasound in silicon are summarized in the table here.

Table 2.1: Summary acoustic properties of common CMOS materials

Material	ρ_{m0} (kg/m^3)	c_{11} (GPa)	V_a (m/s)	Z_0 (MRayl)
Water	1000	2.23	1480	1.494
Vacuum	0	0	0	0
Air	1240	1.4E-7	344	4.27E-4
Silicon	2331	166	8439	19.7
Silicon Dioxide	2200	69	5600	12.3
Silicon Nitride	3170	270	9229	29.3
Aluminum Nitride	3230	396	11073	35.8
Aluminum	2700	111	6420	17.3
Molybdenum	10000	398	6300	63.1

Notice how the impedances of the materials are within the same order of magnitude. This is beneficial to transducer design, as will be seen in the subsequent section.

2.5 Material Boundary Conditions

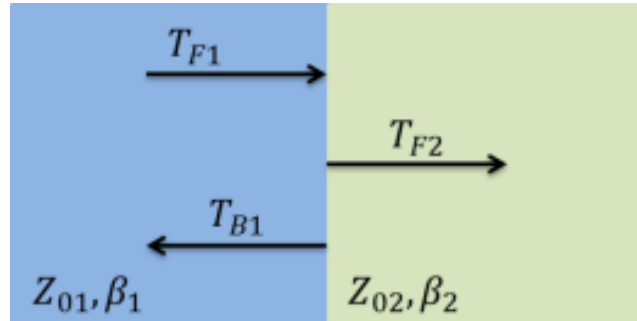


Figure 2.3: Illustration of an acoustic boundary between two materials. The arrows with T represent a stress wave travelling the regions. Z_{01} and Z_{02} are the acoustic impedance in each region. β_1 and β_2 are the wavenumbers in each region.

An important aspect of transducer design is the condition when an acoustic wave travels between two different materials. This is directly analogous to electromagnetic plane waves. In the 1-dimensional case this is also compatible with transmission line theory. Consider the case shown in Figure 2.2, where a wave traveling in Region 1 impinges upon the boundary between the regions. Some of the wave continues into Region 2, but a portion is reflected back to Region 1. Considering the sinusoidal solution to the wave equation, then the complete expression for the total waves in each region can be expressed as

$$T_1 = T_{F1}e^{-j\beta_1z} + T_{B1}e^{j\beta_1z} \quad (2.14)$$

$$v_1 = -\frac{T_{F1}}{Z_{01}}e^{-j\beta_1z} + \frac{T_{B1}}{Z_{01}}e^{j\beta_1z} \quad (2.15)$$

$$T_2 = T_{F2}e^{-j\beta_2z} \quad (2.16)$$

$$v_2 = -\frac{T_{F2}}{Z_{02}}e^{-j\beta_2z} \quad (2.17)$$

The amount of energy reflected and transmitted depends upon the material properties of the two regions. The reflection coefficient is the ratio of the reflected wave to the incident wave

$$\Gamma = \frac{T_{B2}}{T_{F1}} \quad (2.18)$$

and the transmission coefficient is the ratio of the transmitted wave to the incident wave

$$\zeta_T = \frac{T_{F2}}{T_{F1}} \quad (2.19)$$

At the boundary between the two regions, the stress and particle velocity must be continuous. Using this boundary condition and the definitions of Γ (2.18) and ζ_T (2.19), along with (2.14) through (2.17) yields

$$\Gamma = \frac{Z_{02} - Z_{01}}{Z_{02} + Z_{01}} \quad (2.20)$$

$$\zeta_T = \frac{2 \cdot Z_{02}}{Z_{02} + Z_{01}} \quad (2.21)$$

2.6 Acoustic Losses

The expression for power in an elastic wave can be determined as follows

$$P_a = -\frac{1}{2} \cdot (v^* \cdot T) \cdot A \quad (2.22)$$

Where T is the stress on the particle, v is the particle velocity, and A is the cross sectional area. Poynting's theorem, in its simplest form states that the power of the wave is conserved. This can be accomplished by examining the spatial change in power:

$$\frac{d}{dz}(P_a) = -\frac{1}{2}(j\omega\rho_{m0}vv^* - j\omega cSS^*)A \quad (2.23)$$

This expression shows that the change in P_a is purely imaginary and therefore power is conserved because the change in the real part of power is zero.

$$\frac{d}{dz}Re(P_a) = 0 \quad (2.24)$$

This is to be expected since the power was found in a lossless system. There are several mechanisms which can incur loss in an acoustic signal. Thermal elastic losses, occur since as a material expands it decreases in temperature, and when it contracts it increases in temperature in the adiabatic limit. If the material has good thermal conduction then the transfer of energy from areas of the wave undergoing compression to the regions of rarefaction will remove energy from the wave, this is known as thermos-elastic dissipation. Silicon however has very low thermo-elastic dissipation; it is on the order of 0.036 dB/cm at 480 MHz [70], insignificant for on-chip pulse propagation length scales. Another source of loss is due to scattering of waves at grain boundaries or due to dislocations in the material. As silicon is a single crystal material, with modern silicon wafer fabrication, this value is also negligible, as shown in [70] at reasonable temperatures and high frequency, attenuation is independent of number of dislocations in the material. The greatest source of acoustic loss in silicon comes from viscoelastic or “internal friction” losses.

Since there are no purely elastic materials, a loss factor comes from viscous damping of neighboring particles. In addition to the Hooke’s law relation between stress T and strain S , there is an additional stress coming from neighboring viscous damping and characterized by a parameter η :

$$T_\eta = \eta \frac{dS}{dt} \quad (2.25)$$

Similar to conduction loss in electromagnetic fields, acoustic losses can be modeled as a complex elastic constant c

$$c = c_0 + j\omega\eta \quad (2.26)$$

Referring back to Poynting's Theorem in (2.23), we see that a complex stiffness coefficient means there is now a real component.

$$\frac{d}{dz}(\text{Re}(P_a)) = -\frac{1}{2}\omega^2\eta SS^*A \quad (2.27)$$

If we make the approximation that the loss is small, then this expression simplifies to:

$$\frac{1}{P_a} \frac{dP_a}{dz} = -\frac{\eta\omega^2}{V_a^3 \rho_{m0}} \quad (2.28)$$

This differential equation has the solution:

$$P_a = P_0 e^{-2\alpha z} \quad (2.29)$$

$$\alpha = \frac{\eta\omega^2}{V_a^3 \rho_{m0}} \quad (2.30)$$

For silicon this attenuation value has been characterized in the past [69], to a value of approximately 10^{-17} dB/Hz²/cm, which is a viscosity η of $0.035 \frac{kg}{s \cdot m}$. A more meaningful representation of this has been plotted below. Here we see the attenuation value normalized to wavelength, as well as the total loss in the channel for a distance of 1300 mm, both as a function of frequency.

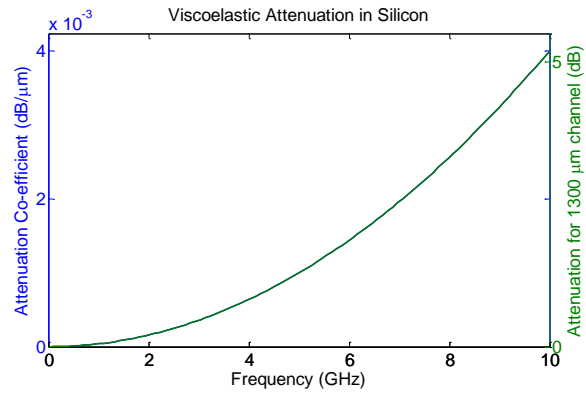


Figure 2.4: Acoustic Loss in silicon as a function of frequency.

Chapter 3

ULTRASONIC PIEZOELECTRIC TRANSDUCERS

This chapter will present a design of a one-dimensional piezoelectric transducer. While the physical ultrasonic communication channel is affected by 2-D and 3-D effects, it is easier to understand the coupling for the one-dimensional electrical to mechanical conversion using one dimension. The 2D/3D higher dimensional effects will be explored in the next chapter in the context of diffraction.

In order for the channel to operate at low powers and low energy per bit, there must be an efficient conversion from the electrical domain to the acoustic domain at the transducer, and then mechanical to electrical domain at the receiver. Piezoelectric transducers are desired for their high values of conversion efficiency, owing to relatively high piezoelectric coefficients. The first section defines a piezoelectric material and the unique properties they exhibit. Physically a piezoelectric ultrasound transducer is a capacitor with the piezoelectric material acting as the dielectric layer. The electrical impedance, which includes the mechanical coupling to the transducer, is important as it allows for the determination of optimal matching of source and load impedance of supporting electronics. In addition to the transducers utilized in a communication channel, additional resonant devices, used for other applications, will be examined to demonstrate the general purpose use of the transducer model.

In addition to the electrical impedance of the transducer, another goal is to determine the power and frequency transfer characteristics, considering only the real part of the electrical impedance. A common practice is to develop a circuit model which treats the acoustic layers as electrical transmission lines, and an electrical transformer as the conversion mechanism between the two domains. These models

will be derived and used to determine the conversion loss of the one-dimensional communications channel.

3.1 *Piezoelectric Materials*

In most materials, there is no coupling between the mechanical domain and the electric domains. The mechanical domain referred to here is the motion described by Hooke's Law (2.2). In the electrical domain, for non-ferroelectric dielectric materials the relationship between electric displacement, D , and the electric field, E , is the dielectric constant, .

$$D = \epsilon E \quad (3.1)$$

Piezoelectric materials are unique in that an applied stress can change the electric displacement, so called the direct piezoelectric effect, and an applied electrical displacement induces a strain, which is called the inverse-piezoelectric effect. What are generally two separate linear relations ($D = \epsilon E, T = cS$), are coupled to form two coupled equations. As such there are many ways to represent the piezoelectric effect through the use of several different piezoelectric coefficients; d , e , g , and h . The constituent piezoelectric formulae are summarized here as a change to Hooke's Law (2.2) and the electric displacement relationship (3.1)

$$T = c^E S - eE, \quad D = eS + \epsilon^S E \quad (3.2)$$

$$S = \frac{1}{c^E} T + dE, \quad D = dT + \epsilon^T E \quad (3.3)$$

$$S = \frac{1}{c^D}T + gD, \quad E = -gT + \frac{1}{\epsilon^T}D \quad (3.4)$$

$$T = c^D S - hD, \quad E = -hS + \frac{1}{\epsilon^S}D \quad (3.5)$$

The superscript notation denotes which quantity is held constant while measuring the material constant. For instance c^E is the elastic constant, measured when the electric field is zero. The significance is that since the electric and mechanical domains are coupled the elastic coefficient become stiffer and the dielectric constant can appear larger. A summary of the dimensions of the piezoelectric coefficients is in Table 3.1.

Table 3.1: Dimensional units of the piezoelectric coefficients

Coefficient	SI Units
d	C/N or m/V
e	C/m ²
g	V m/N
h	V/m or N/C

Consider a condition, in which the piezoelectric medium is infinite, or a two electrode transducer which has both electrode plates shorted, since no voltage can exist across shorted electrodes, the electrical displacement D must be zero. Effectively the piezoelectric effect has been nullified since charge cannot accumulate on the electrodes. The expressions in (3.2) can be simplified to a single expression.

$$T = c^E \left(1 + \frac{e^2}{c\epsilon} \right) S = c^D S \quad (3.6)$$

Where \underline{c}^D is known as the piezoelectrically stiffened elastic coefficient. Even though the piezoelectric material cannot produce charge the piezoelectric effects causes an effective “stiffening” whereby the stiffness constant becomes larger. This also has the effect of increasing the speed of sound in the piezoelectric transducer due to (2.10). With this relationship there is a new parameter known as the piezoelectric coupling constant K^2 :

$$K^2 = \frac{e^2}{c\epsilon} \quad (3.7)$$

There are some situations where the piezoelectric expressions may simplify. For instance when operated at DC and each face of the piezoelectric material is free, then the stress is zero. This simplifies the expression in (3.3) to (3.1) and a linear relationship between strain and electric field, related by the d coefficient.

$$S = dE \quad (3.8)$$

Unfortunately for ultrasonic transducers, in most real cases, this simplification is inadequate for describing the correct behavior. When operated at a nonzero frequency, there are spatial and temporal variations of stress throughout the piezoelectric material, necessitating the use of the full expression in (3.3) for modeling behavior. A summary of material properties from several piezoelectric materials is summarized below.

Table 3.2: Summary of common piezoelectric material properties

Material	$V_l(\text{m/s})$	$Z_c(\text{MRayls})$	ϵ_r	$\rho_m(10^3\text{kg/m}^3)$	K^2
AlN [76]	10.4	34.0	9.9	3.23	0.09
LiNbO ₃ [69]	7.36	34.2	39.0	4.64	0.32
PZT [69]	4.33	31.6	847	7.3	0.35

3.2 Piezoelectric Transducers

We now want to consider using the piezoelectric material in one dimension as a transducer for generating and detecting ultrasound. For the sake of simplicity we will consider a one dimensional model for the transducer. Where the transducer is very large in the x-y dimensions, i.e. a large area A with respect to wavelength, doing so allows us to isolate focus on longitudinal waves in the z-direction.

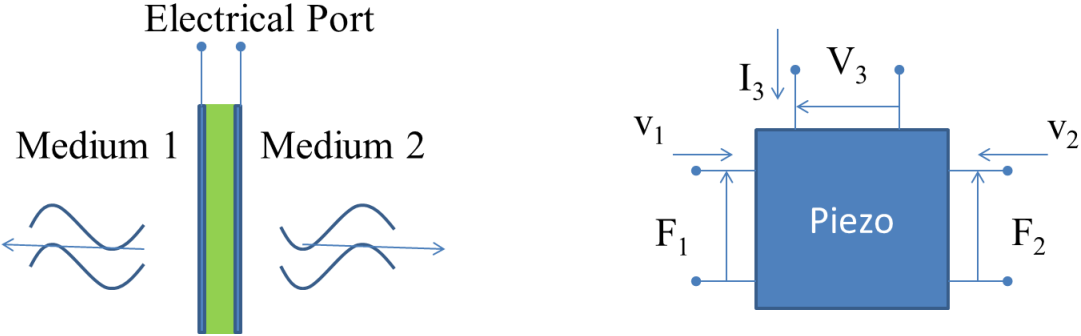


Figure 3.1: Illustration of piezoelectric transducer model, the system is modeled as a three port device, two acoustic ports representing each face of the transducer and one electric port

Consider a 3-port model for the transducer, containing one electrical port and two mechanical ports, with each mechanical port representing a surface of the transducer. A representation of this model can be seen in Figure 3.1. Each mechanical port has a force F and a velocity v which are analogous to the electrical port with parameters of voltage V and current I . The parameters at each mechanical port can be determined from the force and particle velocity at the physical location of the ports (taking the center of the device to be $z = 0$).

$$F_1 = -A \cdot T \left(-\frac{l}{2} \right) \quad (3.9)$$

$$v_1 = v \left(-\frac{l}{2} \right) \quad (3.10)$$

$$F_2 = -A \cdot T \left(\frac{l}{2} \right) \quad (3.11)$$

$$v_2 = -v \left(\frac{l}{2} \right) \quad (3.12)$$

By convention the force F is defined as the external force applied, and the stress T is defined as the internal stress, thus a negative in Equation (3.9) and (3.10). Particle velocity is defined as positive inward to the device, thus one is positive and the other negative. The piezoelectric expressions are in terms of stress, strain, electric field, and electric displacement, but the ports are in terms of force, particle velocity, voltage, and current, therefore they need to be related in order to develop a complete expression for

the three port system. The simplest relation is between the stress and force as they are related by area as seen in (3.9) and (3.11). The strain and particle velocity are both partial derivatives of the particle displacement and as such are related as

$$S = \frac{1}{j\omega} \frac{dv}{dz}. \quad (3.13)$$

The strain depends on the spatial variation of the particle velocity necessitating a solution to the wave equation from Equation (2.9). Consider the sinusoidal solution to the wave equation, given in (3.14).

$$v = v_F e^{-j\beta_a z} + v_B e^{j\beta_a z} \quad (3.14)$$

Instead of considering the wave equation in terms of forward traveling and backwards traveling waves, it is possible using (3.10) and (3.12) along with (3.14) to solve for the particle velocity in terms of the port values v_1 and v_2 .

$$v(z) = - \frac{v_1 \cdot \sin(\beta_a (z - \frac{l}{2})) + v_2 \cdot \sin(\beta_a (z + \frac{l}{2}))}{\sin(\beta_a l)} \quad (3.15)$$

Looking now at the electrical parameters, fundamentally the current and electric displacement is related as in (3.16).

$$I_3 = A \cdot J_3 = A \cdot \frac{dD}{dt} = j\omega A \cdot D \quad (3.16)$$

Since the piezoelectric transducer only has two electrodes, in order to satisfy Kirchoff's Current Law, then the current I_3 must be independent of z throughout the thickness of the transducer. This in turn implies that D must be independent of z . If D

is independent of position, by (3.16) and S does depend on z as in (3.15), then using the piezoelectric relations (3.2)-(3.5), one can conclude that E must be spatially dependent, therefore in order to determine the voltage across the electric ports, the field must be integrated across the whole transducer.

$$V_3 = \int_{-\frac{l}{2}}^{\frac{l}{2}} E \cdot dz \quad (3.17)$$

By using the form of the piezoelectric constituent equations shown in (3.5), along with the boundary conditions in (3.9) through (3.12), as well expressions relating the variables in (3.13), (3.16), and (3.17), and the wave solution in (3.15), can be solved for a series of equations relating all 6 port parameters.

$$\begin{bmatrix} F_1 \\ F_2 \\ V_3 \end{bmatrix} = \frac{1}{j} \begin{bmatrix} Z_{CA} \cot(\beta_a l) & Z_{CA} \csc(\beta_a l) & \frac{h}{\omega} \\ Z_{CA} \csc(\beta_a l) & Z_{CA} \cot(\beta_a l) & \frac{h}{\omega} \\ \frac{h}{\omega} & \frac{h}{\omega} & \frac{1}{\omega C_0} \end{bmatrix} \begin{bmatrix} v_1 \\ v_2 \\ I_3 \end{bmatrix} \quad (3.18)$$

Where the new variable Z_{CA} , is defined as:

$$Z_{CA} = Z_C \cdot A \quad (3.19)$$

Z_C is known as the characteristic impedance for the material, and is determined by (2.13) and Z_{CA} is known as the radiation impedance. From these relationships it is possible to determine an expression for the electrical input impedance of the transducer. If we consider the radiation impedance for both region 1 and region 2, these are the acoustic impedances seen looking out from the respective terminals, these are defined as:

$$Z_{1A} = -\frac{F_1}{v_1} = \frac{AT\left(-\frac{l}{2}\right)}{v\left(-\frac{l}{2}\right)} \quad (3.20)$$

$$Z_{2A} = -\frac{F_2}{v_2} = -\frac{AT\left(\frac{l}{2}\right)}{v\left(\frac{l}{2}\right)} \quad (3.21)$$

If the materials on each side of the transducer continue on to infinity, then the radiation impedances would be the characteristic impedances of the respective materials. If instead there is a stack of layers of different materials, each material can be treated as the acoustic equivalent of an electrical transmission line. Therefore using the relationships for Z_{1A} and Z_{2A} in (3.20) and (3.21) along with the relationship between the ports in (3.18) the electrical impedance can be found from the ratio of the voltage to the current to the expression in (3.22).

$$Z_3 = \frac{1}{j\omega C_0} \left[1 + k_t^2 \frac{j(Z_{1A} + Z_{2A})Z_{CA} \sin(\beta_a l) - 2Z_{CA}^2(1 - \cos(\beta_a l))}{[(Z_{CA}^2 + Z_{1A}Z_{2A}) \sin(\beta_a l) - jZ_{CA}(Z_{1A} + Z_{2A}) \cos(\beta_a l)]\beta_a l} \right] \quad (3.22)$$

Where C_0 is the clamped capacitance of the transducer and the parameter k_t^2 is related to the transverse piezoelectric coupling coefficient K by:

$$k_t^2 = \frac{K^2}{1 + K^2} \quad (3.23)$$

It is also known as the piezoelectric coupling coefficient. However if the value of K^2 and k_t^2 is small compared to 1 (as is the case for most piezoelectric materials), then they are approximately equal to each other. The expression derived in Equation (3.22) is quite complex and does not allow for any immediate revelations in device performance.

3.3 Thin Film Bulk Acoustic Resonators (FBAR)

As a starting point the simplest device is the thin film bulk acoustic resonator or an FBAR. The FBAR is a device which traps acoustic energy inside the thickness of the transducer. This is accomplished by having both faces of the transducer connected to a very low acoustic impedance, ideally 0. Referring back to Table 2.1, the acoustic impedance of air is 427 Rayls compared to aluminum nitride which has an acoustic impedance of 35.8 MRayls, a difference of five orders of magnitude. From a qualitative perspective, any ultrasonic energy generated in the transducer would be completely reflected at each face as seen in (2.20). The input impedance of an FBAR can be calculated from (3.22) by setting both Z_{1A} and Z_{2A} to 0,

$$Z_3 = \frac{1}{j\omega C_0} \left(1 - k_t^2 \frac{\tan\left(\frac{\beta_a l}{2}\right)}{\frac{\beta_a l}{2}} \right) \quad (3.24)$$

This impedance is plotted for a representative piezoelectric transducer is plotted in Figure 3.2. The simulation parameters are an aluminum nitride FBAR, 1.5 μm thick square with area 50 μm x 50 μm .

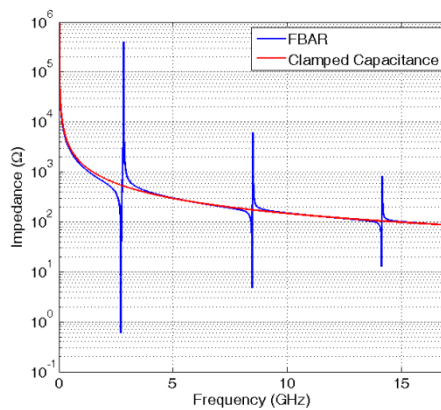


Figure 3.2 Electrical input impedance of an AIN FBAR

Notice that there are resonant and anti-resonant peaks in the impedance where the value goes to zero and infinity respectively. Without the piezoelectric effect, the transducer is simply a capacitor, the first term in Equation (3.22), plotted in red in Figure 3.2. The second term in Equation (3.24), referred to as the motional impedance, is caused by the piezoelectric properties. Because of the tangent in the expression, the frequencies at which the impedance becomes infinite can be calculated by (3.25).

$$\omega_{0n} = (2n + 1) \frac{\pi V_a}{l} \quad (3.25)$$

These are known as the antiresonant peaks and are multiple values due to the periodic nature of the tangent function. Physically this occurs at frequencies where the transducer thickness is an odd multiple of half-wavelengths long. The first peak is the largest, as evident from (3.24) containing a $1/\omega^2$ term for the motional impedance. Physically this is due to the fact that at higher frequencies allow, a whole wavelengths within the thickness of the transducer cancel out positive and negative charge additions due to the piezoelectric effect, reducing the overall net charge on the device electrodes. This model does not include a loss terms. These include material losses, losses of energy at the anchors, which further contributing to smaller resonant peaks.

The other frequency of interest is the resonant frequency, which is when the electrical impedance, is equal to zero. This occurs under the following condition:

$$\frac{\tan\left(\frac{\beta_a l}{2}\right)}{\frac{\beta_a l}{2}} = \frac{1}{k_t^2} \quad (3.26)$$

The purpose of an FBAR is to contain the acoustic energy within the transducer itself; however for the goal of an on-chip ultrasonic communication is to transmit ultrasonic energy into another medium. As a starting place though, one can expect that

the peak response of the transducer will be in the neighborhood of the resonant frequency.

3.4 *Highly Overtone Bulk Acoustic Resonator*

An HBAR is a modification on the FBAR in that one side of the FBAR is attached to a thick (multiple wavelengths) substrate which is backed by air or vacuum. Since the substrate is many wavelengths thick compared to the half wavelength thick FBAR there are multiple resonant peaks, with spacing equal to the fundamental resonance of the much larger substrate. This can be modelled from Equation (3.22) by considering Z_{1A} to be zero and Z_{2A} a complex impedance modeled by a transmission line terminated with a short circuit, with length and impedance values base on silicon material properties.

There are a few reasons that make the HBAR structure useful. Firstly they are easier to fabricate than an FBAR because there is no need to create a very thin film. HBAR is essentially an M-I-M structure common in CMOS (such as MOS gates). Secondly the substrate typically has a lower intrinsic material loss and since the wave spends most of the time traveling in the substrate the effective total loss can be lower. For aluminum nitride, the intrinsic material loss can be quantified as a quality factor of 500 [71]. The quality factor of silicon can be much higher, at least 2800 [72].

Again using aluminum nitride as the representative material a simulation of the same AlN resonator from the FBAR section, solidly mounted on a 50 μm thick silicon, results in the input impedance curve shown in Figure 3.3.

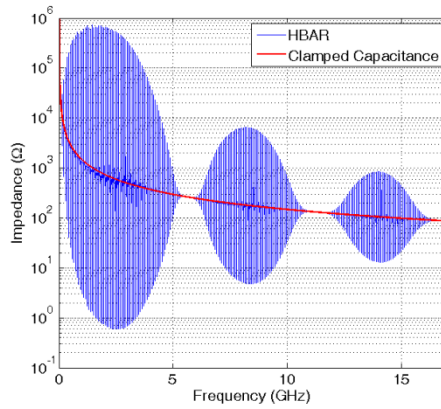


Figure 3.3 Electrical input impedance of an AlN HBAR on a silicon substrate

This gives a qualitative understanding of how well the transducer can couple energy into the silicon. Looking at the envelop of resonant peaks in Figure 3.3, the peaks are largest near the FBAR resonances and then diminish to nothing between resonance peaks. At these locations, little acoustic energy can couple from the transducer into the substrate.

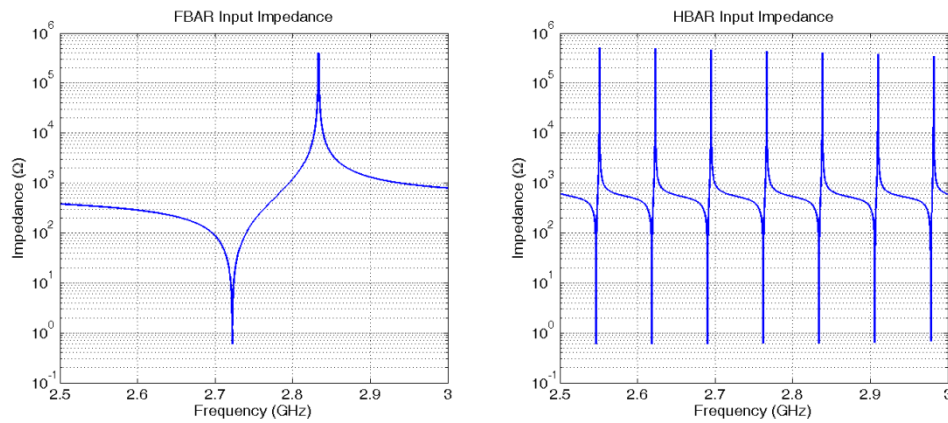


Figure 3.4: Expanded view of the FBAR and HBAR input impedances near the fundamental resonance peak of the transducer

The input impedance of both systems is calculated using the viscoelastic model for loss from Chapter 2 for both materials. From Figure 3.4, the resonance peaks of the

HBAR have higher quality factors due to the lower material loss in the silicon. The spacing of the peaks is approximately 75 MHz, corresponding to the thickness mode resonance of 50 μm thick silicon. In order for the one dimensional assumption of an HBAR to be true, most of the acoustic energy must remain directly underneath the transducer. This can hold for sufficiently large transducers, however for small transducers, diffraction loss can significantly reduce the quality factor. For microsonar applications, the ideal transducers are small, furthermore if they are operated in pulsed mode, such that the standing wave resonance of the HBAR does not have enough time to form, then these expressions do not give an adequate method of determining the input impedance of the transducer.

3.5 Transducer Power Transfer

The FBAR and HBAR devices give a starting point for understanding transducer operation in as much as they show qualitatively where the peak responses should be expected and why. For a more concrete quantitative understanding, the design space for piezoelectric ultrasound transducers is very large, containing multiple variables with few closed form solutions. In order to simplify some of the design from a qualitative perspective the focus here will be for the so-called, “air-backed” transducers. These are ones which generate waves into the medium defined by Z_{2A} , and the backing layer Z_{1A} is air, which is approximately zero. Furthermore these first steps consider the case where Z_{2A} is real. Physically this is a system which semi-infinite where Z_{2A} is the characteristic impedance of the transmitted region. In general Z_{2A} can be complex due to loss or finite thickness materials which are modelled as transmission lines. In such an event the KLM model and design methodology in the next section should be used.

A transducer will have responses at every half wave resonant as established with the FBAR. The range of interest for these transducers though is in the neighborhood of the primary resonance, $n = 0$ in Equation (3.25). The relationship between the resonance frequency and thickness of the transducer is well defined, such that it is possible to normalize the response with respect to resonance. By using the expressions in Equations (2.11) and (3.25), then the sinusoid terms in Equation (3.22) can be replaced as in Equation (3.27), making all calculated frequency values directly proportional to f_0 .

$$\beta_a l = \frac{\pi f}{f_0} \quad (3.27)$$

Finally to help ease the design space due to the number of variables consider a new normalized impedance parameter η_r , which is the ratio of the impedances Z_{2A} and Z_{CA} .

$$\eta_r = \frac{Z_{2A}}{Z_{CA}} \quad (3.28)$$

Consider a new form of the input impedance expressed in Equation (3.22), instead written as

$$Z_3 = \frac{1}{j\omega C_0} + jX_a + R_a. \quad (3.29)$$

From this expression it is evident that input impedance of the transducer is a capacitor in series with an additional complex term known as the motional impedance. Using this new form of the input impedance expression along with the substitutions in Equation (3.27) and Equation (3.28) and the air backed case, such that Z_{1A} is zero, the values of X_a and R_a can be derived as

$$X_a = \frac{f_0 k_t^2}{2\pi^2 f^2 C_0} \frac{\sin\left(\frac{\pi f}{f_0}\right) \left(2 + (Z_r^2 - 2) \cos\left(\frac{\pi f}{f_0}\right)\right)}{\sin^2\left(\frac{\pi f}{f_0}\right) + Z_r^2 \cos^2\left(\frac{\pi f}{f_0}\right)} \quad (3.30)$$

$$R_a = \frac{f_0 k_t^2}{2\pi^2 f^2 C_0} \frac{Z_r \left(1 - \cos\left(\frac{\pi f}{f_0}\right)\right)^2}{\sin^2\left(\frac{\pi f}{f_0}\right) + Z_r^2 \cos^2\left(\frac{\pi f}{f_0}\right)} \quad (3.31)$$

Both of these terms are scaled by k_t^2/C_0 . For most piezoelectric materials k_t^2 is very small, and as such the motional impedance is small compared to the clamped capacitance. As an illustrative example consider the same aluminum nitride HBAR transducer as before but on an infinite silicon half space. This models the impedance that is encountered when operating the transducer with a short pulse. The input impedance is plotted and compared to the clamped capacitance value in Figure 3.5.

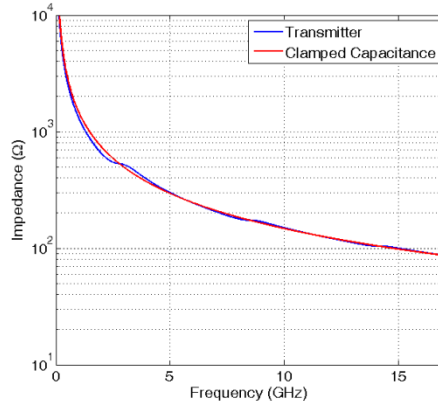


Figure 3.5: Input impedance for microsonar transducer

From an electrical perspective the input impedance of the transmitting transducer is numerically similar to the clamped capacitance impedance, save for a slight deviation near the resonances. This does little to illustrate the amount of energy converted to acoustic energy. To evaluate this consider the setup shown in Figure 3.6, where an electrical source is attached to a transducer.

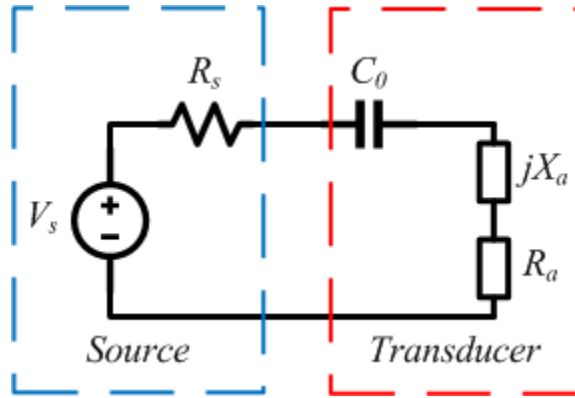


Figure 3.6: Driving Setup

The transducer itself physically is the same as a capacitor, therefore there is no electrical source of energy dissipation (aside from poor isolation of the dielectric), as such the real portion of the impedance represents the power that is converted from electrical to acoustic. While it is possible to have a complex source impedance, thereby designing an electrical matching network, in the context of on chip SONAR it is not practical to have inductors on the size scale of the transducers themselves. In this case the power factor, in Equation (3.32), illustrates the portion the applied power which is converted to acoustic power.

$$PF = \frac{R_a}{\sqrt{(R_a + R_s)^2 + (-1/\omega C_0 + X_a)^2}} \quad (3.32)$$

Ideally the source resistance R_s would be as small as possible so as to maximize the amount of power delivered to the acoustic load R_a . For now it shall be treated as zero. In practical circuits, this source resistance is typically 50 ohms of RF circuitry.

With the simplifications made thus far there are still three variables left; C_0 , k_t^2 and η_r . Since everything is normalized to the resonance frequency, which depends on thickness, C_0 effectively represents the area. As this is a one dimensional model, the

area does not affect performance. This can be illustrated in Equation (3.32) by setting R_s to zero and seeing that the C_0 term cancels. It is of course still important for the entire system design, and the diffraction loss will inform the value of C_0 , which will then dictate the circuit interface (including the choice of R_s). The value k_t^2 only allows for a small amount of designing as it is a fixed material property, its effect will be addressed later. This leaves the impedance ratio η_r as a design variable. While it is also somewhat restricted due to material properties, Section 3.6 will cover the design of matching layers.

Referring back to Equation (3.30), due to the complexity even limiting to a single variable the easiest starting point is approximation near resonance. At the resonance frequency X_a is equal to zero. If we consider that in general R_a and X_a are much smaller than $1/\omega C_0$ then Equation (3.32) can be approximated as

$$PF \approx \omega C_0 R_a . \quad (3.33)$$

From this expression, it is evident that the dependence of R_a on frequency is important in understanding the overall efficiency of generating ultrasound into the medium. Rewriting Equation (3.31) into the form of Equation (3.34) and Equation (3.35) yields:

$$R_a = \frac{f_0 k_t^2}{2\pi^2 f^2 C_0} H\left(\frac{\pi f}{f_0}\right) \quad (3.34)$$

where

$$H\left(\frac{\pi f}{f_0}\right) = \frac{Z_r \left(1 - \cos\left(\frac{\pi f}{f_0}\right)\right)^2}{\sin^2\left(\frac{\pi f}{f_0}\right) + Z_r^2 \cos^2\left(\frac{\pi f}{f_0}\right)} \quad (3.35)$$

The important parameters are the center frequency, peak amplitude and bandwidth of the power efficiency. The objective is to find the optimal point of operating a transducer with respect to maximizing the gain-bandwidth product. It is convenient to work with the expression for $H(\pi f / f_0)$, as it is symmetric about the center frequency and has closed form solutions for the parameters of interest. In general, the bandwidth estimated this way will provide a conservative estimate of the actual bandwidth of the transducer, and demonstrates the trends in the power factor. Plotting the $H(\pi f / f_0)$ in Equation (3.35) for several values of η_r yields the graphs in Figure 3.7.

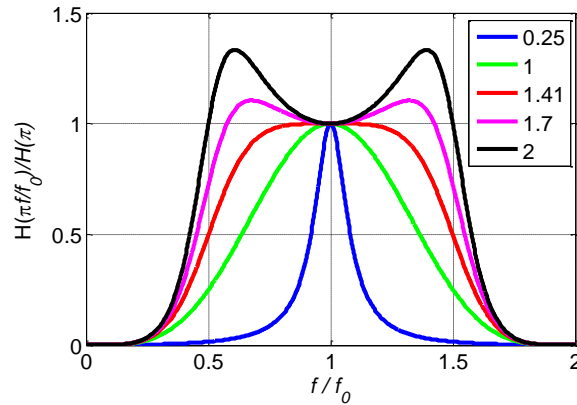


Figure 3.7 Value of $H(\pi f / f_0)$ normalized to the value at the resonance frequency f_0 , the legend shows which curve corresponds to different η_r

The plots are normalized to the value at f_0 to illustrate the shape as a function of η_r . For low values of η_r (and therefore Z_{2A}) the response peaks at the center frequency with a narrow bandwidth. The maximum bandwidth does not occur when

the two impedances are equal, but actually when η_r is $\sqrt{2}$. Above this value the peak shifts from the center frequency which is half wavelength resonance to the 1/4 and 3/4 resonant modes at 1/2 and 3/2 the resonance frequency. This is due to a change in the boundary condition, when $Z_{2A} < Z_{CA}$ then displacement is maximum at each face of the transducer, allowing for the half wavelength mode. In the air backed case if Z_{2A} is very large; on one side (air) the displacement is maximum and the other (Z_{2A}) the displacement is minimum, which allows for 1/4 resonance mode. This is further illustrated by considering the location of the lowest peaks found from Equation (3.35) and expressed in Equation (3.36) and plotted in Figure 3.8.

$$f_{max} = \begin{cases} f_0 & \eta_r < \sqrt{2} \\ \frac{f_0}{\pi} \cos^{-1}\left(\frac{1}{1 - Z_r^2}\right) & \eta_r \geq \sqrt{2} \end{cases} \quad (3.36)$$

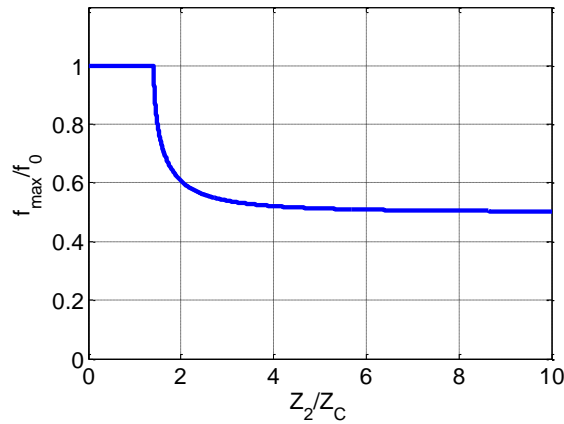


Figure 3.8: Center frequency of the impedance response with respect to impedance ratio

The location of the response maximum peak is important as it corresponds to maximum displacements. What is more important is the gain (or the insertion loss), and the bandwidth over which the response is high. Likewise from Equation (3.35) it

is possible to use this location to determine the peak amplitude of $H(\pi f / f_0)$ as Equation (3.37) and plotted in Figure 3.9.

$$f_{max} = \begin{cases} \frac{4}{Z_r} & Z_r < \sqrt{2} \\ \frac{Z_r^3}{Z_r^2 - 1} & Z_r \geq \sqrt{2} \end{cases} \quad (3.37)$$

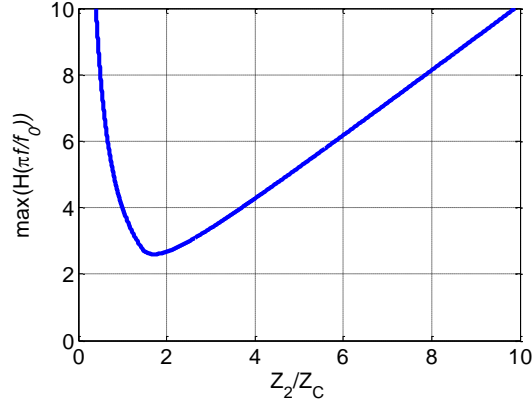


Figure 3.9: Maximum value of $H(\beta_a l)$ as a function of the ratio of Z_2 and Z_C

Intuitively the maximum energy should occur when the the transducer and the material Z_2 are closely matched, however this is not the case. The reason for this is that when there is a large mismatch, each of the multiple layers are allowed to build up in the effectively trapped mode. This will however limit the bandwidth in these regions. The bandwidth can be defined as the half power points in the $H(\pi f / f_0)$. Due to the split in the peaks going from the middle towards the $f_0/2$ locations there are three regions for the bandwidth defined as in Equation (3.38), and plotted in Figure 3.10.

$$f_{max} = 2f_0 \left(1 - \frac{1}{\pi} \cos^{-1} \left(-\frac{Z_r^2}{Z_r^2 - 2} - \sqrt{\left(\frac{Z_r^2}{Z_r^2 - 2} \right)^2 + 1} \right) \right), \quad Z_r < \sqrt{2}$$

$$f_{max} = 2f_0 \left(1 - \frac{1}{\pi} \cos^{-1} \left(\frac{2 - \frac{Z_r^2}{\sqrt{Z_r^2 - 1}}}{2 - Z_r^2} \right) \right), \quad \sqrt{2} \leq Z_r \leq \sqrt{4 + 2\sqrt{2}} \quad (3.38)$$

$$f_{max} = \frac{f_0}{\pi} \left[\cos^{-1} \left(\frac{2 + \frac{Z_r^2}{\sqrt{Z_r^2 - 1}}}{Z_r^2 - 2} \right) - \cos^{-1} \left(\frac{2 + \frac{Z_r^2}{\sqrt{Z_r^2 - 1}}}{2 - Z_r^2} \right) \right], \quad \sqrt{4 + 2\sqrt{2}} < Z_r$$

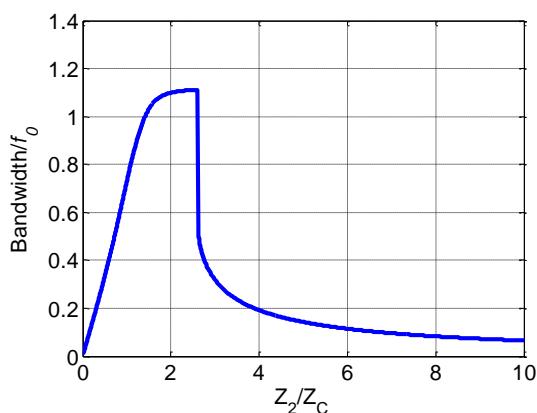


Figure 3.10: Bandwidth of $H(\pi f / f_0)$

The maximum bandwidth appears to occur at η_r values larger than the matched impedances case, and then rolls off quickly. This is somewhat deceptive as in the second region of Equation (3.38) the passband is not flat, due to the response shifting from half wavelength resonance to quarter wavelength resonance. This distortion in the passband causes additional ring down in the time domain response, effectively decreasing the bandwidth. Ultimately this is an approximation of the actual performance and $H(\pi f / f_0)$ does not include the complete frequency dependent behavior of the system, given the $1/f^2$ term in Equation (3.34). Therefore, to get an accurate assessment of device performance numerical solutions are needed.

Returning back to Equation (3.32) the more exact form does not have a closed form solution from which to determine the center frequency, maximum efficiency and

bandwidth. Though the value of C_0 cancels, the value of k_t^2 does not. As such a value of $k_t^2 = 0.07$ will be used as an approximation of Aluminum Nitride (AlN). Solving these numerically result in the following plots.

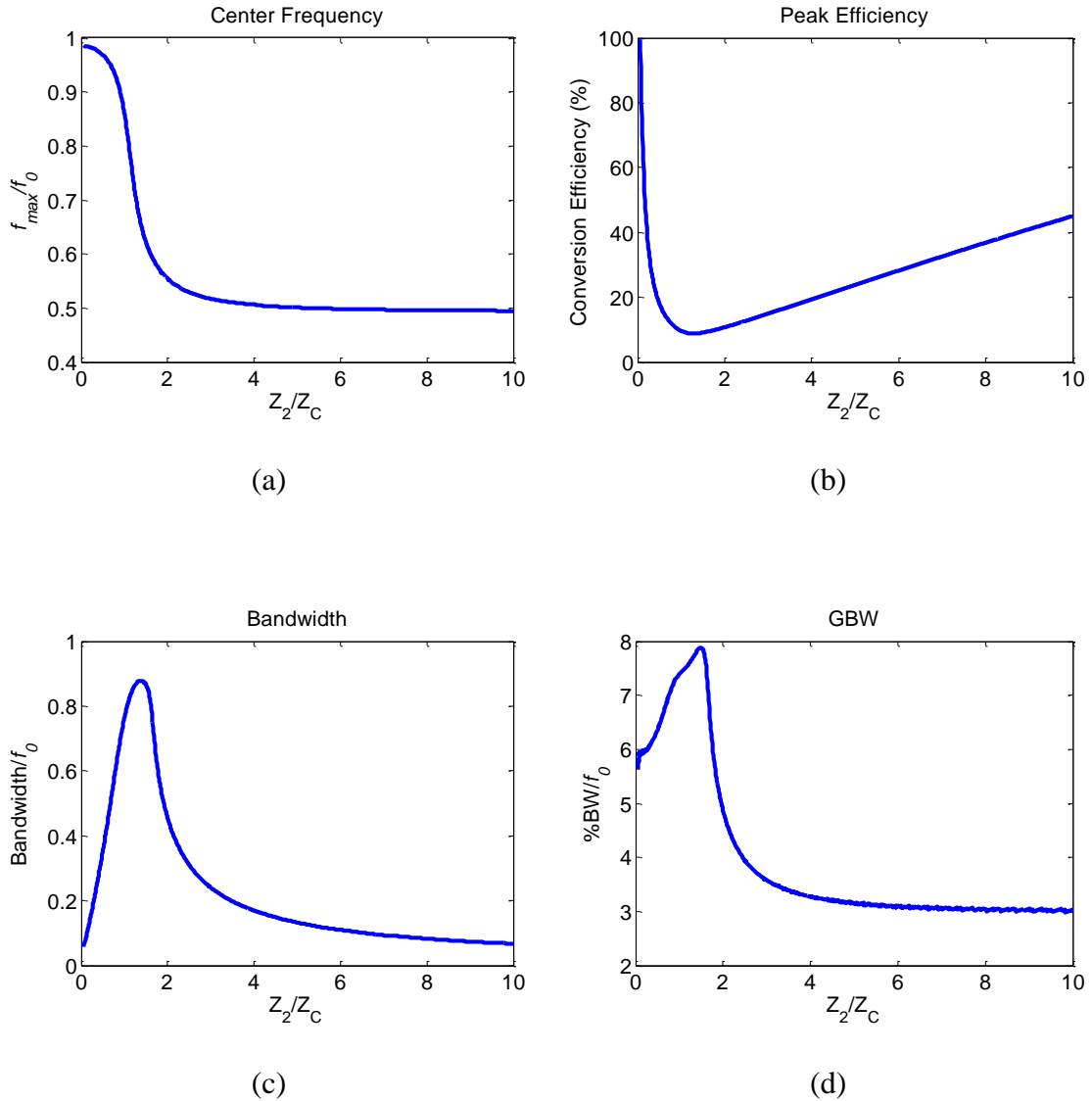


Figure 3.11: Performance metrics of power conversion as a function of impedance ratio η_r , (a) Center Frequency (b) peak value of the response (c) Bandwidth, taken as the half power point (d) Product of the peak value and the bandwidth

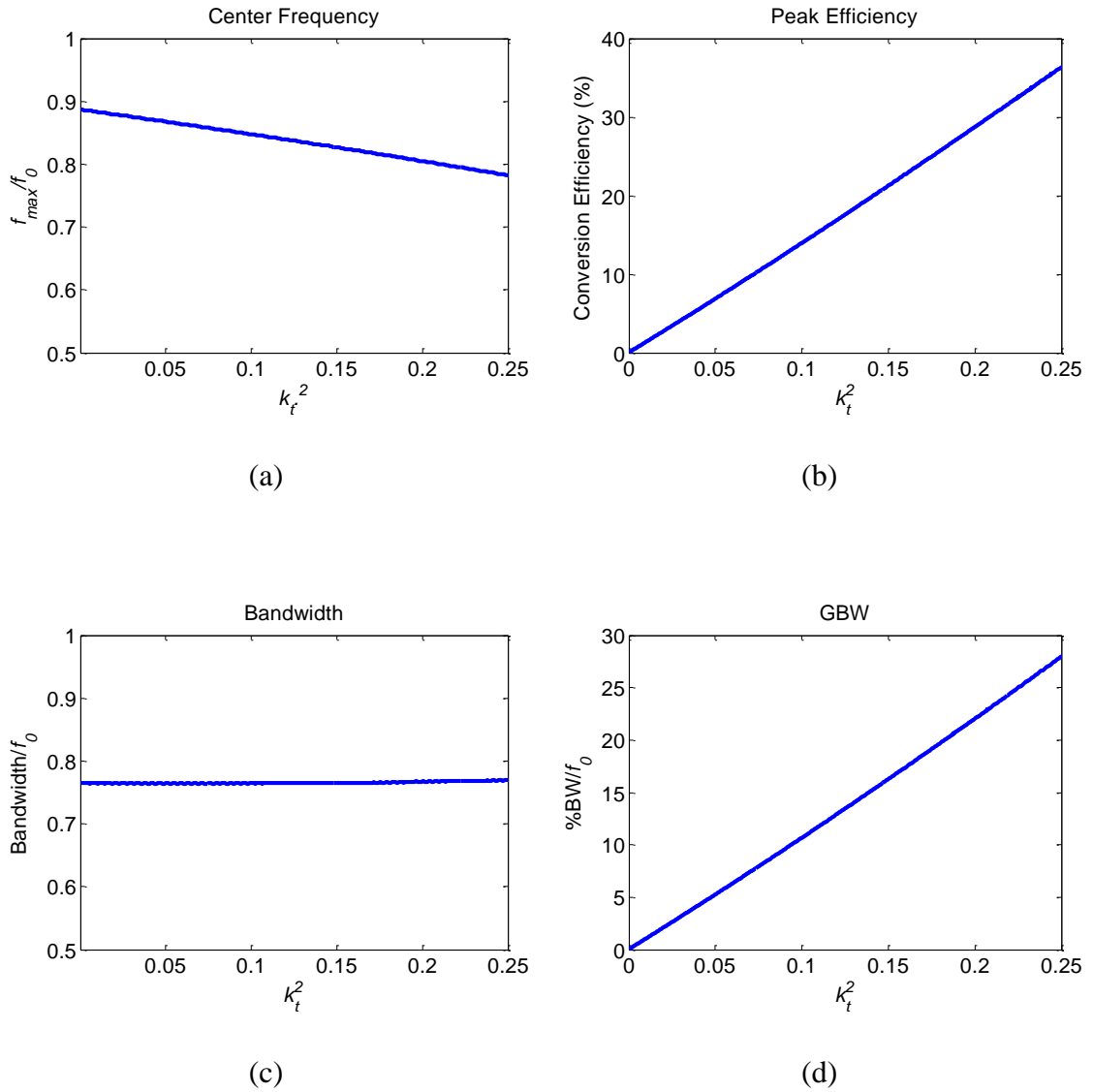


Figure 3.12 Performance metrics of power conversion as a function of coupling efficiency k_t , (a) Center Frequency (b) peak value of the response (c) Bandwidth, taken as the half power point (d) Product of the peak value and the bandwidth

The trend in center frequency is similar to Figure 3.8, it is nearly at f_0 and shifts to $f_0/2$ for large values of η_r . It does shift at lower ratios than $H(\pi f / f_0)$, at the matched case the center frequency has already reduced to $0.8836 f_0$. The trend for the peak

value is very similar to that shown in Figure 3.9. The minimum occurs near unity, with a η_r of 1.2751 and a value of 8.79%. The maximum value of the bandwidth occurs near this when η_r is 1.3647 the bandwidth is $0.8786 f_0$.

All of these values were solved for when the coupling efficiency k_t^2 was 0.07. Intuitively as a measure of efficiency, one would expect that increasing k_t^2 would result in a linear increase in peak efficiency. Taking the matched case ($\eta_r = 1$) and sweeping k_t^2 results in the changes to these parameters seen in Figure 3.12.

The maximum value of k_t^2 for the plots shown was chosen as it is in the neighborhood of the largest k_t^2 for piezoelectric materials [73]. While the value of the center frequency decreases with increasing k_t^2 , the peak efficiency has a linear dependence on k_t^2 . The bandwidth is almost independent of k_t^2 over this range of values and therefore the gain bandwidth product increase exponentially with k_t . Therefore, there is great benefit in performance if a material with higher coupling coefficient can be used. Unfortunately, many of the high coupling coefficient materials do not have a CMOS compatible process flow at the moment.

While it would be easy to state that the peak values found here represent the best designs to use, there are limitations to this method of modelling which require other methods to be utilized. For instance, the power factor is a real scalar value, however the phase of the acoustic signal from the transducer (either force/pressure or particle velocity) is important in that distortions in the phase can effectively decrease the bandwidth of the signal and contribute to the bit error rate of the channel. As such this method does not provide a way of relating the phase of input signal (V/I) to the output signal (F/v).

Furthermore, the setup described an air backed transducer. This type of transducer is exactly the same the previously described HBAR. As such it has a very limited useable bandwidth, requiring something to be done about multiple reflections to so

that no resonances can develop. In the air backed case the acoustic energy can only flow from one port, however when both ports are connected to real loads there is no way of determining the partition of energy in each port from the lumped model approach. The parameters k_t^2 and η_r cannot truly be designed for as there are a limited selection of CMOS compatible piezoelectric materials, and silicon, though additional mechanical matching layers can be designed. All of these factors contribute to the use of circuit modelling techniques in the next section.

3.6 KLM Model

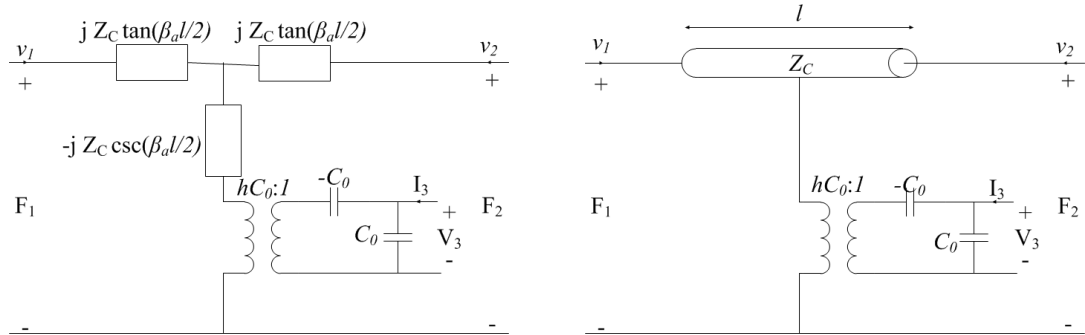


Figure 3.13: Mason and Redwood models

It has been common practice since Mason [50], to model the transducer as an equivalent electrical circuit, with an electrical side and a mechanical side separated by a transformer. By doing this it creates a model which allows for the addition of input and output impedances of preceding and subsequent circuitry to be modelled with the transducers or mechanical layers as impedances, real or complex transmission lines. All attempts to model the channel start from the results in Equation (3.18), and then treat the force as voltage and particle velocity as current. Mason's model was the first created this way, where he treats the conversion of electrical to mechanical as a transformer and simply related the three ports using a T-network, where each

impedance is frequency dependent and is directly translated from the coupled equations in Equation (3.18).

Though it is credited and named after him in the original paper, Redwood identifies his model as Mason's model [74]. The Redwood model replaces the T-network in in Mason's model with an equivalent co-axial cable or transmission line. While this is closer to a physical representation it is difficult to use in analytical derivations due to the ambiguity in the connection of the grounding shield and the negative capacitance. Even so, it is much more useable in circuit simulation software.

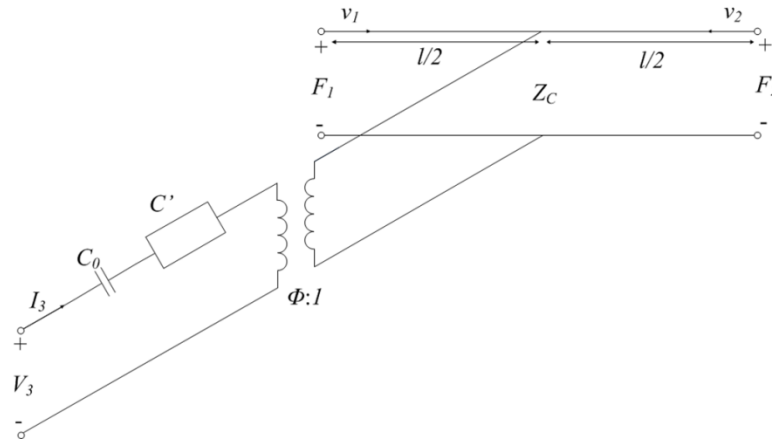


Figure 3.14 KLM Model

The KLM model, first introduced in [75], and seen in Figure 3.14, is beneficial for running simulations as well as time domain analysis. The parameters in Figure 3.14 are:

$$\phi = k_t \sqrt{\frac{\pi}{\omega C_0 Z_{CA}}} \text{sinc}\left(\frac{\omega}{2\omega_0}\right) \quad (3.39)$$

$$C' = -\frac{C_0}{k_t^2} \frac{1}{\text{sinc}\left(\frac{\omega}{\omega_0}\right)} \quad (3.40)$$

The challenge of using the model, especially for circuit simulation software is that the turns ratio, ϕ , is a function of frequency. Even so, it is a good model for the physical behavior in generating acoustic waves. In this case the conversion from electrical to acoustic occurs at the center of the transducer and generates waves which propagate towards both acoustic ports. While this is not physically true, as the entire thickness of the transducer contributes to wave generation, it does help illustrate the frequency response of the transducer.

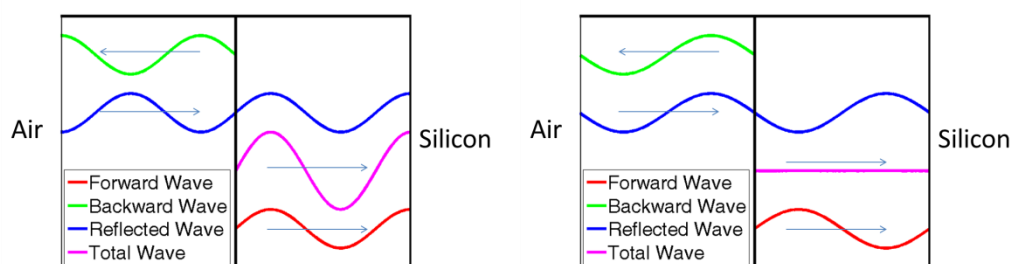


Figure 3.15: Wave generation from transducer

Consider the two cases demonstrated in Figure 3.15. The left side for each case is air, or a reflecting boundary condition, whereas the right is silicon, an absorbing boundary. Waves are considered to have been generated at the center of the transducer and propagate forwards (toward the silicon) and backwards (toward the air “backing”). The air presents a perfect reflection condition so that backwards travelling waves are completely reflected with a 180 degree phase shift. For simplicity consider perfect matching between the transducer and silicon. When the transducer is an odd multiple of half wavelengths, (the $5/2$ wavelength thick condition is illustrated in the left image in Figure 3.15), then the phase of the reflected back traveling wave, and the forward traveling wave add up perfectly and maximal signal is obtained. When the transducer is an integer number of wavelengths (the 2 wavelengths thick condition is illustrated in

the right image in Figure 3.15), then the phase of the reflected back traveling wave is 180 degrees out of phase with the forward traveling wave, leading to no signal being transmitted. This leads to a peak signal near the resonance frequency which rolls off to some finite bandwidth. If the silicon is not directly matched to the transducer, then the forward wave will also have some portion reflected. This manifests in the response of the system as a decrease in the bandwidth. This line of thinking is not exact as seen in the previous section the peak response is slightly lower than resonance for the matched case.

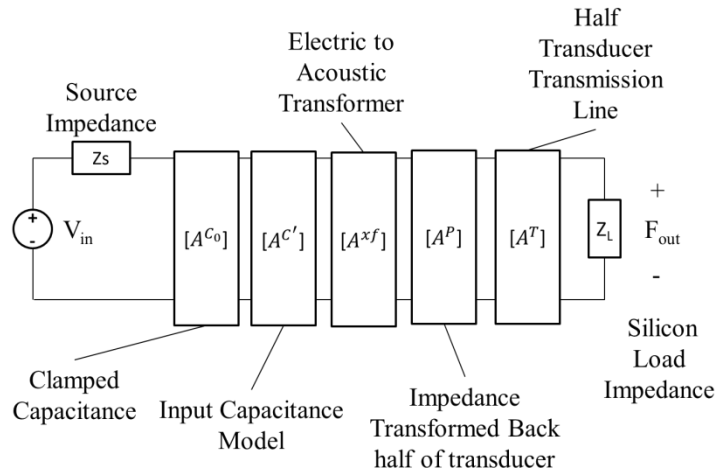


Figure 3.16: ABCD representation of the transducer in transmission

The closed form solution of the transducer transfer function is rather intractable. Instead simulations are performed using microwave circuit techniques. Each impedance element in the KLM model is represented by its ABCD matrix. The ABCD chain for the transmit configuration is shown in Figure 3.16. The output is the force and particle velocity entering into the silicon. The unit A^P is an impedance transform of the back half of the transducer. Modeling the system this way allows for the inclusion of parasitic electric circuit elements at the input of the transducer, including the source impedance Z_s . Likewise, mechanical layers on either the bottom or top of

the transducer can be modeled as transmission lines attached after A_T or transformed through A_P respectively.

In order to model the receive behavior, the force acquired from the transmit simulation is applied to the mechanical port of the transducer, through the silicon radiation impedance. Then the process uses the ABCD matrices in reverse order, with the only caveat that the transformer matrix is inverted, since it is going the other way through the turns ratio.

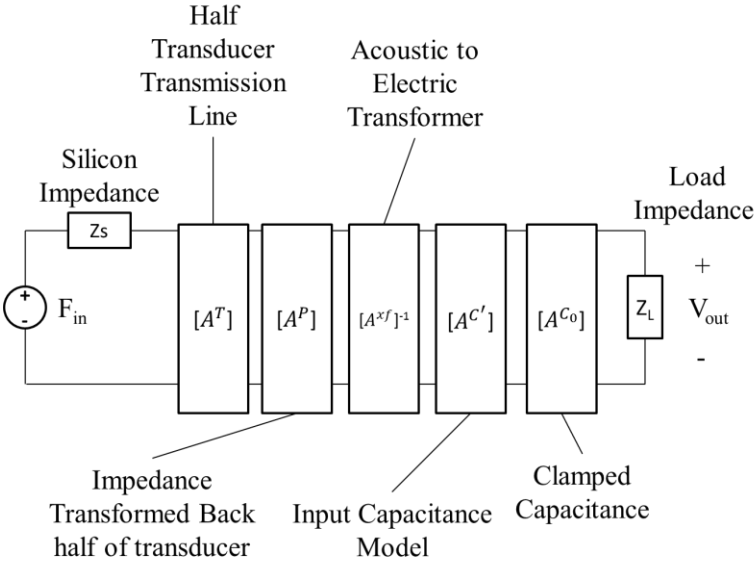


Figure 3.17: ABCD representation of transducer under receive

From this model, the behavior of an acoustic communication channel can be modeled. The entire channel can be modeled as a voltage frequency transfer characteristic, where the signal on the receive transducer, attached to an open circuit, is some fraction of transmitted signal from the transmitting transducer. A simulation of an aluminum nitride transducer to silicon channel is shown in Figure 3.18. Likewise is can be used to determine the power conversion and will generate the exact same plots

seen in Figure 3.11. Since the explicit mechanical signal at each port is modelled it allows for the examination of the phase of the signal at each port.

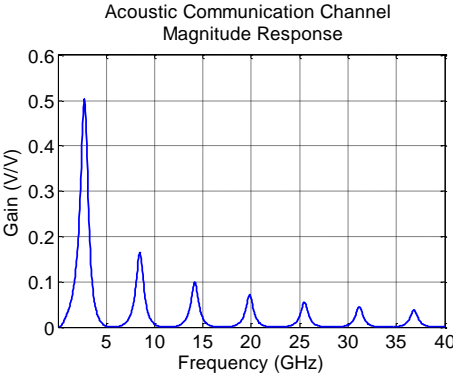


Figure 3.18: Ideal transducer magnitude response function

The primary peak is at the half wavelength resonance, approximately 2.7 GHz for the 1.5 μm thick transducer using the Sandia properties for aluminum nitride [76]. Each subsequent peak is of lower amplitude, an effect which is independent of intrinsic material loss (though loss will contribute as well). It occurs since higher resonant peaks include whole wavelengths. In the piezo the positive and negative charge generated by the positive and negative peaks of the full wavelength cancel, leaving a smaller effective area of the transducer generating charge.

Using the KLM model, it is possible to design various mechanical layers in order to shape the transfer function of the primary resonance to more desirable characteristics. Again, the primary design considerations here will be the center frequency of the transducer, the bandwidth, and the peak response value. This design work resulted in a stack design with the Institute for Microelectronics, a collaboration with the IARPA TIC program and resulted in a paper for the International Ultrasonic Symposium [77]. In order to ensure high quality factor and electromechanical coupling coefficient several of the layers are fixed. Since the diamond crystal lattice of

the silicon does not match the Wurtzite crystal of the aluminum nitride, a buffer layer is needed. While other materials may offer more desirable mechanical characteristics, silicon dioxide is a good choice of material since these transducers will eventually be fabricated on a CMOS stack. In order to ensure correct crystal growth of the AlN, a seed layer of AlN is needed followed by a metal which grows with the crystalline structure similar to that of AlN. The process developed at IME uses molybdenum seed layer. The top electrode is also molybdenum. Finally, the device is capped with silicon dioxide as well to provide a protective barrier. While these layers are fixed, the thickness of each layer can be adjusted within the range shown in Figure 3.19.

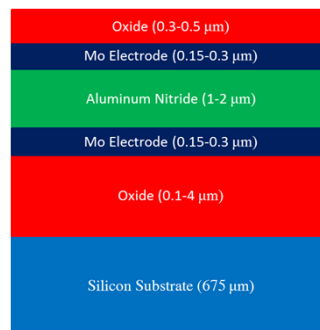


Figure 3.19: Transducer cross section with annotated thickness ranges for design space

The first parameter to explore is the thickness of the aluminum nitride transducer itself. Recall from the section on FBARs, that the resonance frequency can be determined from (3.25). Here there is a simple and easy inverse relationship between the resonance frequency and the thickness of the material. The bandwidth and peak response do not have nice closed form solutions. The results of sweeping the thickness of AlN from 1 μm to 2 μm is shown in Figure 3.20.

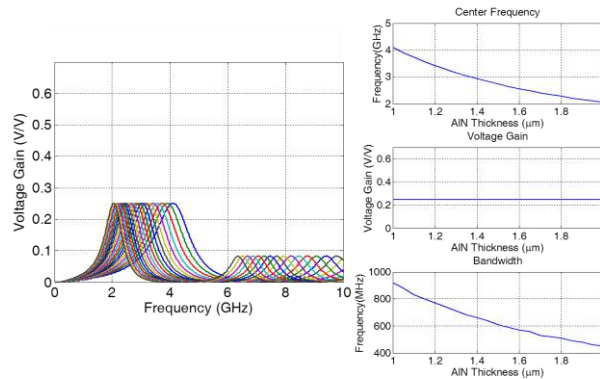


Figure 3.20: Effect of AlN film thickness on transfer function

As expected, the center frequency decreases as the thickness increases. As previously established, the transducer bandwidth decreases with increasing transducer thickness, linearly with the center frequency. Interestingly, though not entirely surprisingly, simulations show that the amplitude of the peak response does not depend on thickness, as it is related to the k_t^2 and other material properties. For subsequent simulations, an AlN thickness of 2 μm is chosen as the foundry can confidently provide films as thick as 2 μm . This limit is due to fabrication limits of vias connecting the top and bottom metal electrodes.

Next consider the top layers; the top oxide and the top Mo metal electrode. To visualize the effect consider Figure 3.15 for the way waves are generated in the transducer. If instead of air there were another material, within an order of magnitude acoustic matching to aluminum nitride then the frequency at which the forward and backward waves would shift, depending on how thick this backing material is. Since the backing material is not a perfect match for aluminum nitride it will diminish the bandwidth some. Since we have access to microfabrication technique the layers can be created precisely as thick as desired. Though not shown here, one benefit is that

having a thin transducer results in a low output impedance, but adding the layer keeps the output impedance low while decreasing the frequency response. The results of simulations of the silicon dioxide and Mo backing layers are shown in Figure 3.21 and Figure 3.22.

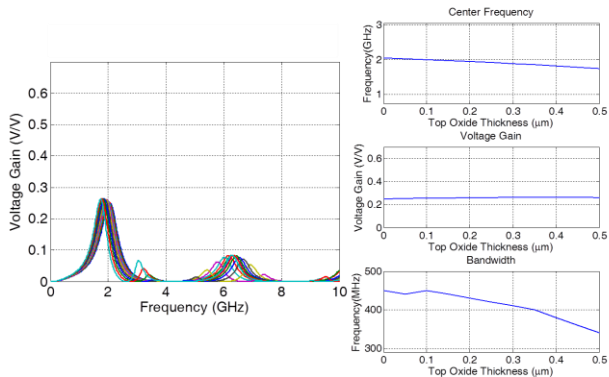


Figure 3.21: Effect of the silicon dioxide backing layer

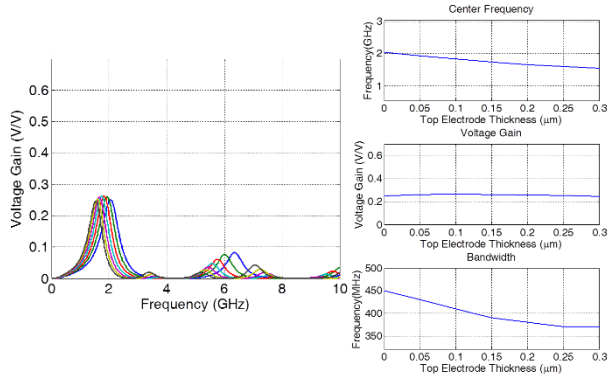


Figure 3.22: Effect of the top Mo electrode

As expected increasing the thickness reduces the resonant frequency and bandwidth, while the effect on the amplitude is minimal. The thickness of the oxide film is a good design layer which can be used to lower the center frequency, and can even be tuned after fabrication at the foundry by depositing additional oxide films.

The effects of increasing the top metal is similar to oxide however the material properties of Mo compared to oxide do cause a slight change. The acoustic impedance and density of Mo is much greater than AlN whereas oxide is less than AlN. This results in a greater shift in center frequency and reduction in bandwidth for a thinner layer.

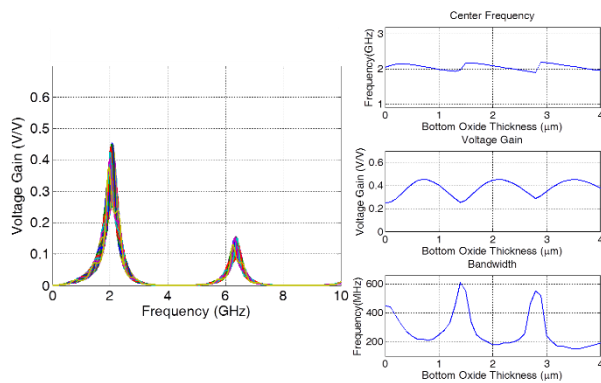


Figure 3.23: Effect of bottom silicon dioxide layer

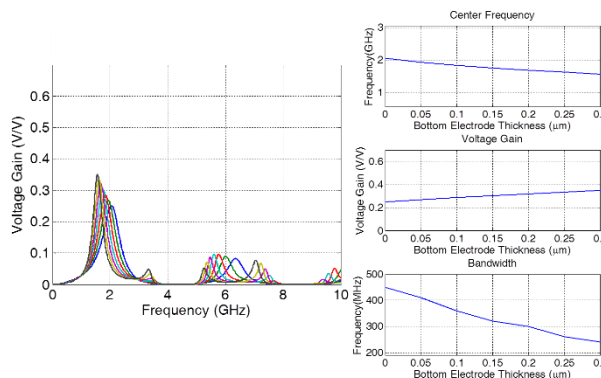


Figure 3.24: Effect of bottom electrode layer

Adding layers to the bottom does not shift the frequency as it does on the top. The quarter-wavelength matching layer is a common method for increasing amplitude, though over a narrow bandwidth. Neither silicon dioxide nor Mo have the ideal value

of impedance for quarter wavelength matching, they do both affect the response and can be optimized. The results of these sweeps are shown in Figure 3.23 and Figure 3.24.

Though it is not the ideal value for a quarter wave matching layer, the effect the oxide has on the response is similar. Firstly, as expected there is only a small shift which occurs in the center frequency. What is interesting is that while there are regions where the amplitude increases as expected; there are also regions where the bandwidth increases instead. Allowing for the selection of a layer for increased bandwidth instead of increased amplitude, especially considering there is an increase in bandwidth of over 100% while the reduction in gain is only 30%.

The bottom electrode has much higher acoustic impedance than oxide, which results in a very different effect on the transfer function. If the medium the transducer is transmitting into has lower acoustic impedance, such is the case when going into oxide or silicon, the response shape is around the half wavelength resonance as described. This is due to the boundary condition of the resonant mode, such that there are antinodes at each face. If the material has significantly higher acoustic impedance, approaching an open circuit in the KLM model, then the boundary condition at the transmitting surface changes from an anti-node, to a node and the transducer begins to act as a quarter wavelength resonant transmitter. Since this is only caused by a large impedance mismatch at the transmitting face, it does result in a significant decrease in bandwidth, though it does lead to an increase in the transmitted amplitude. As the bottom electrode becomes thick with respect to wavelength, the transmitting condition shifts more towards the quarter wavelength mode.

All of these effects superimpose and the final design choices were as follows. The transducer layer thickness was as large as possible to reduce the resonance frequency as low possible, the goal for the work with IME was transducers at lower frequencies.

Then the backing layers were chosen as thick as possible to reduce the resonance frequency further while maintaining relatively low output impedance. The bottom electrode was chosen as thin as possible to maintain the half wavelength behavior, due to its wider bandwidth. Finally, simulations were redone with the full stack to determine the thickness of the bottom oxide and an optimal value of 2 μm or 4 μm are chosen due to the wider bandwidth. The results of this simulation sweep is plotted in .

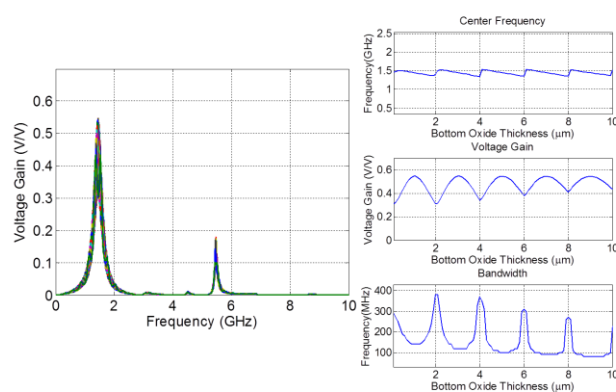


Figure 3.25: Simulation of full stack sweeping bottom oxide layer

After the transducer design was completed sample structures were fabricated at IME. The transducers were scanned near the resonance frequency and the result is plotted in Figure 3.26. Previous transducers from IME yielded signal levels of 200 μV at peak. The new design has signal level at peak of 18 mV at 1.3 GHz, a tremendous improvement enabling a higher SNR for chip-scale sonar. The signals for both the measured data and the simulations shown in are lower, than calculated in the previous simulations, where the gain was between 0.25 V/V to 0.5 V/V. This is due to the input impedance of the receivers, which were 50 ohms, greatly reducing the signal level, a common challenge with circuit board level testing of micro-sonar. Furthermore,

differences in the signal levels from the simulated and measured are due to the parasitic capacitance and resistance of the test circuit board itself.

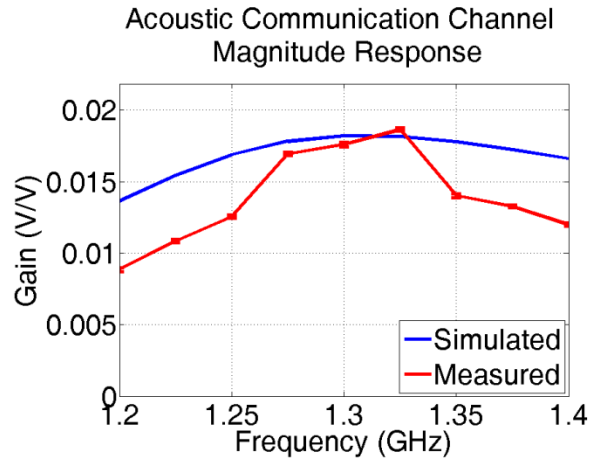


Figure 3.26: Measured acoustic communication channel magnitude response of designed stack

The one dimensional analysis presented here is beneficial for understanding the efficiencies of transducers and appropriate design. For applications in communication in silicon however it becomes important to investigate 2-D and 3-D effects. The next chapter will cover phased array theory and element radiation patterns, in order to consider these effects in design.

3.7 *Transducer Noise Figure*

For the purposes of a communication channel it becomes important to know the sensitivity of the signals. This will dictate the link budget of the channel and allow for meaningful comparison with other technologies.

There are three types of loss commonly referred to in electronic design; (1) Johnson or thermal noise, (2) Flicker or $1/f$ noise, and (3) shot noise. The thermal

noise is the most common source and is well modelled. In general a resistor generates thermal noise of the form

$$V_n = \sqrt{4k_B TR\Delta f}. \quad (3.41)$$

Thermal noise is classified as white since the spectrum is flat or independent of frequency across frequencies upto high THz frequencies. This is the most important type of noise in ultrasonic transducers. Flicker noise is associated with low frequencies (as the $1/f$ title suggests). Though the physical phenomenon are not fully classified based on theoretical limits it is negligible for ultrasonic transducers in the MHz [78]. Shot noise is a well understood quantum mechanical phenomenon which occurs due to the fact that charge is quantized. However, it is a phenomenon which arises in steady state currents, of which piezoelectric transducers do not operate with a DC bias point, again making it negligible.

The primary acoustic white noise source can be modelled from the radiation impedance. For the one dimensional model this is Z_{1A} or Z_{2A} from Equation (3.20) or Equation (3.21). Consider again the air backed case, and the acoustic noise, which is the noise on the acoustic terminals of the transducer, can be modelled by treating the noise from the real part of the radiation resistance.

$$F_n^2 = 4k_B TZ_{2A} \quad (3.42)$$

Where for the air backed case the value of Z_{2A} is real, in general this noise can be found from the real component of Z_{2A} . The value of the noise voltage and the output of the transformer is this noise force filtered by the force transfer function. From the KLM ABCD design section the entire channel can be simplified on the receive side

from Figure 3.17. If we take this to be a filter relating the input (Force) to the output (Voltage) such as the form of Equation (3.43).

$$G_r(f) = \frac{V_r(f)}{F(f)} \quad (3.43)$$

Since this noise then passes through this filter the acoustic noise at the output of an unloaded transducer is then defined as

$$|V_{rn}(f)|^2 = |G_r(f)|^2 4k_B T Z_{2A}. \quad (3.44)$$

This represents the thermal noise limit of the transducer. However, this is not the only source of noise. In traditional ultrasound systems the transducer is separated from the interfacing electronics, often by long transmission lines. As such the analysis often incorporates the loss in these connections [78] [79]. For the integrated micro-sonar the cables connecting the transducer to the amplifier are short. There are however losses associated with the intrinsic loss of the materials in the transducer stack. It is possible to define a mechanical quality factor which relates to the viscoelastic loss co-efficient defined in Equation (2.30), in Equation (3.45)

$$Q_m = 4.343 \left(\frac{2\pi f}{V_a \alpha} \right) \quad (3.45)$$

This value is frequency dependent and specific to each material in the transducer stack. This manifests itself in the acoustic impedance of each material as Equation (3.46)

$$Z_{mech} = Z_a \left(1 - \frac{j}{2Q_m}\right) \quad (3.46)$$

Where Z_a is the characteristic acoustic impedance of the material defined as in Equation (2.13) , and Z_{mech} is the characteristic impedance including the intrinsic material loss. As the piezoelectric transducer is physically the same as a capacitor another source of loss is involved with the dielectric loss tangent, this results in the clamped capacitance of the transducer to be effectively complex as seen in Equation (3.47).

$$C_0 = C_{0,real}(1 - jTan(\delta)) \quad (3.47)$$

All of these effects can rolled together and modelled as a Thevenin equivalent voltage source with Thevenin equivalent impedance representing the collective effects of all the noise sources. Such a system is designed such that the transducer is driving load R_r . The input impedance in this case, incorporates all of the loss mechanisms described by Equation (3.46) and Equation (3.47). The noise generated by this system (neglecting the load resistors noise for now) is written as

$$|V_n(f)|^2 = 4k_B T Re(Z_{in}(f)) \left| \frac{R_r}{Z_{in}(f) + R_r} \right|^2 \quad (3.48)$$

To determine the contribution of the acoustic power in this condition requires an adjustment to the expression in Equation (3.44). Recall that the filter defined in Equation (3.43) is defined for the open circuit condition. This therefore represents the Thevenin Equivalent voltage source, which is a function of the applied force. Since

this now has a load resistor the acoustic noise needs to be adjusted from Equation (3.44) to the value seen in Equation (3.49).

$$|V_{rn}(f)|^2 = |G_r(f)|^2 4k_B T Z_{2A} \left| \frac{R_r}{Z_{in}(f) + R_r} \right|^2 \quad (3.49)$$

The noise figure, a figure of merit for the transducer is the ratio of the noise power on the output to the thermal acoustic noise; the theoretical lower limit. This is accomplished as the ratio of Equation (3.48) and Equation (3.49), resulting in Equation (3.50).

$$NF_t = \frac{Re(Z_{in}(f))}{Z_{2A} |G_r(f)|^2} \quad (3.50)$$

Notice that the load resistance cancels from this expression. This is significant as it shows that it is independent of the load. It is worth noting that this expression does yield unity if the transducer is modelled without any material loss, and the unity condition represents the lower bound on transducer noise.

Chapter 4

Radiation Patterns for GHz Ultrasonic Phased Arrays

A 1-D communication channel was modelled in the previous Chapter. In 1-D the waves generated and detected are plane waves. In 2-D and 3-D the phenomenon of diffraction becomes important. Diffraction occurs due to waves sources from finite apertures such that not all spatial harmonics are available to make perfect plane waves. When there are two transducers used as a communication channel transmit and receive elements, diffraction spreads the wave energy such that the receiving transducer only receives a fraction of the transmitted energy. Diffraction loss will be covered in Section 4.2

Antenna array theory is common both to electromagnetics (RADAR or RF communication [80]) and ultrasonic imaging (SONAR or medical imaging [81]). A directional antenna is more desirable than an isotropic one because it results in higher signal to noise ratio due to lower $1/r^2$ loss, but it has the downside that the signal is confined to a direction. In order to scan an area with a directional antenna, one has to physically scan across a region. Using array theory it is possible to apply different phases to an element array and create and control a directional beam electronically, combining the advantages of an isotropic emitter with the focus of a directional antenna. The system complexity however becomes higher as it requires high frequency electronics power and volume.

Phased arrays behaves very similarly to a transducer of the same physical size. Due to the periodicity of the array however, the steerable beam formed can be narrower in angular spread, due to the way the phases constructively interfere. First we consider the radiation pattern from a single transducer which can be arrayed later.

4.1 *Radiation Impedance*

The acoustic impedance for a material is defined by the ratio of pressure to particle velocity [69]. For plane waves this value is the characteristic impedance dependent only on material properties. For other geometries though the original definition seen in Equation (2.12) must be used and can result in impedance dependent on the profile of the transducer.

$$Z = -\frac{T}{v} \quad (2.12)$$

The simplest case to consider is a sphere, with radius a , which generates spherical waves traveling outward from its center. To begin, it is useful to define a scalar wave potential, which is related to the particle displacement as

$$u = \nabla\phi \quad (4.1)$$

This parameter also obeys the wave equation defined in Equation (2.9). The sinusoidal steady state solution of the wave equation for a perfectly spherical wave is of the form

$$\phi = \frac{Ae^{-jkR}}{R} \quad (4.2)$$

The relationship between the pressure T and the scalar wave potential is

$$T = \omega^2 \rho_{m0} \phi \quad (4.3)$$

The relationship between the scalar wave potential and the particle velocity can be found from the time derivative of Equation (4.1).

$$v = j\omega \frac{d\phi}{dR} \quad (4.4)$$

Using Equation (4.3) and (4.4) with (2.12) results in an expression for the spherical wave impedance shown

$$Z = \frac{k^2 R^2 + jkR}{1 + k^2 R^2} Z_0 \quad (4.5)$$

Where Z_0 is the characteristic impedance of the material the spherical waves are travelling in. As kR becomes larger, at large radius or large k (small wavelength), the radiation impedance approaches the characteristic plane wave impedance. For small kR the real portion of the radiation impedance becomes small, meaning that for an applied stimulus only a small portion of real power is generated into the acoustic medium. The details of this can be seen in the acoustic power, taking the form of Equation (4.6).

$$P = 2\pi R^2 Z v v^* \quad (4.6)$$

By substituting the expressions in (4.2) (4.4) and (4.5) into (4.6) and using the boundary condition, where the particle velocity at the surface of the sphere is denoted $v(a)$, results in the power emitted from a spherical radiator as Equation (4.7).

$$P = \frac{2\pi a^2 Z_0 \left(k^2 a^2 + \frac{jk a^2}{R} \right)}{1 + k^2 a^2} |v(a)|^2 \quad (4.7)$$

The real portion of power is independent of R , in agreement with the first law of thermodynamics. The intensity however, which is power through area, falls off as $1/R^2$. For large values of a , the real portion of the power is approximately related to a^2 . At larger a , a large number of wavelengths can fit the aperture. If however a , and specifically ka is small, then the real portion of the power is approximately related by a^4 . In this region most of the power is reactive and very little real power is transmitted. Though here this is shown for a radiating sphere, the principle holds for small planar transducers as well [69].

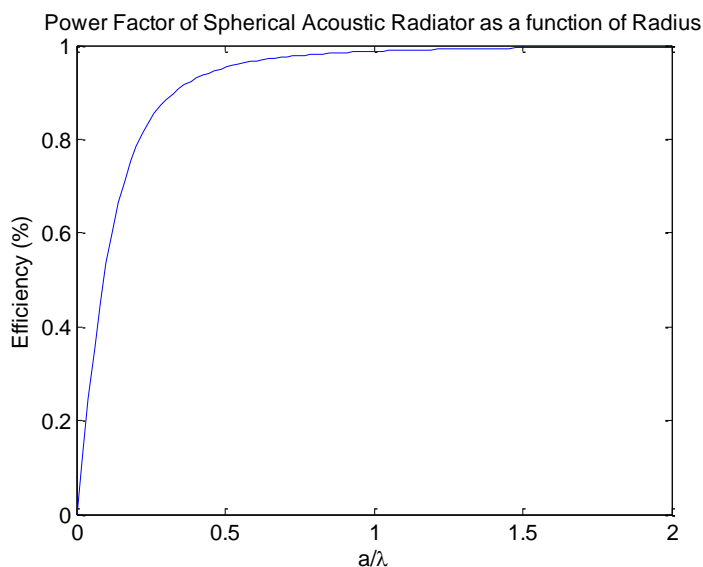


Figure 4.1: Power factor of Equation (4.7) as a function of radius normalized to wavelength λ

The efficiency of the transducer as a function of the size can be determined by the power factor of Equation (4.7). This is plotted in Figure 4.1. When the radius is half of a wavelength the power factor efficiency is 95%, and it rolls off rapidly as the size approaches zero. Commonly the design of transducer is such that the size of the

transducer is on the order of a half wavelength or larger. This is a very common design constraint for RF antennas as well. The benefit of using ultrasonics on chip is that an acoustic wavelength is 5 orders of magnitude smaller than an RF wavelength at the same frequency. Therefore an efficient acoustic transmitter at 1 GHz in silicon is $\lambda/2 \sim 4 \mu\text{m}$, compared to multiple cm for an RF antenna, operating at the same frequency. As will be covered in the phase arrays section, the optimal spacing between elements is a half wavelength, allowing for similarly sized transducers, operating at an efficient size scale. Furthermore though half wavelength transducers are on the edge of good efficiency of transducers, in an array the effective aperture of all the elements sets the size scale of the full transducer and acoustic impedance leading to a real valued impedance [78].

4.2 Transducer Radiation Pattern

In order to model the diffraction, and thereby the radiation pattern of a transducer starts with the application of Huygens-Fresnel Principle. At any given point in time the current wave front can be treated as a series of infinitesimal spherical wave sources. The superposition of the sources can be used to predict the wavefront at any subsequent time and point in space. The solution obtained this way is achieved through Rayleigh integral method resulting in a series of equations known as the Sommerfield Diffraction Equations.

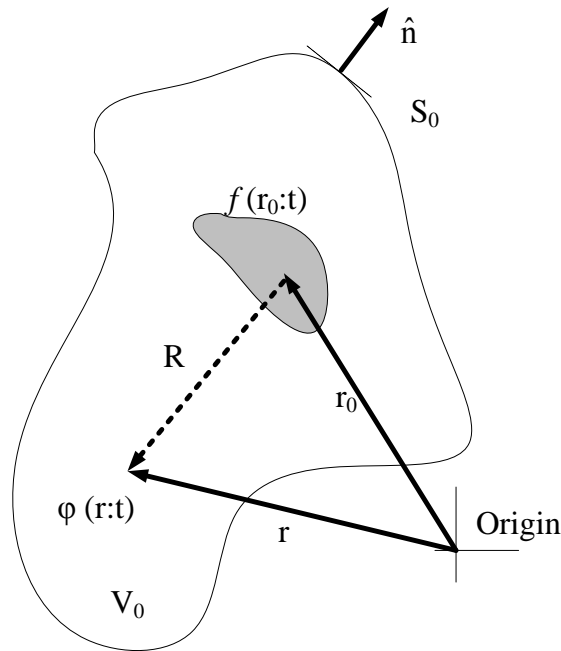


Figure 4.2: Setup for Green's Function method

A common method of accomplishing this is known as the Green's function method [[69], [81] [82]]. There is a collection of spherical wave generators collected together in a "cloud" denoted by the gray color [Figure 4.2]. The objective is to determine the field potential at some arbitrary location r given this source potential. Each radiator within this "cloud" at position r_0 has a strength of $f(r_0:t)$. This cloud is contained within some volume V_0 , enclosed by some surface S_0 , and the vector \hat{n} is the outward facing normal of S_0 . S_0 is chosen to utilize Gauss's theorem. To setup this condition, waves propagating from this source must obey the wave equation, which is adjusted from Equation (2.9) to include the driving function in

$$\frac{1}{V_a^2} \frac{d^2 \phi}{dt^2} - \nabla^2 \phi = -f(r_0:t) \quad (4.8)$$

Transforming this expression into the frequency domain yields what is known as the inhomogeneous form of the Helmholtz equation, in Equation (4.9).

$$(\nabla^2 + k^2)\Phi = -F(r; \omega) \quad (4.9)$$

It is convenient here to define a function type known as Green's function. Qualitatively a Green's function is the impulse response solution to the inhomogeneous Helmholtz equation, much in the same way a filter can be defined by an impulse response function. As a solution to Equation (4.9), it can be seen explicitly as

$$(\nabla^2 + k^2)G(r|r_0) = -\delta(r - r_0) \quad (4.10)$$

Where $G(r|r_0)$ is a Green's function solution. As stated before, the method here results in a pattern generated from the superposition of a series of infinitesimal spherical sources. In this case the free space Green's function for a spherical source is defined as

$$G(r|r_0) = \frac{e^{-jkR}}{4\pi R}, R = |r - r_0| \quad (4.11)$$

Since we now have the basic Green's function, it is possible to determine Φ from the Green's function G . By combining Equations (4.9) and (4.10), integrating over the volume, V_0 , and applying Green's theorem, allows for the integral solution of the scalar potential resulting in Equation (4.12).

$$\Phi = \iint_{S_0} G(r|r_0) \frac{d\Phi(r_0)}{dn} - \Phi(r_0) \frac{dG(r|r_0)}{dn} dS_0 + \iiint_{V_0} G(r|r_0) F(r_0) dV_0 \quad (4.12)$$

Up until now the expressions have been adherent to the strict mathematical theory. It is possible to choose a setup with source function and boundary conditions to make simplifications. First, if the region of interest is chosen such that there are no internal sources, the second portion of Equation (4.12) becomes zero. In this condition the driven wave enters the region from one of the boundaries.

With on chip sonar, the acoustic sources all come from plane like locations, i.e. the transducers are on the silicon air interface, a flat plane. As such the bounding surface can be chosen as a flat plane bounded by an infinite semi-sphere. The top surface where the transducer generates waves is a reflecting surface, making it convenient to employ the method of images. The pattern from a single point in the enclosed region can be modeled as the sum effect from two points, one in the region of interest and the another modeling the reflected wave. Consider the setup shown in Figure 4.3.

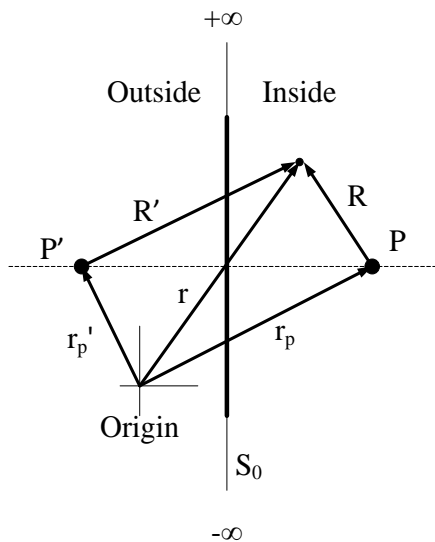


Figure 4.3: Point sources representing the method of images

If the field created by both of these point sources satisfies the boundary conditions than the boundary can be removed and the resulting field produced by the sources will be the same as the original boundary condition. There are two Green's function which represent this condition of the two sources, P and P', the sum and difference.

$$G_D(r) = \frac{1}{4\pi} \left(\frac{e^{-jkR}}{R} - \frac{e^{-jkR'}}{R'} \right) \quad (4.13)$$

$$G_N(r) = \frac{1}{4\pi} \left(\frac{e^{-jkR}}{R} + \frac{e^{-jkR'}}{R'} \right) \quad (4.14)$$

Where R and R' are denoted in Figure 4.3, and the subscripts D and N stand for Dirchelet and Neumann conditions. If the observation point lies on the boundary, then both these distance vectors, R and R' , are equal and $G_D(r)$ and $G_N(r)$ simplify to Equation (4.15) and Equation (4.16) respectively.

$$G_D(r)|_{S_0} = 0 \quad (4.15)$$

$$G_N(r)|_{S_0} = \frac{e^{-jkR}}{2\pi R} \quad (4.16)$$

Equation (4.12) also requires knowledge of the derivative of the two functions, solved in Equation (4.17) and (4.18).

$$\frac{dG_D(r)}{dn} \Big|_{S_0} = \frac{\cos(n, R)}{2\pi} \frac{d}{dR} \left(\frac{e^{-jkR}}{2\pi R} \right)_{S_0} \quad (4.17)$$

$$\left. \frac{dG_N(r)}{dn} \right|_{S_0} = 0 \quad (4.18)$$

These boundary conditions represent solutions which can be obtained if the normal component of either the pressure or the particle velocity is known at the boundary. Both of these values can be obtained from the KLM model. What is convenient about these two boundary conditions is that for either one either $G(r)$ is zero, or dG/dr is zero, which simplifies the expression in Equation (4.12), to two sets Equation (4.19) and Equation (4.20).

$$\Phi_D = \frac{1}{2\pi} \iint_{S_0} \Phi_0 \cos(n, R) \frac{e^{-jkR}}{R} \left[jk + \frac{1}{R} \right] dS_0 \quad (4.19)$$

$$\Phi_N = \frac{1}{2\pi} \iint_{S_0} \frac{e^{-jkR}}{R} \frac{d\Phi}{dn} dS_0 \quad (4.20)$$

Together these two expressions are known as the Rayleigh-Sommerfeld diffraction equations. The mean of the two expressions is also an appropriate solution to the wave equation, as seen in Equation (4.21)

$$\Phi_K = \frac{1}{4\pi} \iint_{S_0} \frac{e^{-jkR}}{R} \left[\frac{d\Phi}{dn} + \Phi_0 \cos(n, R) \left[jk + \frac{1}{R} \right] \right] dS_0 \quad (4.21)$$

Perpendicular to the transducer surface these three expressions converge to the same value. Off axis these each represent different boundary conditions outside of the transducer. Equation (4.19) is known as the Radiating Dipole and models the condition where the transducer is on an un baffled medium, where the acoustic impedance of the backing material is low, and there is zero stress at the surface. For

on-chip SONAR this is when the silicon is backed by air. Equation (4.20) often referred to as Huygen's Equation, models a rigid infinite baffle, such that the acoustic impedance of the backing material is very high and there is zero particle displacement at the surface. For on chip SONAR this requires a material much stiffer than silicon in intimate contact with the top surface of silicon. The final expression, Equation (4.21) is known as Kirchoff's function is when the remaining boundary has an acoustic impedance identical to that of silicon. This condition exists in the case of an on-chip SONAR for a multi-chip stack, or the use of absorbing backing layers.

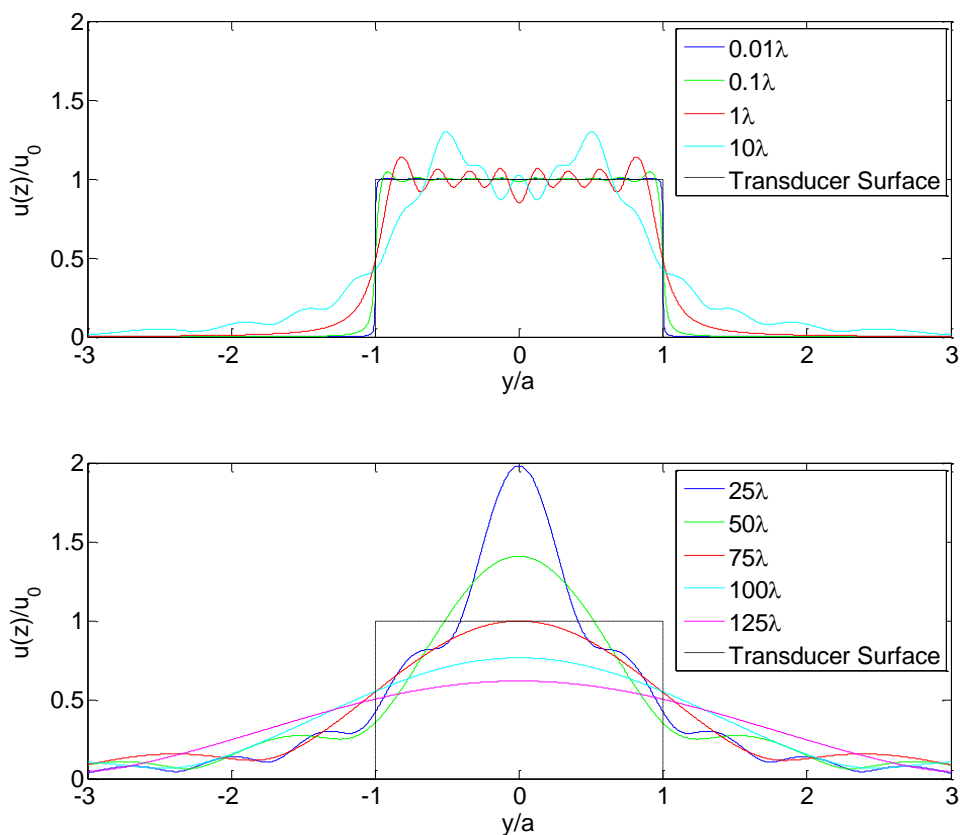


Figure 4.4: Plots of radiation pattern at different distances from the transducer

The first thing to investigate is the shape of the pattern which emerges from the transducer. Due to the simplicity of mathematical analysis a circular transducer is

often used in these types of analysis as it has a closed form solution. Here numerical solutions are presented to demonstrate the effect of the wave travelling from the transducer. Consider the radiating dipole case as its application to the on-chip SONAR applications. To help limit the design space all dimensions are normalized to wavelength. These first set of plots are for a circular transducer with a radius of 5λ . The pattern at different distances from such a transducer is plotted in Figure 4.4.

Consider the first portion of Figure 4.4, near the transducer itself, most of the wave is contained within the spatial area of the transducer. At some point the particle displacement amplitude interferes and actually doubles in size at the peak displacement over a narrower area, this location is referred to as the “self-focal” point of the transducer. After this the wave front decreases in amplitude and spreads out over a larger spatial area. Where this occurs and the rate at which it occurs can be determined from investigating the peak response on the center axis of the transducer. This is done for several different geometries and plotted in Figure 4.5.

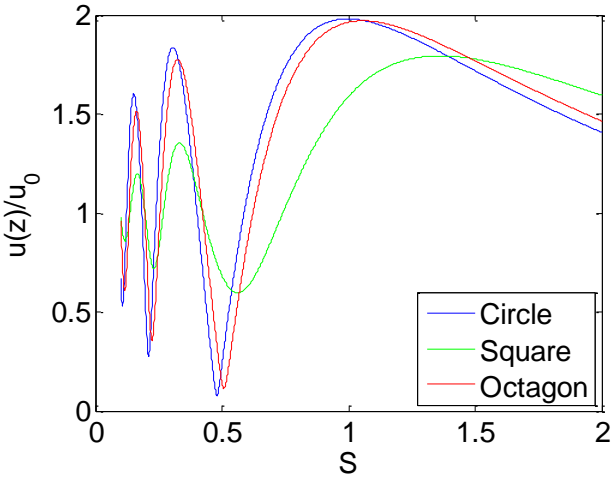


Figure 4.5: Plot of on axis value of intensity from radiation pattern of a circle

These are now plotted against a new parameter S , known as the Fresnel Parameter

$$S = \frac{z\lambda}{a^2} \quad (4.22)$$

The purpose of this is to normalize the axial distance with respect to the transducers area. A larger transducer will contain energy within its area over a longer distance. As evident in Figure 4.5 distances less than $S = 1$, there is significant variation in the amplitude across the transducer area. From Figure 4.4 these variations mostly average out across the area. At values of S greater than 1 the amplitude decreases as $1/r^2$. The Fresnel parameter is useful in separating these two regions as $S < 1$ is known as the near field and $S > 1$ is known as the far field.

Strictly speaking S is defined for a circular transducer. Consider as well other geometries which are more easily realized in lithography; square and octagon transducers, also plotted in Figure 4.5. The square transducer plotted here has each side equal to twice the radius of the transducer, as such the effective area is greater so it peaks a little further from the transducer. Though the peak value is less than that for the circular transducer, it has greater amplitude over the space of the far field. Similarly an octagon transducer, while closer in area to the circle is slightly greater in area leading to a slight shift in the peak value and greater amplitude in the far field region.

Returning to the communication channel, for a single transducer pair on axis, of identical size the spacing should be less than the switch to the far field. The loss associated with diffraction effects can be determined as the ratio of power on the receiver to power on the transmitter as seen in Equation (4.23).

$$DL(z) = \frac{\int_{R_x} T(x, y, z)T^*(x, y, z)dxdy}{\int_{T_x} T(x, y, 0)T^*(x, y, 0)dxdy} \quad (4.23)$$

Where T is the stress field determined from Equation (4.21). This is plotted in dB (10 log) for a square transducer with a side length of 10λ .

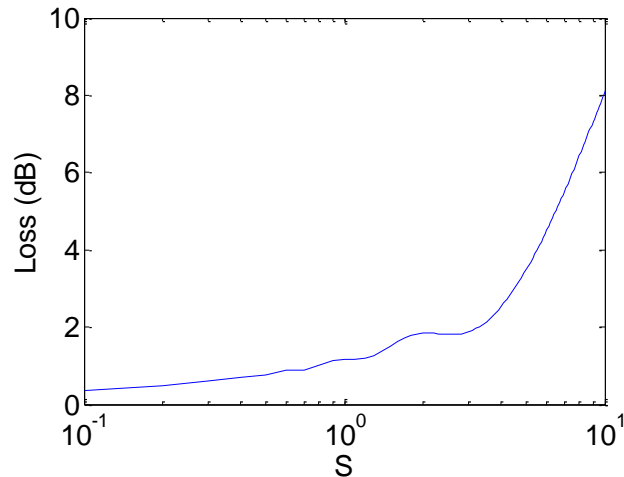


Figure 4.6: Diffraction loss as a function of distance S

This shows the design space and the loss in the one dimensional channel associated with diffraction. This however limits the type of communication channels to an on axis 1-D channels. A couple of issues distinguish the design of a phased array compared to a single element communication channel described above. Firstly individual transducer elements in the array should be operated in the far field such that pressure from the multiple sources can interfere with each other to create a steerable pattern. While the single elements will operate in a region which is theoretically high loss, the entire array can be operated such that the overall size of the array operates in a lower diffraction loss region. The design of a whole array will be covered in the next section. For now it is important to further investigate the off-axis pressure profile of a single transducer.

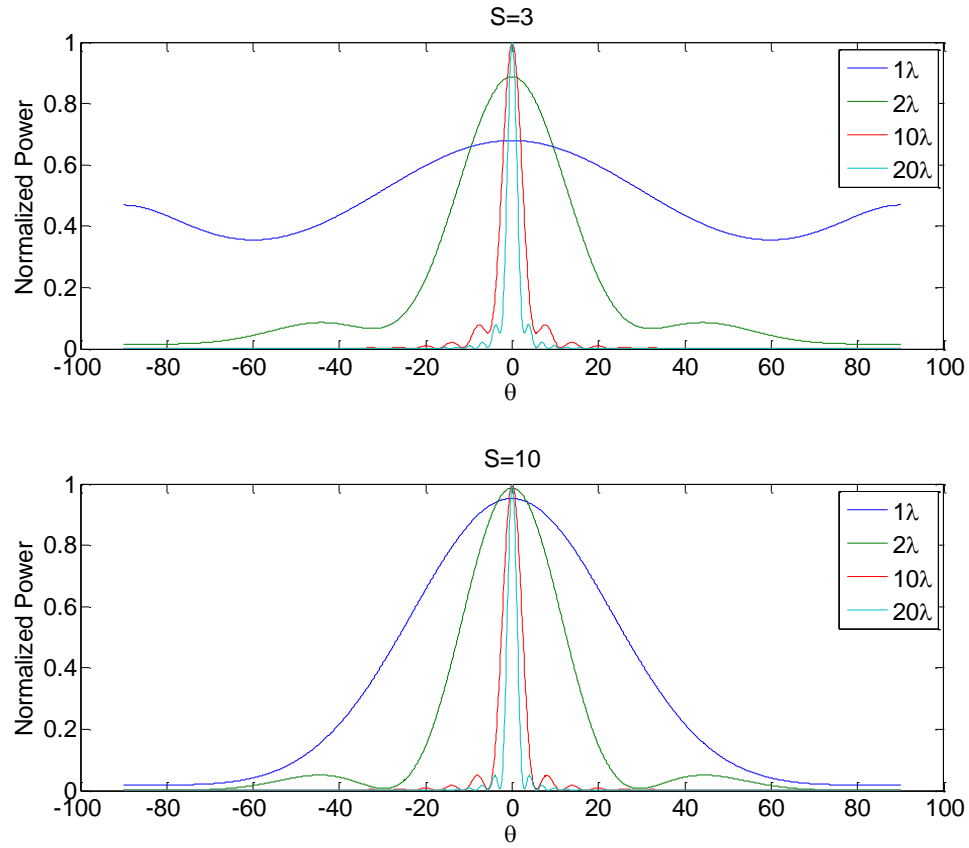


Figure 4.7: Radiation pattern of a transducer (or multiple transducers)

The Fresnel parameter is more accurate for transducers of larger size. As such in Figure 4.7 at a value of $S = 3$ the single wavelength transducer appears to have an relatively equal response at all angles. However further from the transducer at $S=10$ the shape is more narrow. The larger transducers however all maintain the same shape, with respect to angle from the center of the transducer. This is significant as it will limit the maximum angle that can be steered by the phased array. This angle can be found analytically for circular transducers, and in a pressure release baffle an infinitesimal ($\ll \lambda$) transducer has an angular response with 3-dB points at 45 degrees [69].

4.3 Array Factor

By the principle of superposition, the acoustic radiation pattern from an array of elements can be determined by the sum of individual elements radiation patterns. This can be simplified by considering the radiation pattern from a single element and the radiation pattern from an array of isotropic elements separately. Here we start by considering a 1-D array and the 2-D pattern it creates. In order to determine the pattern caused by a 2-D array it is just the projection of each axis into two 1-D arrays.

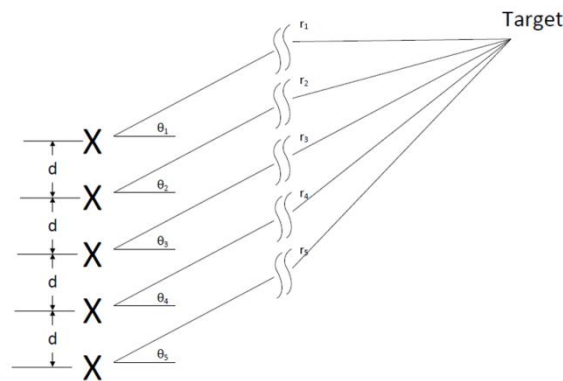


Figure 4.8: Phased array system setup, the effect of the array at the target point is determined by superposition of the elements in the array

Let's consider an N element array of isotropic point source elements, as illustrated in Figure 4.8 (where $N = 5$). Each element is located at an X and they are spaced d apart. The goal is to find the combined pattern of all elements at some target point a distance from the array. If each element radiates sinusoidal acoustic waves then at some distance r , the particle velocity is described as in Equation (4.24), (with time dependence suppressed), recalling that the relationship between particle velocity and the scalar wave potential is linear in the far field.

$$v(r) = \frac{Ae^{-jkr+\beta}}{r} \quad (4.24)$$

Where A is the initial amplitude, k is the wavenumber, r is the spherical distance from the element, and β is the initial phase of the signal. If the distance R , from the center of the array to the target point, is large one can assume that rays from each element to the target are all parallel. Put another way the angle θ measured from the normal of the array for each element in the array is the same.

$$\theta_1 \approx \theta_2 \approx \dots \approx \theta_m \approx \theta \quad (4.25)$$

Therefore the difference in the path length r , from each element to the target increases linearly with each element. The change between two successive elements can be determined through trigonometry as Equation (4.26).

$$\Delta r = d \cdot \cos(\theta) \quad (4.26)$$

Taking into account the position of an element in the array, the element's effect on the target point can be calculated as in Equation

$$P(R) = \frac{Ae^{-jkR}e^{n \cdot k \cdot d \cdot \cos(\theta) + \beta}}{R} \quad (4.27)$$

While the distance can be simplified to the array distance R for the spatial quantity of $1/R$ due to the small change in distance from (4.26) it does still need to be accounted for in the phase. Since it is possible to drive each element independently, for the sake of simplicity consider each element to be driven by a sinusoid with a

linear phase shift between each successive element. By summing up N isotropic elements in a linear array with field contribution from (4.27) and taking the reference point at the center of the array then, one can calculate the array factor AF [80].

$$AF = \frac{\sin\left(\frac{N}{2}\Psi\right)}{\sin\left(\frac{\Psi}{2}\right)} \quad (4.28)$$

$$\Psi = k \cdot d \cdot \sin(\theta) + \beta \quad (4.29)$$

It is also possible to steer the beam changing only the phase between each element. A linear phasing scheme is chosen for its simplicity, such that the successive phase change between two elements is a constant which is represented by β in Equation (4.29). The maximum value in Equation (4.28), occurs when Ψ is equal to 0. Therefore the relationship between β and θ is

$$\beta = -k \cdot d \cdot \sin(\theta) \quad (4.30)$$

Using this array factor it is possible to investigate the effects of spacing and number of elements on the far field pattern. For simplicity of illustration, consider first the condition where β is 0, and the beam is formed broadside, at 90 degrees to the linear array. Consider first the inter element spacing. A summary of different spacing values is shown in Figure 4.9.

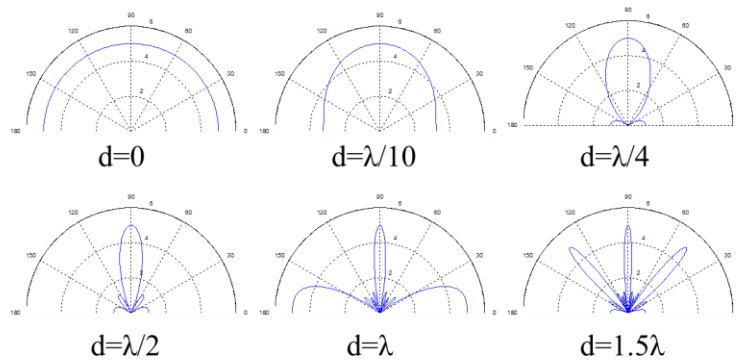


Figure 4.9: Array factors for $N = 5$ elements, varying spacing between elements

The patterns plotted in Figure 4.9 are normalized to a single element radiation pattern for illustrative purposes. The first case, where the electrode spacing is zero, implies that all the elements are directly on top of each other, adding in phase the same pattern, which is an isotropic pattern 5 times greater in amplitude than an individual element. As the spacing increases a single large lobe or beam emerges. As the spacing continues to increase, smaller side lobes emerge. Referring to the $\lambda/2$ spacing, there are 4 small lobes associated with the one large lobe. The large lobe is called the primary beam and the smaller lobes are called side lobes. When the spacing is greater than $\lambda/2$ additional large lobes appear; called grating lobes. The initial derivation involves adding the elements in phase at a single point. If the spacing is greater than a wavelength then the first cycle of one element can add with the second cycle of its neighbor causing another location where there is a large lobe. These grating lobes can be reduced by ensuring the half wavelength spacing, using a pulsed mode of operation (less cycles means the higher order grating lobes will diminish in amplitude), or by using directional elements which attenuate in the region of the grating lobes, but this will reduce the scanning range. Furthermore, since grating lobes are indistinguishable from the main lobe in continuous wave operation, the maximum scanning that can

occur with the main lobe, is between two grating lobes. So taking the half wavelength spacing as the optimal spacing choice then the effect of the number of elements on the radiation pattern is calculated in Figure 4.10 using Equations (4.28) and (4.29), with β equal to zero.

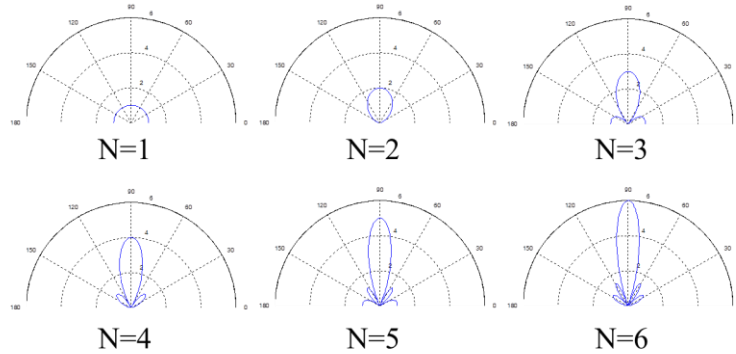


Figure 4.10: Array factors for $\lambda/2$ spacing, varying the number of elements in the array

Again all patterns shown are normalized to a single isotropic emitter for illustrative purposes. The $N=1$ case represents a single isotropic element, and the pattern is simply spherical. As the number of elements increases, directionality of the beam is apparent. The increased number of elements also brings about additional small lobes, called side lobes. These are different than grating lobes and are present even in a simple planar transducer. The first side lobe is approximately -13 dB lower than the main lobe, whereas the second is -18 dB and they continue to shrink at higher node number [69]. As the number of elements increases the magnitude of the first side lobe does not change but it does get thinner as does the main lobe. By operating the transducers in a pulsed mode of operation, using a tone burst or a Gaussian envelope, can reduce the presence of side lobes and nulls without distorting the main lobe.

Sidelobes are a result of off axis phase variations between elements, when the array is operated at continuous wave. When the transducer is pulsed there are less cycles of signal to add up at these angles while still summing at the main lobe. [81]. Nulls themselves are also interesting as they can be used to cancel out an interfering signal. If an undesired signal is incident on the array at the angle of the null then the signal will be attenuated rather than amplified.

So far the discussion has been qualitative on the beam pattern due to number of elements and the spacing. First consider the main beam. The goal is to have the beam as small as possible so as to concentrate the signal to a single point with high selectivity. The width of the main lobe can be determined by solving Equation (4.28) for the half power point. This has been approximated in [80] as

$$\Theta_H \approx 2 \cdot \sin^{-1}\left(\frac{1.391\lambda}{\pi Nd}\right) \quad (4.31)$$

There are three properties which can be adjusted to improve the beam-width. As the frequency increases, the wavelength decreases which lowers the beam-width. Increasing the number of elements inversely reduces the beam width. Finally increasing the spacing between elements decreases the beam width. The last approach however is unadvisable due to the generation of grating lobes.

So far the derivation for the array properties has assumed continuous mode operation of a single frequency. In order to use the array as a communication channel, a signal will be modulated on top of the carrier, consisting of some bandwidth. It is therefore important to know how much bandwidth the array can carry and what happens to the signals if it moves outside of the useable array bandwidth.

Returning to Figure 4.8, at some target time t , there are subsequent time delays of approximately $\Delta r/V_a$ between each element. Using this value at a frequency f_l yields a

phase shift β_1 between each element. A second frequency f_2 , would require a different phase shift β_2 . If f_2 is greater than f_1 , then the phase shift β_2 must be greater than β_1 because of Equation (4.30), in order to point to the same target point. If instead the phase shift remains constant, then the signal at f_2 will shift towards the broadside, center location $\theta + \Delta\theta$. Likewise if f_2 is less than f_1 and the phase remains constant it will shift away from the broadside. This angle shift has been characterized in [83] as Equation (4.32)

$$\Delta\theta = \frac{\Delta f}{f} \tan(\theta) \quad (4.32)$$

As long as the shift in θ is less than the beam width of the primary frequency then the signal will still reach its intended goal. A criterion commonly used is such that $\Delta\theta$ is less than one fourth the total beam width[83].

$$\frac{\Delta\theta}{\Theta_H} < \frac{1}{4} \quad (4.33)$$

This results in an expression for the bandwidth of the array in Equation

$$\Delta f = \frac{f \cos^{-1}\left(\frac{1.391\lambda}{\pi Nd}\right)}{4 \tan(\theta)} \quad (4.34)$$

While it is expected, by definition that a smaller beam width results in a smaller bandwidth and a greater carrier frequency results in a greater bandwidth, it is interesting that the bandwidth has a dependence on the angle θ of which the beam is pointed. This means that the further the beam is pointed from the broadside condition the smaller the bandwidth of the array.

Chapter 5

DEMONSTRATION OF AN ULTRASONIC ON CHIP 120 MBIT/S COMMUNICATION LINK USING INTEGRATED PIEZOELECTRIC PHASED ARRAY

5.1 *Introduction*

With any technology competing as a communication modality on chip there are three criteria to consider; (1) reduced chip area of the communication channel, (2) higher communication bandwidth and (3) reduced energy per bit. Optimizing all three criteria is a challenging problem as there are competing trade-offs when optimizing between these figures of merit. It is worth noting that in many computing systems latency between transmit and receive signal also needs to be minimized, as it is directly related to the communication bandwidth. This is a limit with traditional CMOS wire interconnects today. With an ultrasonic communication link, delay/latency and bandwidth are not the same thing. From a system architecture point of view, the overall system will need to be designed to minimize the effects of latency by relying on high volumes of data transmission.

Both bandwidth and chip area are strongly related in modern CMOS systems as well as for ultrasonic interconnects. New technology nodes for CMOS are defined by the minimum dimension of the transistor. Each new advanced technology node brings about a reduction in size and an increase in frequency. For on-chip optical communications, the bandwidth can be considered as practically infinite [3] owing to the ~100THz carrier frequency of the electromagnetic waves, but one of the big challenges in adapting on-chip optical interconnect system is the size of optical components, such as the laser or that there is a lack of an optical switch which can

compete with the transistor [24]-[26]. As will be seen in this chapter, with respect to ultrasonic communication link, as the communication carrier frequency increases, the transducer dimensions decreases owing to reduction in the wavelength. With carrier frequencies in the few GHz range, the wavelength in silicon is a few microns.

To make a fair comparison of energy per bit, between the different communication modalities, one requires knowledge of what is competitive today as well as what is projected for future systems. The energy per bit is equivalent to the power per bandwidth of communication. Consider a single inverter pair: for an advanced CMOS technology nodes a single inverter can drive another gate with ~ 10 fJ/bit [84]. Typically though, there are multiple digital blocks besides a single inverter involved in moving data from one point to another so the power increases quickly. The limit in system power consumption is due to the ability to remove heat from the chip, this has peaked in the range of 200 Watts [24]. For lower technology nodes, 22 nm and below, with large system complexity, consisting of multiple cores, the communication energy budget would be constrained such that even 300 fJ/bit would consume the entire power budget. Therefore technologies which present link budgets on the order of 20-200 fJ/bit or lower are of great importance [24]. Using low voltage signaling techniques for communication on chip has had success in getting both interchip and intrachip communication down to ~ 50 fJ/bit [85].

Chip-to-chip optical communication has been shown to be as low as 100 fJ/bit [86]. Though the optical waveguide links are very low loss there are several sources of loss associated with converting from electrical signal to optical and back to electrical. These losses are (1) quantum efficiency of the laser (2) quantum efficiency of the detector (3) coupling efficiency of the laser to waveguide and (4) coupling efficiency of the waveguide to the detector. The laser power can then be reduced to the point

such that the final power detected by the receiver is above the noise floor. This power over the bandwidth is the energy per bit associated with the optic channel.

5.2 Ultrasonic Communication Link Budget

The three figures of merit (Area, Bandwidth and Energy per bit) are determined by the minimum signal levels that can be detected, for a given ultrasonic transmit transducer energy. The minimum detectable signal level is a result of the noise associated with the receive transducer and receiver electronics. First let's consider only the transducer and its interfacing impedances as the source of noise. The transducer noise comes from Equation (3.44) and the load impedance also contributes thermal noise from Equation (3.41). Together the total noise power at the receiver output is expressed in

$$P_n = \int \frac{|G_r(f)|^2 4k_B T Z_{2A}}{R_L} df + 4k_B T (BW) \quad (5.1)$$

Both of the terms in Equation (5.1) are a function of the bandwidth of the transducer. For greater bandwidths, greater signal power is needed since the noise power increases. Also worthy of note is that the acoustic impedance and load resistance are a function of the transducer area. The signal power at the receiver is a function of both the input power and the channel loss mechanisms. Therefore the signal to noise ratio, as a function of input power can be determined from Equation (5.2)

$$SNR = \frac{P_{in} \cdot DL \cdot CL \cdot IL}{P_n} \quad (5.2)$$

Where the three mechanisms by which signal is lost in the ultrasonic communication channel are; (1) DL: Diffraction loss, (2) CL: Conversion loss, and (3)

IL: intrinsic material loss. Diffraction loss is the loss associated with the spreading of signal energy as it propagates from a finite emitting source. Conversion loss is associated with the conversion of signals from the electric domain to the acoustic domain, then back to the electric domain. This includes loss as a result of load and source impedances interfacing with the channel. Intrinsic material loss is the viscoelastic or internal frictional losses which convert ultrasonic wave intensity to phonons or heat.

As previously established, by operating the transducer in the near field of operation the loss associated with diffraction is nearly independent of distance. The Fresnel parameter from Equation (4.22) (reproduced here) is what distinguishes the regions of operation.

$$S = \frac{z\lambda}{a^2}$$

In order to design the transducer area, consider a channel length of maximum dimension z_0 . In this case the parameter a can be determined by Equation (5.3).

$$a = \sqrt{\frac{z_0\lambda}{S}} \quad (5.3)$$

Strictly speaking this parameter is for circular transducers with radius a , however it is a fair approximation for a square transducer of side $2a$. In either case the area is a function of the wavelength λ . Therefore as the frequency of the transducer scales up the area required for minimal loss scales down. The diffraction loss can be calculated from Equation (4.23), reproduced here for convenience.

$$DL(z) = \frac{\int_{R_x} T(x, y, z)T^*(x, y, z)dxdy}{\int_{T_x} T(x, y, 0)T^*(x, y, 0)dxdy}$$

Since the designed area is changing with frequency to meet the Fresnel condition then the diffraction loss itself does not scale with the frequency of the transducer. Numerically solving Equation (4.23), using the appropriate z_0 for a 1.3 mm channel in silicon, yields a diffraction loss of 1.18 dB.

Intuitively and as established before the best case scenario for conversion is when the transducer and medium are matched. Though this is an ideal condition it is approachable with the design of the appropriate matching layers. Additionally, circuit matching design techniques cannot be used as they are not practical for on-chip sonar applications, due to the inability to design very small inductors. Consider the channel setup shown in Figure 5.1.

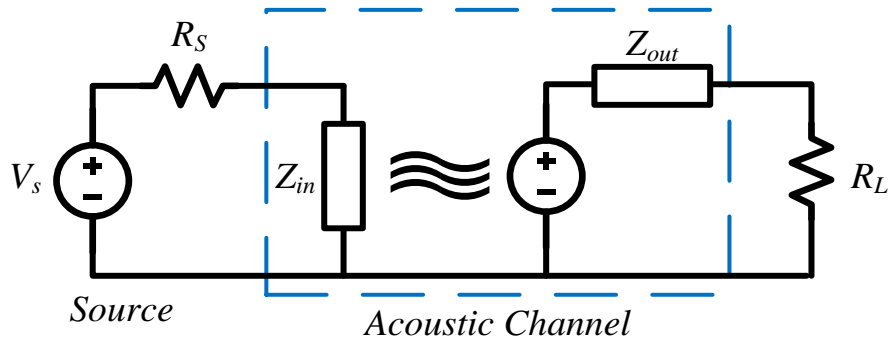


Figure 5.1: Conversion loss figure

There are two impedances connected to the channel, the source R_S and the load R_L . If we have complete access to the design of the source resistance, then for maximum power, since this is a lumped model with no concerns of RF matching, then R_S should be as close to zero as possible. At the load however the output impedance of the

transducer is fixed by the center frequency and area of the piezoelectric transducer. By maximum power theory the maximum power transfer occurs when the load impedance is matched to the transducer impedance. If the load impedance is chosen to be the optimal value such that it scales with the center frequency of the transducer, then the peak value of the conversion loss does not scale with transducer center frequency.

Furthermore, looking at the transmit transducer impedance, as previously established all parameters are a function of the clamped capacitance. The resonance frequency and central response of the transducer are determined by the thickness of the transducer. Considering a simple square transducer size than the capacitance is expressed in Equation (5.4)

$$C_0 = \frac{\epsilon_r \epsilon_0 (2a)^2}{d} \quad (5.4)$$

As established from Equation (5.3), the area scales with wavelength. Since the thickness of the transducer d also scales with wavelength then for a given channel length the clamped capacitance is independent of resonance frequency. Though the capacitance may be fixed, the impedance ($1/j\omega C_0$) however scales down with center frequency, necessitating a reduction in the load resistance.

By considering aluminum nitride transducers of k_t^2 values of 7%, completely matched to the silicon, the conversion loss solved numerically yields a power loss of 24.15 dB. It is the greatest source of loss for the channel. From this model it is also possible to determine the 3-dB frequency for the transducers, 53.88% of the center frequency.

The final source of loss is the intrinsic material loss of the mechanical layers that the waves propagate through. As reported earlier this attenuation coefficient for silicon is very low, on the order of 10^{-17} dB/Hz². This can become significant at very high

frequencies. For instance at 10 GHz it becomes 5.2 dB for a 1300 μm channel, as opposed to 0.052 dB at 1 GHz.

Given all of the losses, and the noise power it is possible to calculate a bit error rate for the channel as a function of the input power to the channel. This expression is seen in Equation (5.5).

$$BER = \frac{1}{2} \text{erfc}(\sqrt{SNR}) \quad (5.5)$$

Channels of different center frequencies can be characterized such that their BER is determined by the input power to the channel.

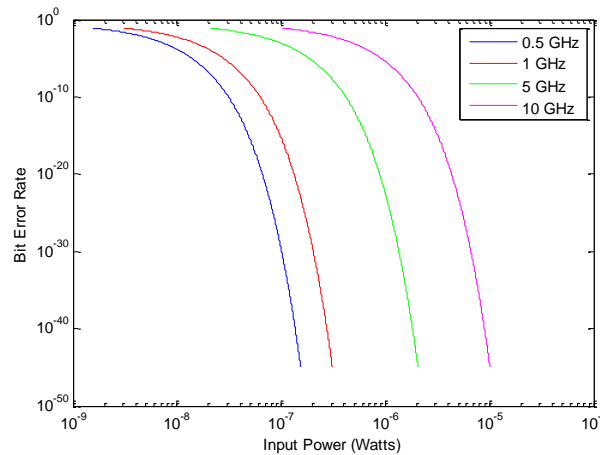


Figure 5.2: BER plot

Consider a device that is running continuously for 2 years at maximum bit rate, for a 10 GHz carrier the BER needs to be less than 2.95×10^{-18} . From Figure 5.2, this corresponds to a signal power of 3.768 μWatts , which is an energy per bit of 0.7 fJ/bit. While this result is promising, it does not consider the power associated with the supporting electronics, which will be covered in the next chapter. For sake of comparison this is the equivalent of neglecting the supporting circuitry for optical

interconnects, such as the detector, tuning or modulation, which has a result on the order of 20 fJ/bit [86].

5.3 Transducers

Experimental results were obtained using aluminum nitride transducers, fabricated at SANDIA National Laboratories [76] with multiple pixel sizes and pixel pitch.

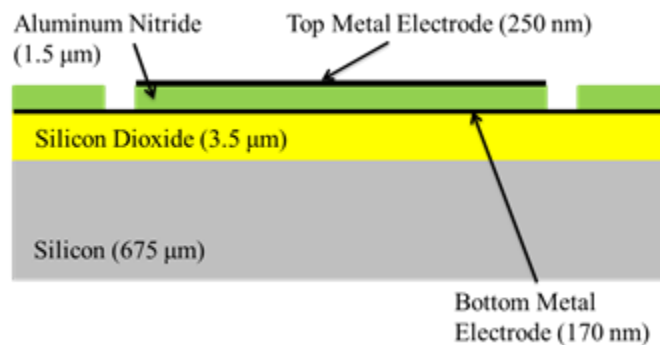


Figure 5.3: Transducer Cross section

The cross section for this process and layer thicknesses is illustrated in Figure 5.3. The process starts with a 6", 675 μm thick silicon wafer. Silicon dioxide is deposited with a PECVD process. Next a polysilicon sacrificial layer is added and then another layer of silicon dioxide is deposited on top. The sacrificial polysilicon (not shown in Fig. 2 for simplicity) is an optional layer for the purpose of release, and was not utilized for the pixels used in these experiments. Next, a metal bottom electrode (170nm) is sputtered on top of the oxide base, patterned and etched. This is then followed by sputtering, patterning and etching of AlN (1.5 μm), to define the transducers. Finally another metal (250 nm) is sputtered on the top and patterned to create the top electrodes of the transducers. An optical picture of an array of these transducers can be seen in Figure 5.4. This structure is a rectangular matrix of pixels.

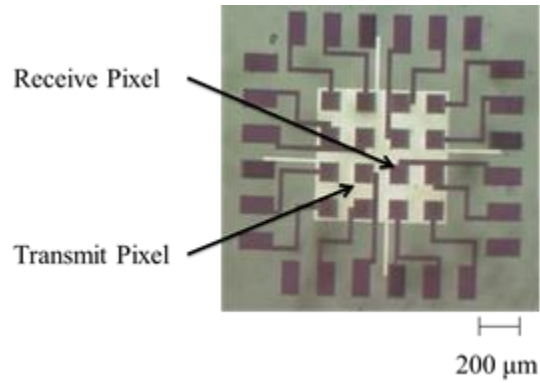


Figure 5.4: Optical image of the AlN transducer array

5.4 Single Transducer Pair Communication Channel

The first experiment for a communication channel consists of a simple transmit receive pair of transducers. This is done to verify acoustic energy coupling into the silicon and reception of the signal at detectable levels.

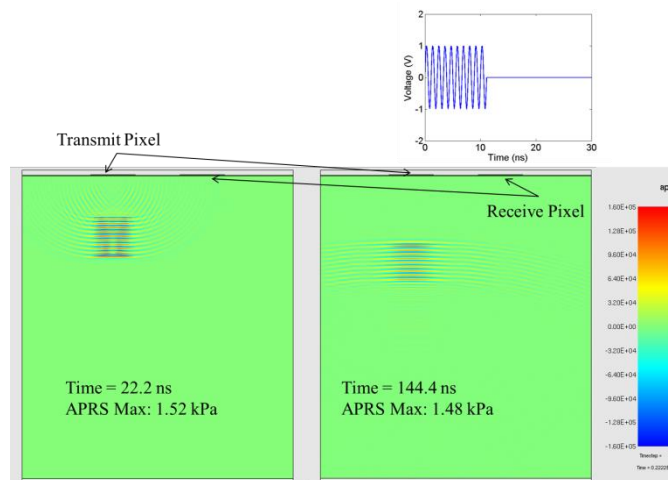


Figure 5.5: PZFlex FEA Sims

FEA simulations are used to simulate communication from one pixel to the nearest neighbor. For $\langle 100 \rangle$ silicon, the elastic modulus in the z-direction (or into the plane of

the silicon wafer) is 165.7 GPa [87], and with a density of 2330 kg/m³ the speed of sound in silicon for a wave travelling as previously described is 8433 m/s. The silicon wafer used for the deposition of AlN, is a double-polished 675 μm thick 6-inch wafer. Therefore the expected return time of the pulse is 160 ns.

In order to model using silicon as a communication channel the FEA software PZFlex was utilized to simulate the propagation of an acoustic wave into silicon and its effects on the neighboring pixel. PZFlex is a FEA designed specifically for time domain simulations of acoustic wave propagation and interactions with piezoelectric materials. The transmit pixel is a 100-μm square of AlN on top of a thin silicon dioxide layer on top of silicon. The neighboring pixel is the same dimension with a center to center spacing, from the transmit pixel, of 200 μm. The results of the simulation are seen in Figure 5.5. Ten cycles of a 900 MHz sinusoidal pulse, with 1- V_{peak} amplitude, is applied to the left pixel inducing a pressure wave in the silicon. In addition to the P-Wave, the discontinuity of the AlN layer on the edges also launches waves into the solid. The amplitude of these waves is much lower. As the primary wave travels it reflects off the back surface and returns to the top. The stress wave induces a voltage on the neighboring pixel, with an amplitude of 250 μV, 160.0 ns after the pulse is applied. This suggests that the signal will be viewable on an oscilloscope, with typical noise levels of 100 micro-volts in the GHz frequency range.

When the pulse is applied, a large RF feed-through signal is seen on the receive side. This is due to electromagnetic waves traveling across the air and the silicon gap, and capacitive coupling, between the transmit and receive pixels.

For pulsed mode operation, the transmit pixels need to be driven by multiple cycles of a sinusoid. RF switches with 4 nanosecond settling time (Analog Devices, ADG901, -3dB bandwidth of 4.5GHz) were used to gate a continuous sine wave RF signal to achieve 18 cycles at 900 MHz at output voltage of 0.5 V_{pp} .

On the receive side two commercial RF amplifiers (MiniCircuits ZX60-33LN-S+) with a gain of 18.8 dB are cascaded in order to boost the return signal to levels that can be more easily read on an oscilloscope (Agilent Infiniium 54835A). The AIN array is placed on spacers on a probe station, and GSG probes are used to apply the voltage signal and to pick up the receive signal on the neighboring pixel.

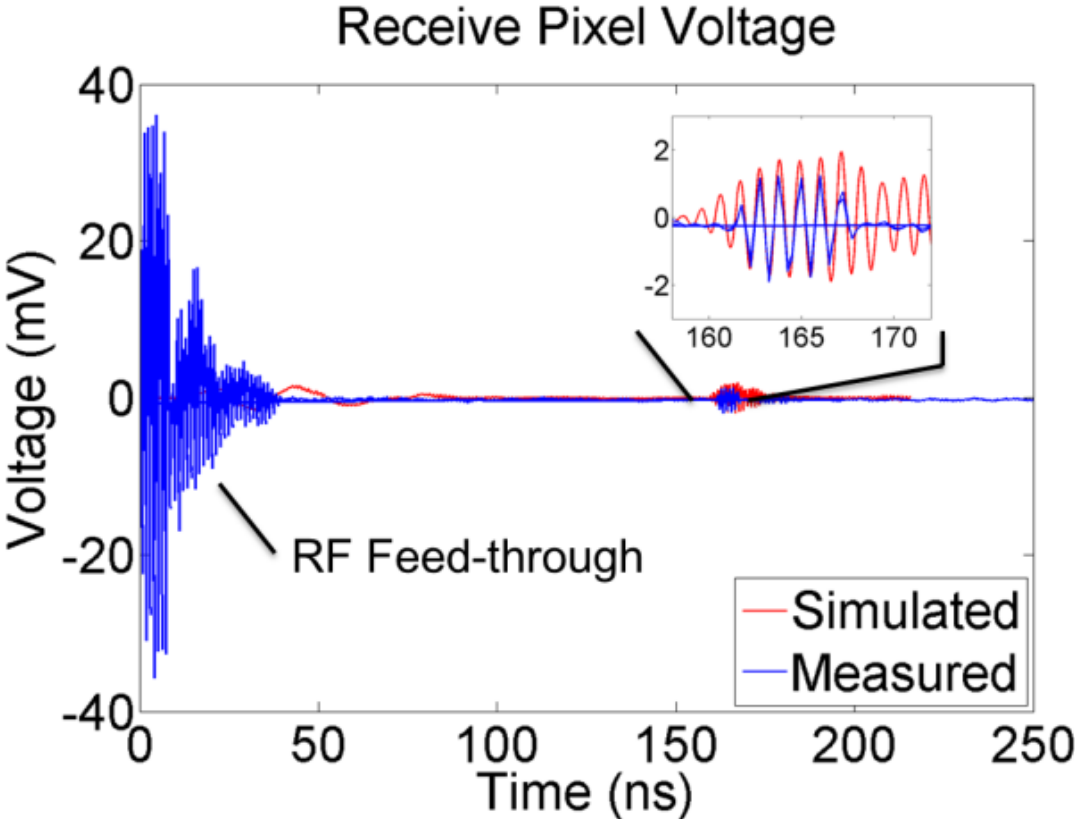


Figure 5.6: Pulse Echo measurements, comparison with simulation

At 900 MHz carrier frequency, the return pulse is measured and compared to the simulated value. The time of flight measurements matches the expected calculated and simulated time of 160 ns. The possibility of this being related to RF transmission line effects is ruled out since the time scale would suggest cabling on the order 50 meters

as opposed to the approximately meter length cables used in these experiments. The measured data shows a large RF feed-through while the pulse is applied. Due to attenuation in the RF switches the transmit amplitude is only on the order of 0.5 V peak to peak. The same input pulse, applied to the transducer is measured and imported into PZFlex and used as a stimulus to verify the model. Changing the amplitude and the width of the input pulse resulted in corresponding changes in the return pulse. This can further be used to demonstrate a communication channel by showing input and output pulses of the channel as shown in Figure 5.7.

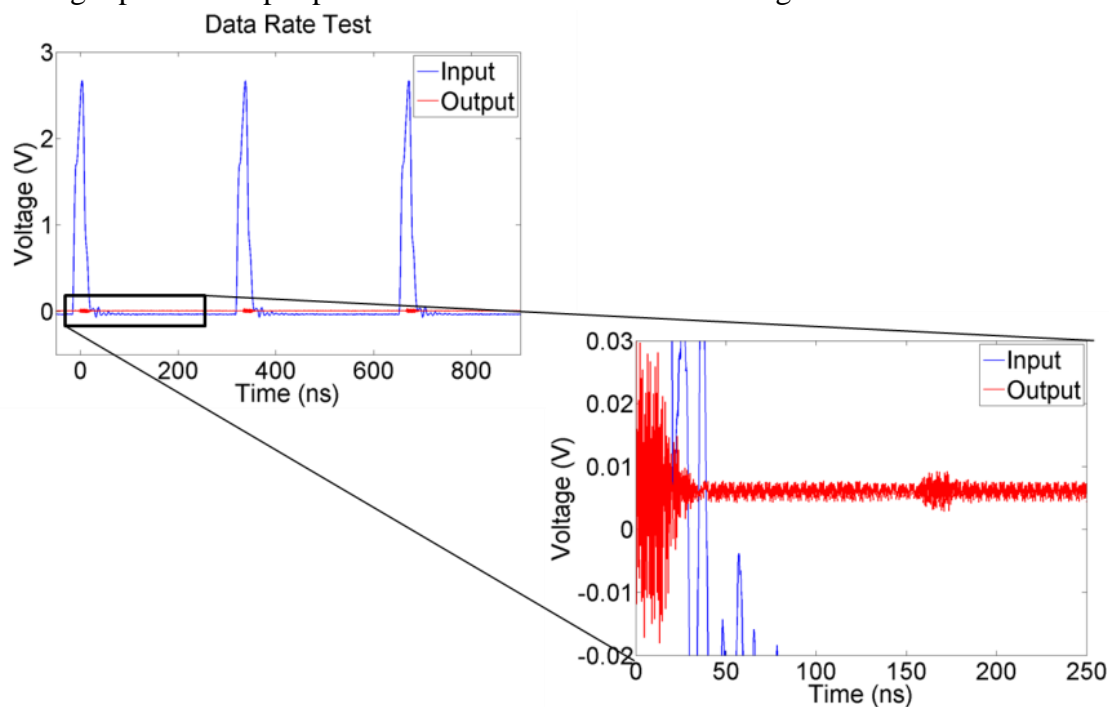


Figure 5.7: Single transducer pair communication channel demonstrating 7 Mb/s. The red-channel is the receive voltage, and the blue channel is the input bit stream to the RF switch

To verify the modelling put forth with the KLM and diffraction loss sections a transmit receive frequency sweep is done. This measures the amplitude of the return

pulse of a neighboring pixel. All the input and output impedance paths of the PCB and cabling are measured beforehand using an S-paramter network analyzer, as well as including the 50-ohm source and scope load impedances. The transmit pixel is a square transducer $43\ \mu\text{m}$ by $43\ \mu\text{m}$. The receive pixel has identical dimensions and is located $100\ \mu\text{m}$ away center-to-center. This defines the integration limits of the diffraction loss integral in Equation (4.23). The measurement result and complete model are plotted in Figure 5.8. The second peak is likely associated with the LC resonance formed by the wire-bond and the clamped capacitance of the transducer. The clamped capacitance is roughly $200\ \text{fF}$, and the wire-bond has an inductance on the order of $1\ \text{nH/mm}$, and the bonds are roughly $1\ \text{cm}$ long, leading to a resonance at the order of $3.5\ \text{GHz}$.

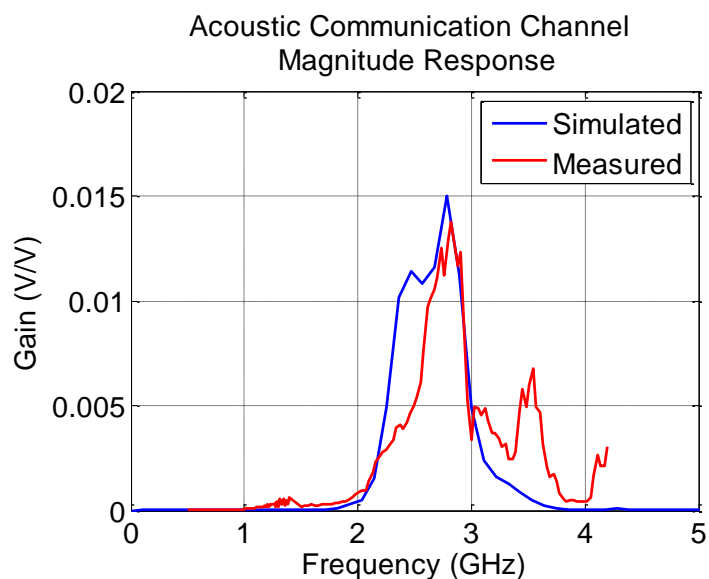


Figure 5.8: Communication channel frequency response – calculated response compared to measured response.

5.5 Phased Array Communication Channel

The next step involved using an array of these aluminum nitride transducers to form a controllable beam for reconfigurable communication. Each array is composed of 16 square elements, $43\ \mu\text{m}$ on a side, spaced $100\ \mu\text{m}$ from center to center. The inner four elements were driven with sinusoids of the same frequency but different phase. The phases were chosen such that there was a linear change in phase of $d\phi_1$ along one axis and $d\phi_2$ along the other axis. This allows for full 3-D control of beam direction. The signal was measured at the 4 corner elements of the array, with a high speed oscilloscope (Agilent Infiniium 13-GHz). This corresponds to a physical angle of 8 degrees. This setup is shown in Figure 5.9.

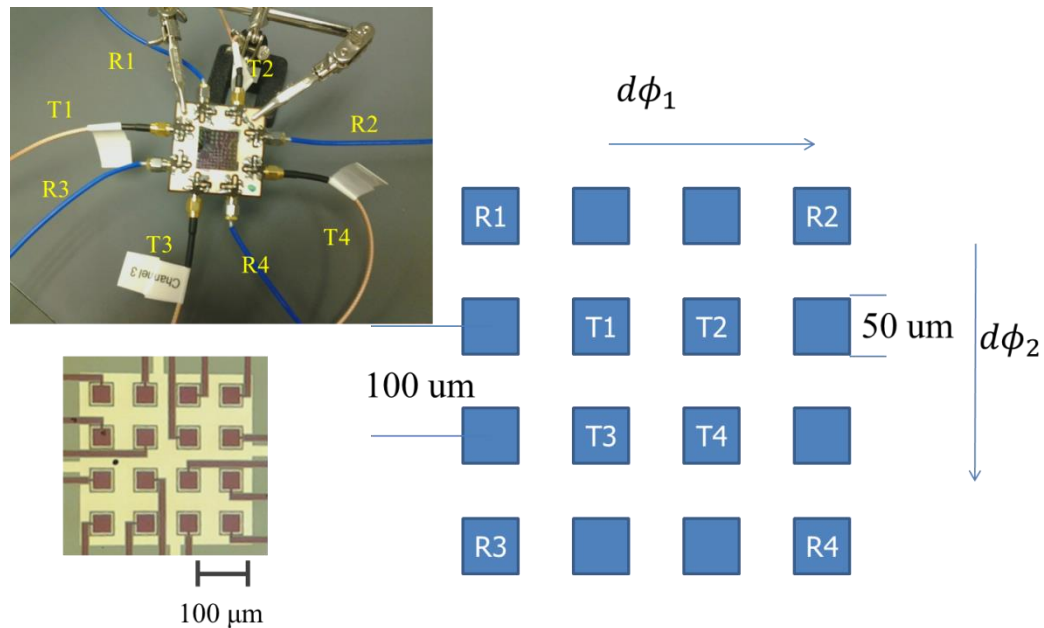


Figure 5.9: SONAR Die and PCB

Each transmit channel is generated using a phasing system built with off-the-shelf commercial components and assembled on a printed circuit board. The pixel array is driven by an RF function generator gated by a RF switch driven by a pulse generator. Each channel has a variable phase shift block and a variable gain amplifier to independently control the amplitude and phase as seen in Figure 5.10. All channels are driven with the same pulse in order to window the transmit pulse to distinguish between the RF feed-through and acoustic signals.

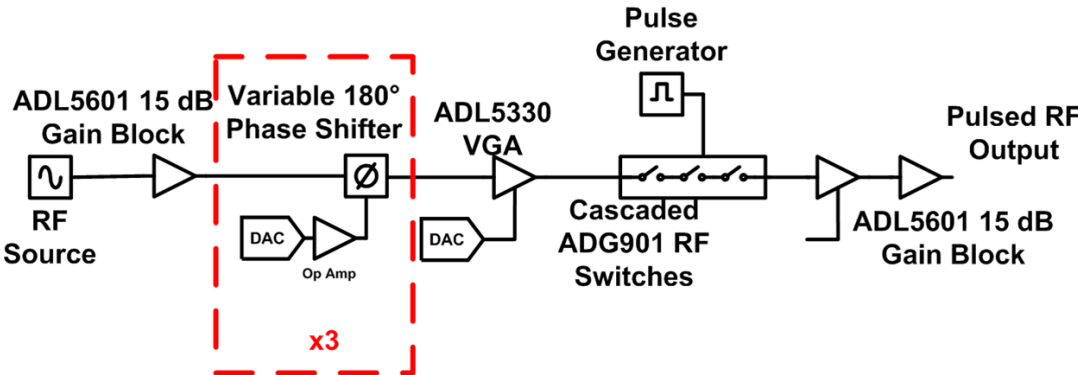


Figure 5.10: Transmit Circuit

As seen in Figure 5.11 changing the phase between the transmit channels creates a measurable change in signal level for each of the output channels. The x and y axis in these plots represents the change in phase along the corresponding physical axis. Peaks in each of these plots corresponds to when the beam is pointed at that receive point. At Channel 1 and 4 the maximum occurs with opposite phasing conditions, likewise for channel 2 and 3. This is intuitive since these elements are physically opposite each other as seen in Figure 5.9. Just as importantly the location where there is a peak for one channel corresponds to a reduced signal level on the other three. By utilizing a threshold level each channel can be selectively communicated to.

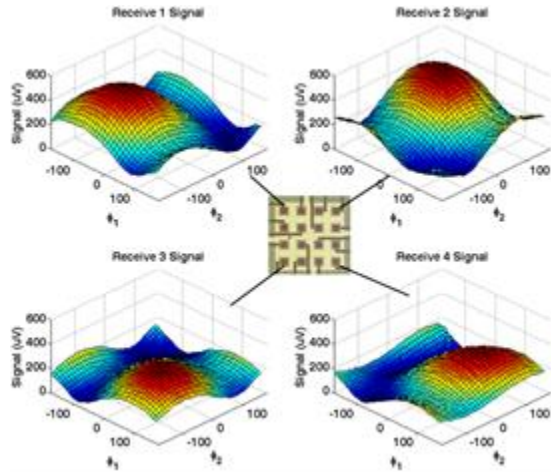


Figure 5.11: Phasing Plots

An FPGA is used to generate a bit-stream to trigger the pulse input of the phase tool.

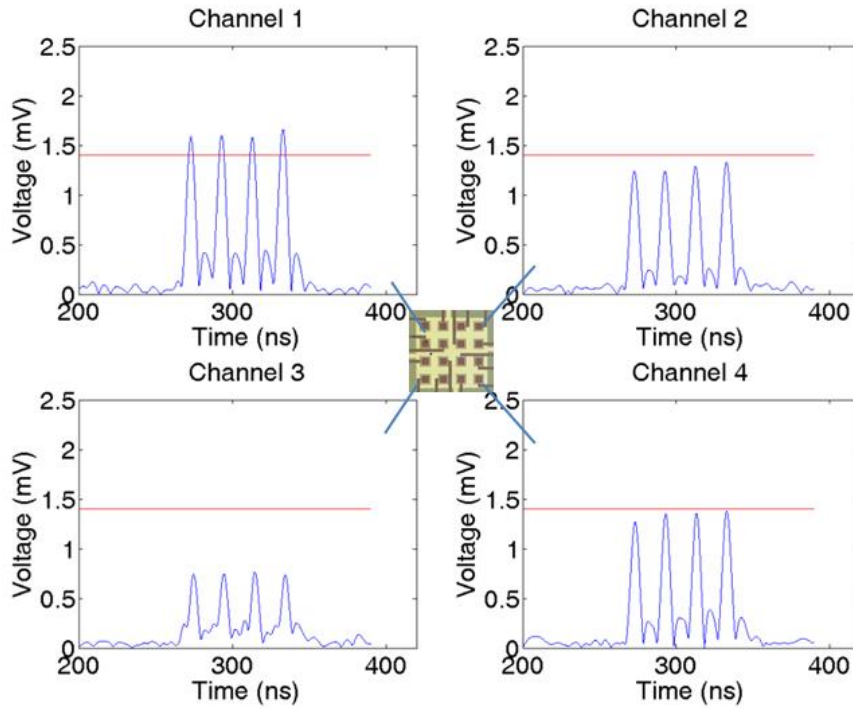


Figure 5.12: Sample time capture of phasing plots

As can be seen in Figure 5.12, by selecting a threshold value for the 4 channels and changing the relative phases one channel receives the bit stream at 100 Megabits per second, while the other 3 do not. Data rates as high as 120 Megabits per second have been measured.

5.6 Conclusions and Future Work

A reconfigurable ultrasonic communication channel in silicon wafers, utilizing aluminum nitride piezoelectric transducers, at a data rate of 120 Megabits per second, has been successfully demonstrated. So far the limitations encountered are not fundamental or associated with the transducers or acoustic channel but instead with the instrumentation, a problem which could be mitigated with CMOS integration. The biggest limits to the system performance come from (1) The bandwidth of commercial RF components used in testing (2) the input impedance of the commercial RF components, as well as the PCB board parasitic capacitance reducing the signal level. Data rates above 120 Megabits per second are limited by the bandwidth capability of the custom phase generating tool used in these experiments, and specifically the rise time of the commercial RF switches used to generate the bit stream. Work is progressing on an integrated solution where transmit and receive electronics are integrated directly with the piezoelectric transducers on silicon with CMOS electronics. One effort is using flip chip bond pads and passive arrays bonded to a CMOS die. Another is the Sandia 350nm CMOS foundry with the passive Aluminum Nitride process deposited directly on top of the CMOS stack.

Chapter 6

DEMONSTRATION OF A MIXED CMOS AND ALN PROCESS FOR ULTRASONIC COMMUNICATIONS LINK

6.1 *Introduction*

Up until now the analysis of the channel has neglected the important aspect of the drive and sense electronics. Though the electric to acoustic conversion and the acoustic channel itself have low loss, it is still necessary to drive the transmit pixel and to convert the received signals back to digital signals, using integrated circuits. These circuits consume additional power and add additional noise to the signal path, resulting in a higher energy per bit in signal transmission. Additionally integrating these piezoelectric transducers with CMOS needs to be demonstrated. This is a common challenge with integrated on-chip optical waveguides for communication as well. Though the waveguides can be lower loss than the metal interconnects paths, the power needed to generate light from the laser, as well as peripheral tuning circuits and the detector, significantly increase the energy per bit [86].

There has been some success with using low-voltage signaling CMOS circuits as a method of reducing the energy per bit [24]. In a CMOS digital chain the amount of energy consumed depends on the capacitance of the line and the voltage level. Smaller transistors have led to smaller capacitances, but the capacitance of long lines has not scaled as fast as the transistor dimensions. At the simplest level the power consumption due to CMOS switching is due to charging and discharging the capacitance between gates. This is expressed as

$$P_{switching} = \frac{1}{2}CV^2f_{CLK} \quad (6.1)$$

The simplest option to reduce power is to reduce the voltage swing as it is a function of voltage squared as seen in Equation (6.1). This still has the added burden of the transmit and receive electronics consuming power, but effectively at high data rates the energy per bit is lower than that of CMOS, thus it's adoption. Compared to optics, on chip acoustics is much easier to integrate with with these types of circuits. The only addition to the physical fabrication process is the inclusion of the piezoelectric transducers. Otherwise the types of electronics for interfacing with the piezoelectrics are already used in traditional CMOS circuits, unlike in optics, which requires integrated lasers and photodetectors. This chapter will demonstrate several of the circuits tested in connection with the ultrasonic channels and demonstrate a single transducer pair communication channel with integrated receive amplifier.

6.2 *Integrated Circuits*

There are two primary circuits of interest investigated for use in high frequency ultrasonic communication channels in silicon. One relating to the receiver and the other the transmitter. In typical RF systems the first stage of a receiver chain is a low noise amplifier (LNA). This is the most significant circuit on the receiver path because it directly interfaces with the receiving piezoelectric transducer. Any circuit in the receiver chain after this point is subject to traditional CMOS circuit design since the signal is a voltage signal at the output of the LNA. Rather than design specific circuit architectures, the remainder of the receiver chain for experimental results is processed

using a high frequency sampling oscilloscope and digital signal processing techniques to demodulate and characterize the signal after acquisition.

Traditional transmit systems use a Power Amplifier (PA) as the final stage connected to the transmitting antenna, delivering high levels of power. For ultrasonic communication the high power is not necessary, partly because of beam confinement, but the low output impedance is as it increases the power transfer efficiency to the transmitting transducer. For the use of transducers in a phased array it is important to have a circuit which is able to generate a sinusoidal output with both phase and amplitude controlled by the circuit. This circuit will be called the phase rotator or phase shifter.

6.2.1 Receiver Amplifier

The first circuit in an RF receive sub-system is a low noise amplifier (LNA). The simplest implementation of this is a common source amplifier. Typically the common-source configuration requires a few transistors, active in addition to biasing transistors, along with passive components for frequency selection. For the size scale required for on-chip sonar it is impractical to design the system with inductors given their large physical size needed to achieve needed inductance. An inverter can also serve as a LNA in the resistor feedback inverter amplifier configuration. This allows for a compact system for the first stage of the receiver, the schematic of which is shown in Figure 6.1.

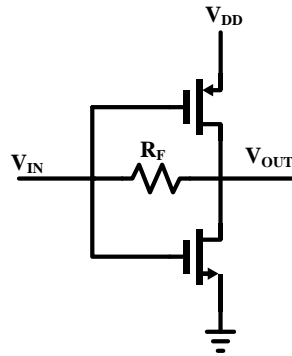


Figure 6.1: Inverter Based Receiver LNA. The feedback resistor biases the inverter in the active gain region.

In principle near the switching voltage an inverter is a high gain amplifier. Consider a sketch of the voltage transfer characteristic of an inverter shown below.

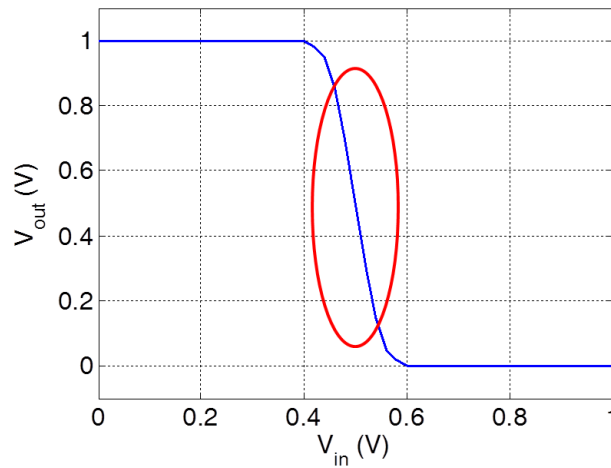


Figure 6.2: Sketch of the voltage transfer characteristic of a CMOS inverter. The highlighted red region is the region of high gain.

Due to process variations, and the narrow range of input voltages for amplification, without biasing the inverter correctly, would tend to latch the inverter to one voltage or the other with minimal gain. The primary purpose of the feedback resistor is such that the inverter biases itself around the switching voltage, as such it is typically a large value, typically greater than the output resistance of the transistors (r_{on}). In order to investigate the performance of the system consider the small signal model of the inverter based receiver shown in Figure 6.3.

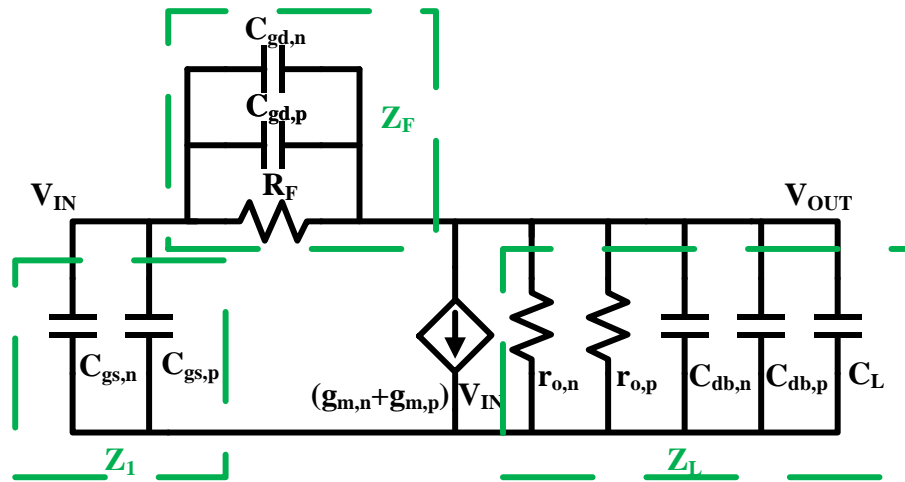


Figure 6.3: Small signal model for double g_m inverter amplifier

Groups of impedances have been lumped together and designated as Z_1 , Z_F and Z_L . As previously established for maximum power transfer the input impedance of the amplifier stage needs to match the output impedance of the transducer. From the small signal model the input impedance is

$$Z_{in} = \frac{Z_1(Z_L + Z_F)}{Z_1 + Z_F + Z_L + Z_1 Z_L (g_{m,n} + g_{m,p})} \quad (6.2)$$

Considering only the resistive components of the input impedance then

$$Z_{in} = \frac{R_F + R_{out}}{1 + (g_{m,n} + g_{m,p})R_{out}} \quad (6.3)$$

Where R_{out} is the parallel combination of the two r_o .

$$R_{out} = (r_{o,n} || r_{o,p}) \quad (6.4)$$

As the feedback resistance becomes very large the input impedance converges to Z_1 ; the gate capacitance of the two transistors. This allows for some degree of control of the receiver input impedance. With the difficulty of designing high value resistors in a small area, it can be useful to help design the input impedance. The amplifier gain can be determined to be

$$A_v = \frac{\frac{1}{Z_F} - (g_{m,n} + g_{m,p})}{\frac{1}{Z_F} + \frac{1}{Z_L}} \quad (6.5)$$

For large values of Z_F this converges to

$$A_v = -(g_{m,n} + g_{m,p})Z_L \quad (6.6)$$

As can be seen in Eq. 6.4, the feedback resistance decreases the overall gain. The primary pole of this system is a result of the output impedance. In principle a single inverter driving itself in an advanced node can operate to extremely high frequencies. However, the pole is dominated by the load node, so any additional transistors placed

at the output will load and decrease the bandwidth of the amplifier. Primarily the circuit RC time constant, which determines the bandwidth, is dominated by the load capacitance and the resistance R_{out} . By increasing the W/L ratio of the inverter transistor, the bias current will increase, reducing the output impedance. The gain stays relatively flat with transistor scaling since the decrease in R_{out} is offset by the increase in g_m . Increasing W/L however leads to higher power consumption and greater circuit area. The next stage input impedance contributed to the load impedance, and hence will effect the design of the LNA amplifier.

The feedback resistor and two transistors each contribute to the thermal noise. As established previously the frequency response of transducers is high enough such that $1/f$ noise can be ignored at the GHz frequencies used for ultrasonic communications. The feedback resistor and the two gain transistors all contribute to the noise power at the output. Considering the noise current from the 3 sources driving the output impedance results in the output noise power of

$$P_n^* = 4kT \left(\gamma_n g_{m,n} + \gamma_p g_{m,p} + \frac{1}{R_F} \right) R_{out} \quad (6.7)$$

Where $\gamma_{n,p}$ is a technology dependent parameter. It is often quoted for long channel transistors as 2/3 [88]. As the W/L ratio increase, the g_m for both transistors increases, but the output resistance decreases for reduced effect on noise power as a function of transistor scaling.

Given the variation in transistors from one technology to the next it is difficult to give a general case and a single number representing the effect of the receiver on the acoustic communication channel. Several different technologies have been used to

build circuits for this purpose. With a completely integrated system, the parasitic capacitance and resistance associated with large path lengths can be nearly negligible. However, while developing this technology the circuits are often separated from the transducers on another physical chip. This results in large parasitic capacitance associated with the bond pads between the two circuits. This requires a large buffer in order to drive the signals on and off the chip. Since the input capacitance of the buffer is large due to its large physical size the amplifier needs to have a larger W/L ratio in order to drive it, leading to a larger amplifier size.

The first amplifier presented here was fabricated in a 65 nm CMOS node. A slight variation on the design was performed, where the feedback resistor was replaced with a transistor in the hopes of reducing the physical size, as seen in Figure 6.4

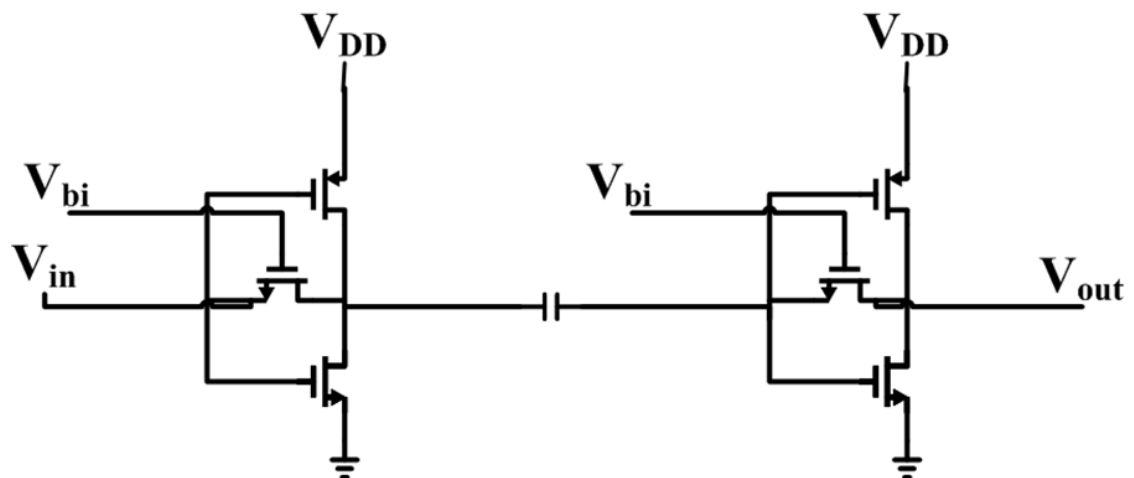


Figure 6.4: Schematic for the receiver in 65 nm technology node

Here two amplifiers are ac coupled together through a capacitor. The primary purpose of the first amplifier is an LNA to buffer the signal. The second stage is a

larger amplifier with the purpose of buffering the signal off chip. The simulated AC magnitude response of this circuit is plotted in Figure 6.5.

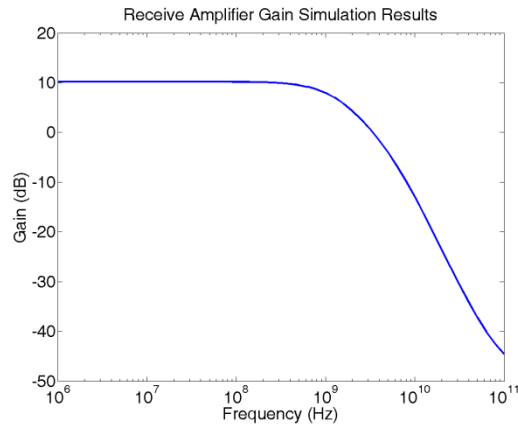


Figure 6.5: Simulated Voltage Magnitude Transfer for 65 nm Amplifier

These results indicate a 10 dB gain with a 3-dB frequency of 1.26 GHz. Though both stages are in principle relatively high gain, the feedback transistor operated in triode operates as a relatively low resistance transducer reducing the gain and increasing the bandwidth. Measurement results for 3 different bias voltages are shown in Figure 6.6.

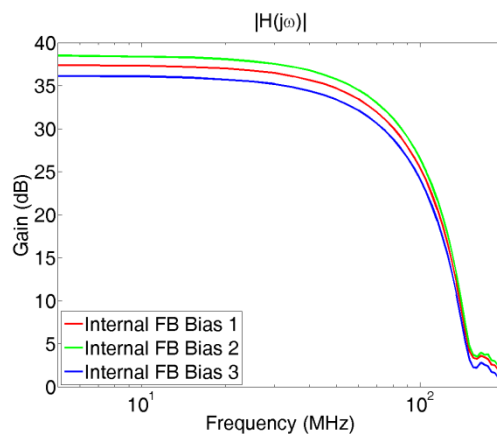


Figure 6.6: Frequency response of 65 nm receiver amplifier

The resulting amplifier has a bandwidth was 52.3 MHz gain 38.49 dB. The difference from the simulated results is likely due to the operation of the feedback transistor. Simulation results match the measured when the transducer voltage V_{bi} is reduced to zero, i.e. the feedback transistor is in cutoff. In order to drive the larger parasitics of the bond pad the second stage needs to be large. Since the input impedance heavily depends on $C_{gsn,p}$ the load capacitance for the first stage is also very large. In this case the transducer amplifier is 3 μm by 8 μm and consumes 280 μWatts . The output buffer is 15 μm by 15 μm and consumes 420 μWatts . Using a scaled amplifier used as a buffer leads to a lower frequency response as it is high gain and has high input impedance.

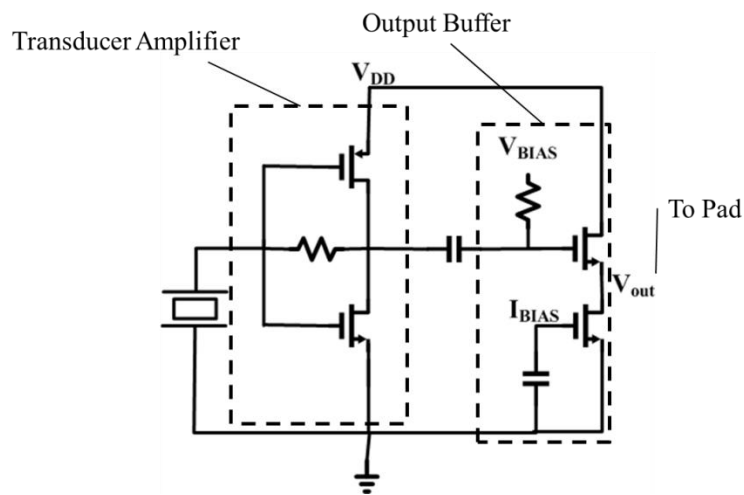


Figure 6.7: Schematic of 350 nm Amplifier

Another amplifier was fabricated in a 350 nm technology node. Although this is an older and larger node it has the advantage of being a process used by Sandia to directly fabricate integrated piezoelectric transducers on top of the CMOS stack. Due to the difficulties with the transistor in feedback, a fixed polysilicon resistor was used

as the feedback path for this design. Additionally a new buffer is used, a common drain amplifier. This has lower gain, wider frequency response, and lower input impedance. The schematic is shown in Figure 6.7.

A plot of both simulated and measured response of the amplifier with buffer is seen in Figure 6.8.

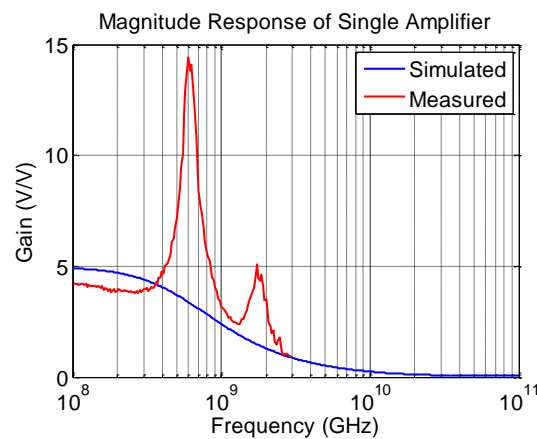


Figure 6.8: Frequency Response of the 350 nm receive amplifier

There are additional resonant peaks in the amplifier which are due to the long wire-bonds connecting the output of the CMOS chip to the test equipment. As expected this circuit takes a larger physical area than the 65 nm circuit. The transducer amplifier itself is 30 μm by 40 μm , and the buffer is 50 μm by 60 μm .

6.2.2 Phase Rotator

When driving individual elements in an array the driving element needs to selectively control the phase of the element it is driving. The operating principle of the “phase rotator” is from a trigonometric identity relating the sum of two sinusoids

$$A\sin(\omega t) + B\cos(\omega t) = \sqrt{A^2 + B^2}\sin(\omega t + \tan^{-1}(\frac{B}{A})) \quad (6.8)$$

Depending on the precision of A and B, any combination of phase and amplitude can be generated by controlling the amplitudes of the input sine and cosine. Generating local sine and cosine signals from a local oscillator will be described shortly. Once the two signals are available on a chip they can be combined with the phase rotator shown in Figure 6.9.

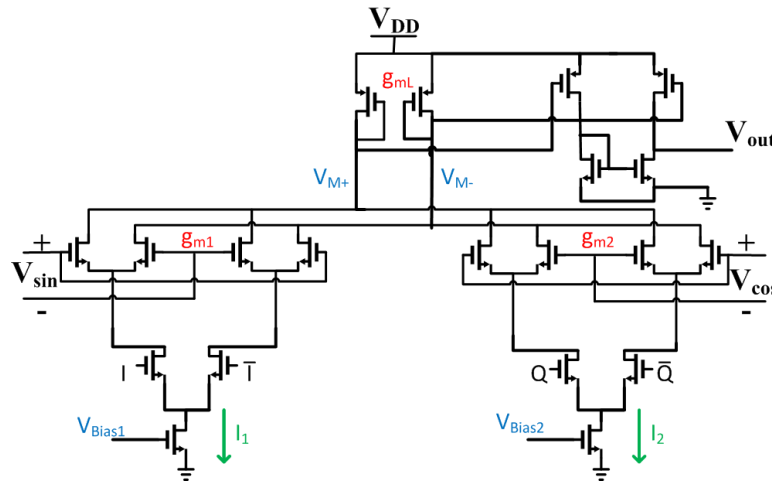


Figure 6.9: Circuit Schematic of the Phase Rotator Transmit Circuit

There are two branches of current and signal flow in this circuit. On the left is a balanced mixing pair driven by the sine or In-phase (I) component. The right is driven by a cosine or Quadrature component (Q). The values of A and B from Equation (6.8) are controlled by the voltages labelled V_{Bias1} and V_{Bias2} , which change currents I_1 and I_2 . These currents are summed at the load transistors. The output stage of the phase rotator is a buffer to drive the transducers. The input of this buffer is the voltage V_M

$$V_M = V_{M+} - V_{M-} = \frac{g_{m1}V_{sin}}{g_{mL}} \sin(\omega t) + \frac{g_{m2}V_{cos}}{g_{mL}} \cos(\omega t) \quad (6.9)$$

If the values of V_{sin} and V_{cos} are equal to V , then the amplitude of the voltage at the mid point from Equation (6.8) is

$$A_v = \frac{V}{g_{mL}} \sqrt{g_{m1}^2 + g_{m2}^2} \quad (6.10)$$

The values of g_{m1}^2 and g_{m2}^2 are proportional to their respective currents I_1 and I_2 . Provided all transistors are matched, then the current flowing into the load transistor will be proportional to the sum of the currents I_1 and I_2

$$g_{mL} \propto \sqrt{\frac{I_1 + I_2}{2}} \quad (6.11)$$

Additionally the phase of the output signal from this configuration is determined by

$$\phi = \sin^{-1}\left(\frac{g_{m1}}{\sqrt{g_{m1}^2 + g_{m2}^2}}\right) \quad (6.12)$$

If the sum of the current is kept constant, then the amplitude will remain constant and the phase will nearly shift linearly with the change in current. The maximum required phase shift is 360 degrees since any phase amount which is greater can be reduced to the 0-360 degree range. The voltages V_{Bias1} and V_{Bias2} are only capable of increasing the magnitude of the current levels, not the polarity. Therefore the

maximum phase shift that can be accomplished is 90 degree difference. To allow for a full 360 degree phase shift the two pairs of transistors to allow for both positive and negative I and Q signals to propagate to the output. The transistor gates I and \bar{I} with Q and \bar{Q} are complementary digital signals which select the polarity of the input I and Q signals.

To accomplish the digital control of the phasing a differential current digital to analog converter (DAC) is used to set the bias voltages V_{Bias1} and V_{Bias2} . A 4 bit current steering DAC allows for 4-bit phase resolution over a single quadrant, and the digital control of the 4 quadrants allows for 6-bits of resolution for the entire 360 degree phase space. The schematic for the DAC is in Figure 6.10.

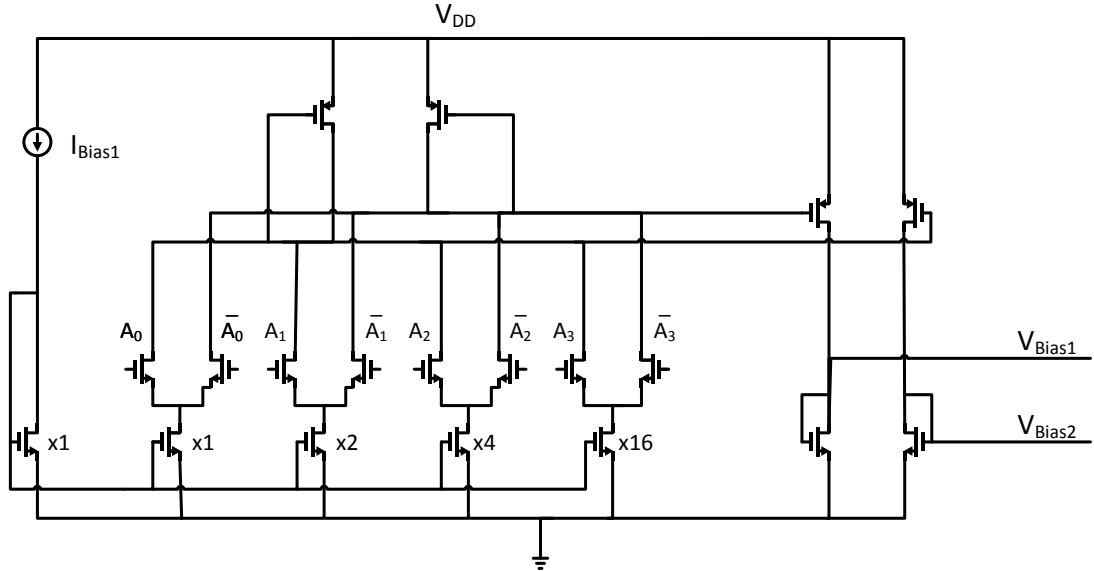


Figure 6.10: Schematic for 4-Bit differential current DAC

Here an off chip reference current, I_{Bias1} , is mirrored proportionally to the different bits. The bits are complementary so as to steer the current along one path or the other.

Additionally the memory storing it is a pair of flip flops, which stores complementary values.

In advanced CMOS nodes the square law voltage current dependence becomes a less valid model for transistor behavior. Additionally, process variations make it difficult to design analog circuits in general. To overcome these challenges, a common practice in RF is to utilize square waves instead of single tones. In this case the fundamental component of the I and Q are at the appropriate phase and then there is additional signal content at the harmonics. At the receiver, demodulation techniques are used to filter these harmonic components from the primary signal of interest [28]-[31].

By using square wave clocking, then local oscillator signaling is much easier on chip. Taking a single differential signal in and passing it through a set of coupled flip flops generates both the I and Q components and their complements on chip. Then using inverters allows for simple buffering and distribution to an array of phase rotators.

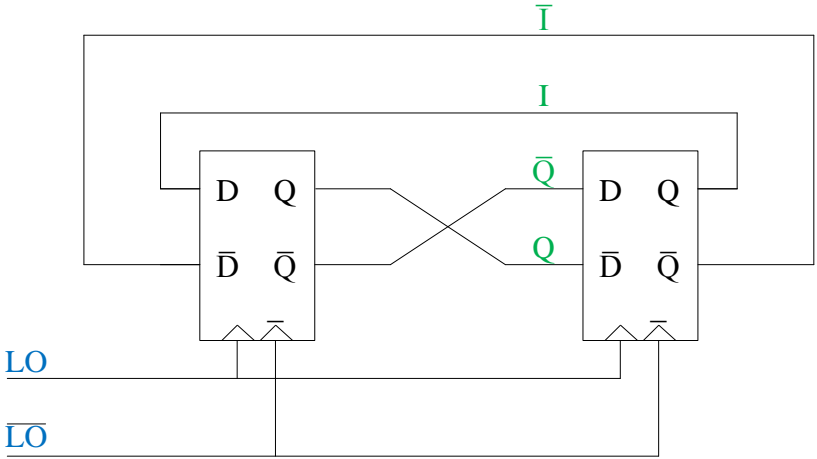


Figure 6.11: Flip Flops for local quadrature clock generation

In order to drive the signals onto off-chip loads, large buffers are needed. Since the signals are square, a simple buffer to use is a chain of progressively larger inverters. This circuit was realized in a 65 nm technology node yielding the following result in Figure 6.12.

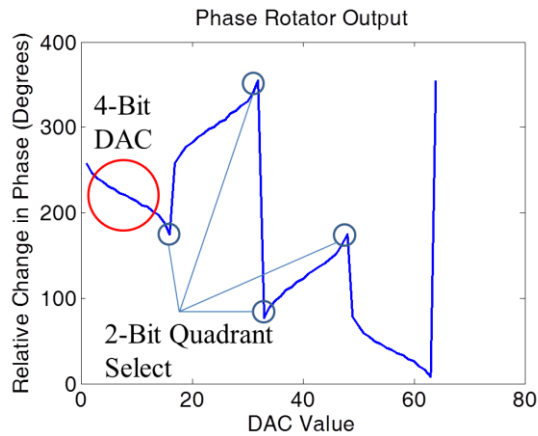


Figure 6.12: Phase rotator output phase as a set by a 6-bit phase DAC

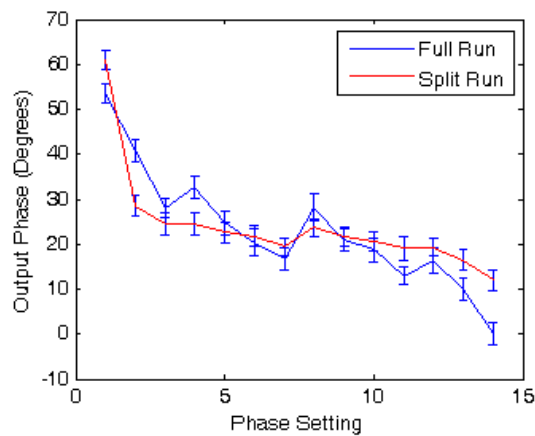


Figure 6.13: Measurement Results of 28 nm Phase Rotator over a single quadrant.

Considering only the phase rotator core itself, as seen in Figure 6.9 then the circuit size is 12 μm by 15 μm . The maximum frequency of this circuit, including the buffers is 1.2 GHz. It consumes a DC power of 480 μWatts . The circuit architecture was fabricated in Samsung 28 nm node. The measurement results are shown in Figure 6.13.

There exists greater nonlinearity in the measurement results captured here. Part of this is due to the process variation of minimum size transistors. The biggest effect these variations have is on the matching of transistors in the current steering DAC. Additionally the current mirror transistor which takes the analog voltage at the rotator itself can result in a different current than that at the DAC, which manifests as errors in the programmed phase. Additionally the harmonic components of the signal cause a distortion at the output stage of the rotator. When the frequency is too low the harmonic components effect the output signal such that rather than a linear phase shift, there is a considerable nonlinear stepwise phase versus DAC code dependence, as shown in Figure 6.14.

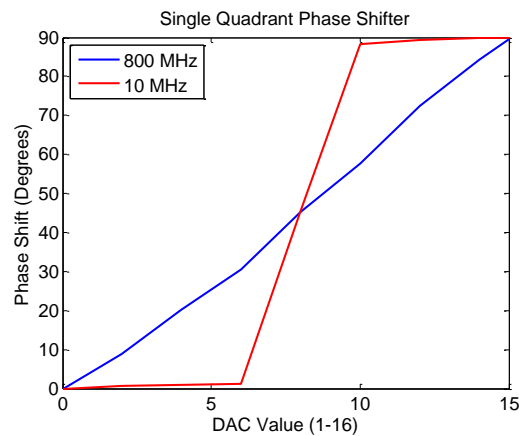


Figure 6.14: Results from 28 nm phase rotator

The phase jumps from one quadrant to the other at roughly the half way point when switching the current. Some of this can be compensated for reducing the bias current, however this is not an option at very low frequencies. This results in a minimum frequency under which the circuit will perform as expected. As expected, being in a lower technology node results in a smaller phase rotator at 7 μm by 7 μm . The max frequency including the buffers is higher at 2 GHz. It consumes a total power of 200 μWatts .

For both of these technologies, the sizes reported only included the rotator core. There is however a set digital peripheral circuits for addressing each pixel, holding memory for each phase setting, an digital to analog converter and a digital pulser for modulating the carrier wave. These can be located away from the array with wires routing to the rotators for each pixel, but it still consumes significant area. The clock generator is less problematic as there is only one for all pixels. The DAC consumes 15 μm by 20 μm in 65 nm and 12 μm by 13 μm in 28 nm. They also add a minimal amount of power compared to the rotators with 12 μWatts at 65 nm and 3 μWatts at 28 nm. The remaining digital periphery consumes 20 μm by 50 μm in 65 nm and 20 μm by 30 μm in 28 nm.

6.3 Sandia 350nm Tapeout Layout and Experimental Results

The Sandia 350 nm fabrication process has been used in the past to fabricate piezoelectric devices directly on top of the CMOS stack [32]. The 350 nm amplifier characterized here was used in this process to directly interface with a piezoelectric transducer in a two element transmit receive communication channel. The transmit transducer is directly connected to an output pad and is driven with an RF pulse. The

receive transducer is buffered through the amplifier which drives a pad off chip to an oscilloscope and demodulated and filtered using MATLAB. This setup is shown in Figure 6.15.

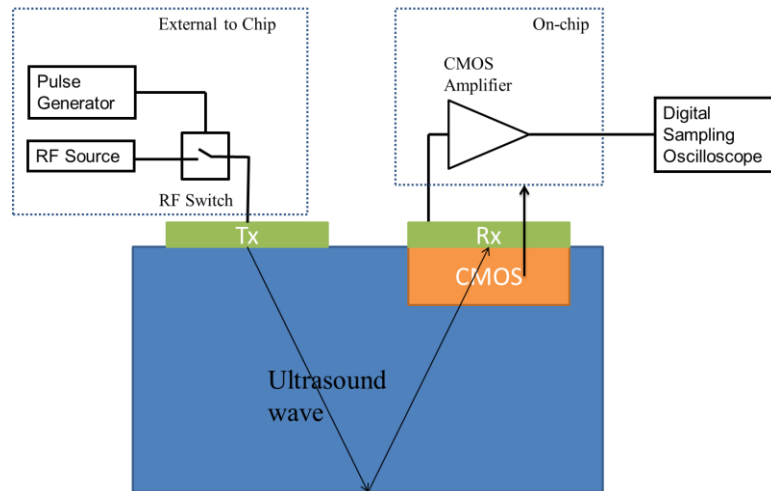


Figure 6.15: Transducer location with integrated amplifier

The two transducers are both sized $80\ \mu\text{m}$ by $50\ \mu\text{m}$ and are $3\ \mu\text{m}$ thick. This thickness was chosen as it was the thickest layer that the fabrication facility could confidently grow, and would allow for the lowest center frequency of the transducers given the low f_T of the transistors in this process. They are positioned such that the $50\ \mu\text{m}$ edge is $40\ \mu\text{m}$ apart from each other. The amplifier used is the same as that described in Section 6.2.1. The amplifier was used and the frequency characteristics for the channel were measured resulting in Figure 6.16.

Due to local oscillator (LO) feedthrough the acoustic reflected pulse is either greater than or less than amplitude value of the background signal. In Figure 6.16, both of these amplitudes are measured and presented. This is due to the fact that the phase of the LO is relatively independent of frequency but the time delay of the

acoustic pulse is independent of frequency, meaning the phase is shifting. There is a regular interval between peaks in the detected signal which comes from this time delay, which works out to approximately 6 MHz.

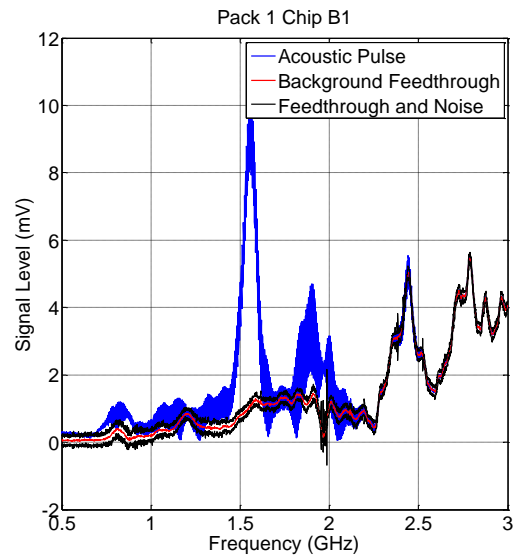


Figure 6.16: Frequency Transfer Characteristic of the 1-D Channel with integrated amplifier

Of particular interest is the lower frequency signals, in the range of 750 to 850 MHz, previously undetected due to the low amplitude of the transducers, which are now detected with the amplifier on. This demonstrates successful integration of CMOS electronics with ultrasonic transducers on CMOS chips for an in silicon communication channel.

Chapter 7

DEMONSTRATION OF A GHZ FINGERPRINT SENSOR BASED ON MEASURING REFLECTED ACOUSTIC SIGNALS

Biometric sensors are important for ensuring secure access to digital devices. This interest is brought upon by the desire for secure, low power method of personal identification, integrated into the smallest information devices. Fingerprinting is one of the most used form of biometric identification. The most common technique for fingerprint biometric identification uses optical imaging [89] - [91]. Optical fingerprinting is vulnerable as one gathers optical reflection which can be simulated by phantom fingerprints. Capacitive readout of fingerprints has found wide usage in hand held devices, primarily due to lack of any external components other than the detector chip [92] - [95]. Ultrasound is potentially a more secure method of detection because the ultrasonic impedance of skin is harder to spoof compared to optical or dielectric properties. Additionally the use of ultrasound, and penetration into tissue potentially allows for three dimensional fingerprint acquisition, and subsurface imaging, as individual blood vessel structure would be much harder to replicate into a phantom. Ultrasonic fingerprinting has also been an active area of research and development [96] - [100] and is now commercially available [101] - [102]. A potential issue with the existing ultrasonic imagers is the need for separate sensor and detection electronic chips. A one chip solution that is compatible with CMOS processing may lead to the lowest cost chip.

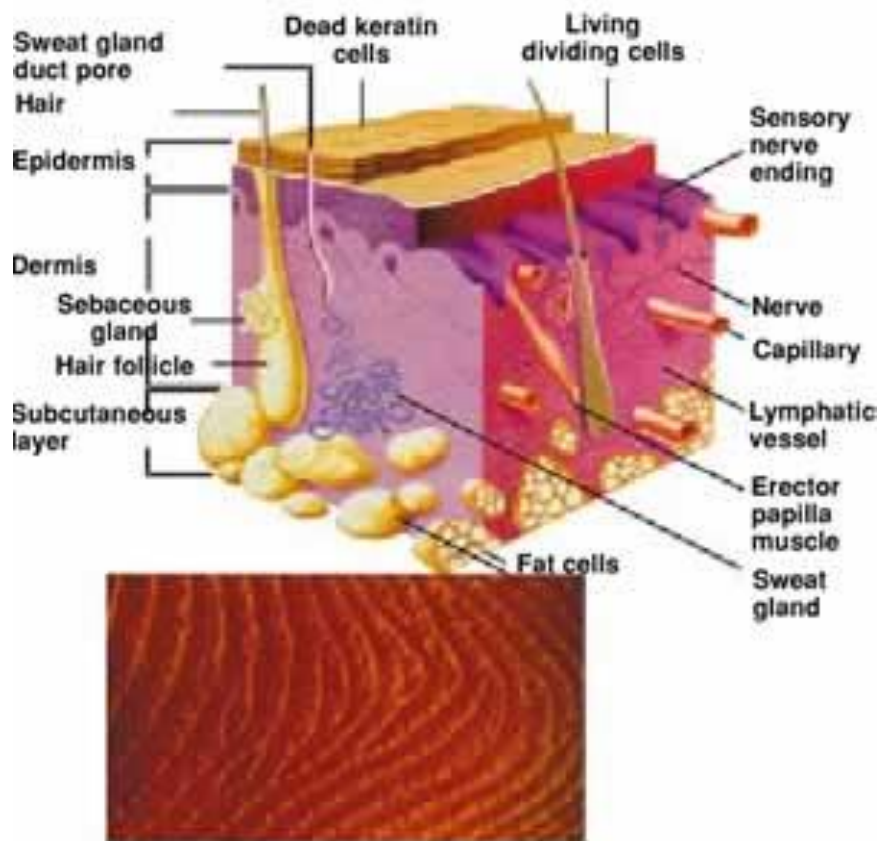


Figure 7.1: Cross section of skin surface layer [108]

We aim to develop multi-modal biometrics that includes full fingerprint imaging, finger vein imaging, thermal sensing and blood flow sensing would make it virtually impossible to fake the identity and prevent malicious system login. The information measured could provide data on blood flow that could provide medical information relevant for wearable electronics. Currently, such multimodal authentication sensor does not exist in the form factor, price point and within the power budget that would enable proliferation in the mobile computing space. In addition, emerging market

segments like wearable devices and internet-of-things devices have more constraints on form factor and power compared to the current ultrathin mobile devices.

In this chapter, work is described in which chip sonar technology that we have described before, in the context of chip-scale communications [103] - [106], is exploited for sensing applications. The key technology breakthrough in this work is the use high-frequency ultrasonic transducers in the range of 1-5 GHz as compared to transducers at a few MHz used in bulk PZT or CMUT transducers. The GHz frequency range leads to very small wavelengths in the 10s of microns to sub-micron ultrasonic pulses. These pulses propagate into tissue and reflect back for short-range imaging of human tissue and tissue surface. The very small wavelength enables the miniaturization of the ultrasonic transducer arrays and the electronic phased arrays all on one chip. Combination of phased array electronics and CMOS directly on the chip would minimize the parasitic capacitances, reducing power to microwatts instead of milliwatts per pixel, while operating at CMOS compatible sub 1.5V actuation of the piezoelectric layers. A potential challenge of imaging below the skin is the high loss of ultrasound at the GHz frequencies. However, by integrated signal processing this disadvantage can be reduced in its impact. The absorption of US in water, and hence tissue, can be approximated as

$$I(x) = I_0 e^{-\alpha x} \quad (7.1)$$

Where

$$\alpha = \alpha_0 f^2 \quad (7.2)$$

And

$$\alpha_0 = 0.134 \frac{dB}{\mu m GHz^2} \quad (7.3)$$

at 40°C [107]. At 1GHz, the absorption is 0.13 dB/μm. The US pulse would propagate 20-30 um for a 3dB reduction in intensity. Since the dead layer of skin is approximately 25um, it is feasible to be able to image below the skin surface, especially if pixels are operated at a lower frequency, and higher pulse amplitudes.

7.1 *Proposed System*

Figure 7.2 shows the overall idea of the sensor configuration. Piezoelectric thin film transducers on the top side of the chip transmit short US pulses consisting of some number of cycles of the carrier frequency. These pulses are transmitted through the wafer thickness, and undergo diffraction. Here it is important to have a reflecting boundary condition, where the waves reflect off the bottom surface of the chip and travel back to the top. The transmit pixel becomes the receive pixel, and measures the amplitude and time delay. The impedance of the material touching the silicon structure affects the reflected signal and hence is capable of measuring the impedance. A key advantage of the above architecture for finger printing is the sense surface; the backside of the chip does not have any electronics. All of the CMOS, wire bonds, or flip-chip bond connections are on the opposite side of the chip. If another material

which is not completely matched or mismatched to silicon is placed on the backside, then a portion of the signal will travel into the material and a portion will be reflected. The reflected signal will have amplitude and phase which depends on the mechanical properties of the backing material. The acoustic impedance of skin is much larger than that of air. It is possible to distinguish between the ridge of a fingerprint, which would be skin in close contact with the back surface, and a valley, which is an airgap. This contrast could be used to acquire an image of a fingerprint if a finger is scanned across a transducer or if an array of transducers is used to scan the finger, as seen in Figure 7.2.

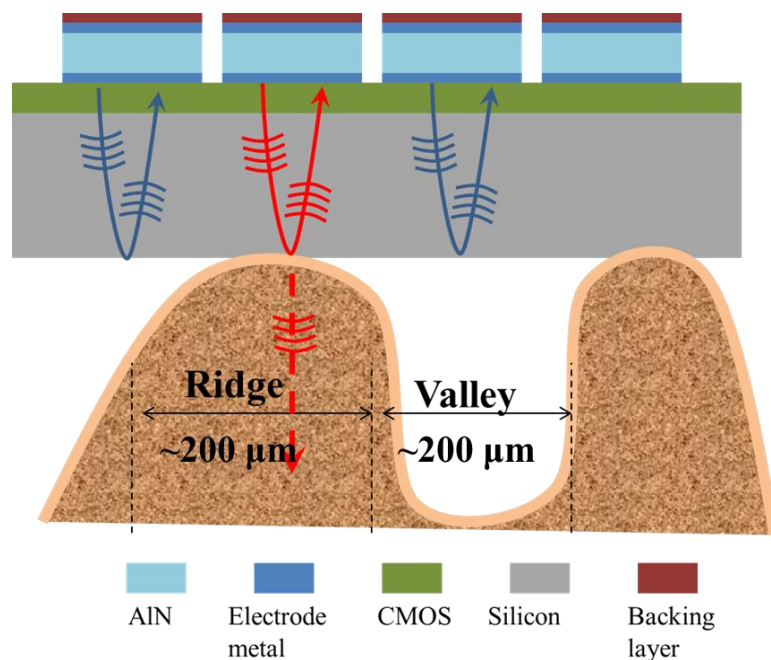


Figure 7.2: Proposed integrated CMOS and Ultrasonic Transducers. The pulses are reflected off the back surface of the silicon chip and the phase and amplitude of the reflected signals are related to the material on the other side.

In addition to impedance contrast imaging it is possible to use the T/R system to measure acoustic properties of materials. This may be useful in identifying properties such as the ripeness of a fruit, or the health of tissue. By interrogating a sample and measuring the reflected signals the value of the acoustic impedance could be measured, instead of just verifying that two signals are different. Furthermore, if the tissue material is lossy, then by evaluating across a band of frequencies would enable measurements of the intrinsic loss of the material. By using thin film piezoelectrics, this allows the study of the properties in the frequency region of greater than 1 GHz.

We envision a single chip solution in which an array of piezoelectric transducers is integrated on top of a CMOS die, where all the electronics to transmit and receive are directly underneath the transducers. The use of thin film transducers allows for center frequencies >1 GHz which allows for very high resolution imaging. Transducers can be actuated and signals measured at CMOS compatible voltage levels [103], without the need for any high voltage bias or amplification, very important for low powered mobile applications. Furthermore by making the active area of the sensor the back side of the chip, it protects the sensitive CMOS electronics from ESD risk.

7.2 Transducers Layout

The devices used for imaging are aluminum nitride (AlN) and are the same as those described in [103] - [106] and in the earlier chapters. The cross section for these is shown in Figure 2. These were fabricated at Sandia National Labs using a process which has been used to integrate aluminum nitride with CMOS [32]. Another foundry process is available at the Institute for Micro Electronics (IME – Singapore) consisting of passive AlN on silicon. Work is being done with them to develop a process for

direct integration of AlN on CMOS as well as stack design for optimal signal levels [77]. The electrode thicknesses and metals are different in the IME stack, as summarized in Chapter 3.

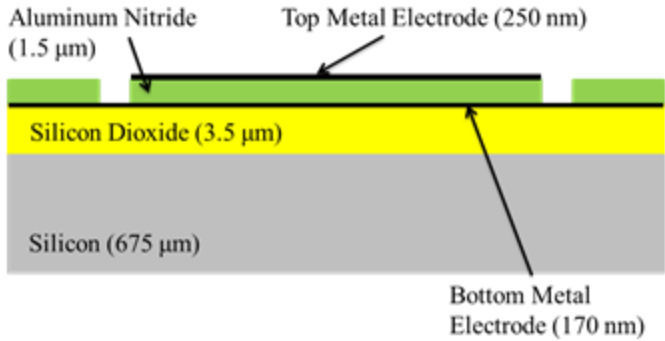


Figure 7.3: Cross section for piezoelectric transducers

The first set of these experiments was done with the same array utilized in the communication channel. A sample array with dimensions is shown in Figure 7.4.

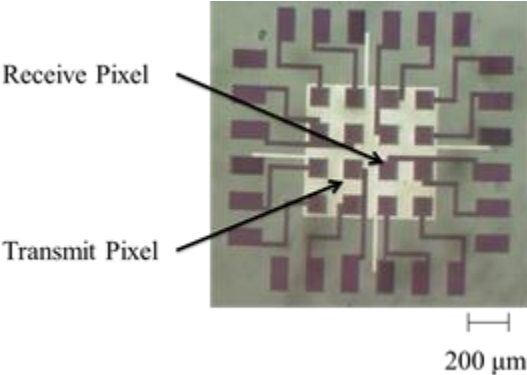


Figure 7.4: Optical capture of array of square transducers

The first experiment involves the use of a single transducer and a mechanically scanned phantom object. Building upon this is a scanner which is a line of transducers which can be used as a sensor to detect a finger print when a finger is “swiped” across the sensitive area. The layout for this is shown in Figure 7.5. There are 85 elements spaced 200 μm center to center, with a square size of 75 μm on a side.

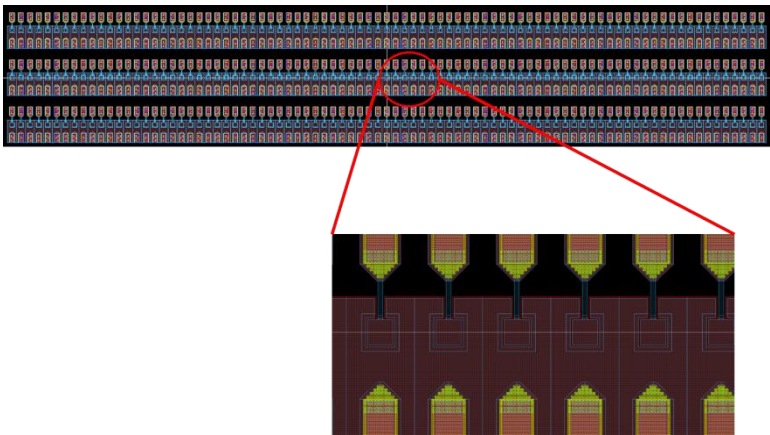


Figure 7.5: Line array of transducers for finger swipe fingerprint reader

7.3 Theory of Operation

When an acoustic wave is generated into a medium and approaches an impedance mismatch boundary some of the energy is transmitted into the second medium, while some of the energy is reflected back into the first. We define a reflection coefficient (R) as the ratio of the reflected wave (T_R) to the incident wave (T_I) and a transmission coefficient (T) as the ratio of transmitted wave (T_2) to the incident wave. It is well known that

$$\Gamma = \frac{Z_{02} - Z_{01}}{Z_{02} + Z_{01}} \quad (7.4)$$

$$T = \frac{2Z_{02}}{Z_{01} + Z_{02}} \quad (7.5)$$

Where Z_{01} is the characteristic impedance in silicon and Z_{02} is the characteristic impedance of the material on the back side. For fingerprinting there are two cases air and tissue. The characteristic impedance of silicon is roughly 17.4 MRayls whereas the impedance of air is around 400 Rayls. This results in a reflection coefficient of 0.999954, which for most practical situations is 1. Tissue, and non-dehydrated skin surface is well approximated acoustically by the impedance of water, about 1.5 MRayls, which yields a reflection coefficient of 0.85. So when there is a ridge underneath the silicon, then the signal level is expected to drop to 85% of the value, when compared to air on the back side.

There is a very large contrast between air and tissue, but it is also possible to distinguish between two more closely related materials based on the acoustic impedance. If we consider, water, isopropyl alcohol (IPA) and acetone, all three are optically transparent, low viscosity liquids, however their acoustic impedance differ. As previously established water has an acoustic impedance of 1.5 MRayls, whereas IPA has an impedance of 0.96 MRayls and acetone is 0.92 MRayls, while IPA and acetone are close they differ enough from water to be detected. The reflection coefficients for our system with water is 0.85, IPA is 0.895 and acetone is 0.899.

The theory developed up until now assumes that the acoustic impedance is independent of frequency, or that each medium is lossless. This is a fair assumption for the silicon substrate, since silicon is a low loss single crystal material [17]. More generally the material which is being measured may be lossy. The primary loss mechanism is due to viscous or viscoelastic damping, this can be represented by a change in the stress T :

$$T = \eta \frac{dS}{dt} \quad (7.6)$$

By including this factor as an additional term in Hooke's Law then the loss can be modeled as a complex stiffness coefficient

$$c = c_0 + j\omega\eta \quad (7.7)$$

It can be seen that since the stiffness coefficient is complex, so too is the impedance, and by Equation (7.4) the reflection coefficient.

Figure 7.6 demonstrates the frequency dependent effect that material loss has on the reflection coefficient. All of the data in the plots is simulated using the material properties of water but with different coefficients of viscosity. Water has a low coefficient of viscosity ~ 1 mPa s. As seen in Figure 7.6, even a coefficient of 10 mPa s, up to 3 GHz there is minimal change in the reflection coefficient. For higher viscosity coefficients the reflection coefficient drops and then slowly rises as a function of frequency. As the frequency increases, so too does the impedance of the lossy medium. Since the reflection coefficient is based on the difference in

impedances as the frequency increases the reflection coefficient reduces, but as the frequency is increased the impedance increases and in the limit as frequency goes to infinity the reflection coefficient eventually approaches unity.

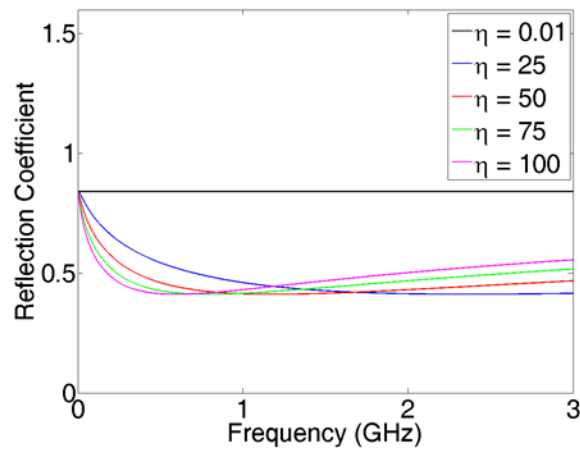


Figure 7.6: Frequency dependence of the reflection coefficient when loss is taken into consideration

7.4 *Experimental Setup*

The fingerprint scan was done with a single pixel with the fingerprint image pattern mechanically scanned over backside of the chip. The phantom was made of Mars plastic, thermally shaped into the image of the fingerprint using a silicon mold. This was mounted on to a precision motor stage and scanned across the back side of one of the AlN die. The die itself contains transducers with a center frequency of 2.7 GHz, and are a 50 μm by 50 μm square. A schematic of this setup can be seen in Figure 7.7. The receive signals were captured using a high frequency digital sampling oscilloscope and then demodulated and filtered to measure the amplitude of the receive signals. The signals were RF pulses of 50 ns, 2.7GHz sinusoids and the

amplitude was measured to demonstrate contrast for the image. The noise floor was $40\mu\text{V}$, while the acquired signals were in the $300\text{-}700\mu\text{V}$ at the higher 2.7GHz .

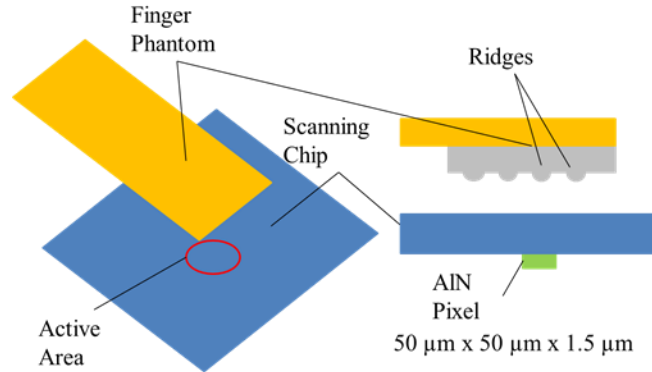


Figure 7.7: Illustration of experiment setup, where a rubber fingerprint phantom is attached to a mechanical manipulator and scanned across the sensitive area on the back of the silicon chip

To demonstrate the capability of distinguishing materials a similar setup was used where droplets of water, IPA and acetone were placed on the active area and the signal levels were captured for each material. The transducers for this experiment were $2\ \mu\text{m}$ thick squares, $50\ \mu\text{m}$ by $50\ \mu\text{m}$, and have a center frequency of $1.3\ \text{GHz}$. Once the signals are captured they were normalized to the signal level of the clean air-backed transducer. The signals were $50\ \text{ns}$ sinusoids, swept from $1.25\ \text{GHz}$ to $1.35\ \text{GHz}$ and then normalized to the air-backed case. At these $1.25\text{-}1.35\ \text{GHz}$ range, the signal levels were in the 20mV range, providing a much higher SNR, compared to that for the fingerprint.

A larger system for interrogating multiple pixels is also developed. The schematic is seen in Figure 7.8.

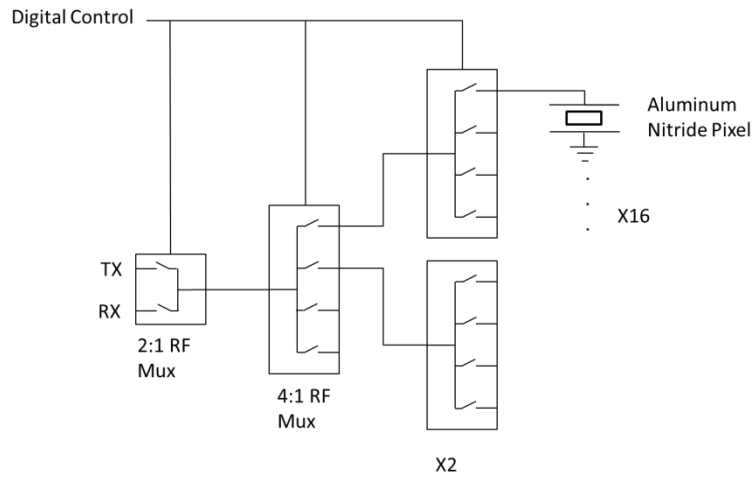


Figure 7.8: Schematic of 16 pixel fingerprint interrogation system

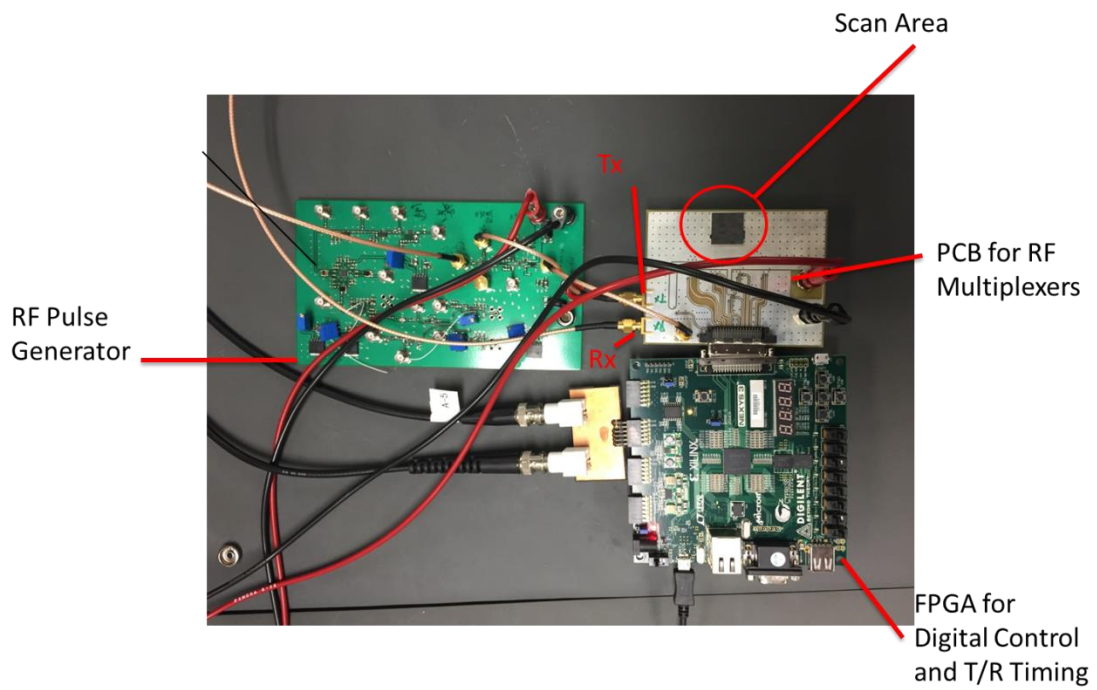


Figure 7.9: Circuit setup for finger print swipe setup

Here a digital controller, in this case a Field Programmable Gate Array (FPGA) is connected to an RF switch matrix. These controls are used to sequentially transmit and receive from each pixel in a line of 16. In this manner a low resolution image with pixels $75\ \mu\text{m}$ by $75\ \mu\text{m}$ squares spaced $400\ \mu\text{m}$ apart can be measured and a finger can be “swiped” across the sensitive scan area can be gathered. This system is shown in Figure 7.9. There are 3 boards, the FPGA for control, a custom PCB for both the RF pulse generation and the other contains the RF switch matrix.

7.5 *Experimental Results*

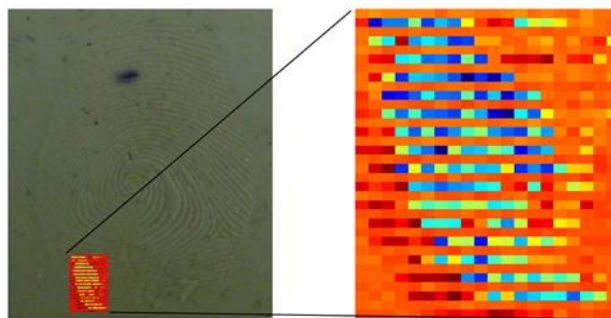


Figure 7.10: Results of fingerprint mechanical scan

As seen in Figure 7.10 as the image was scanned across the active area the signal level changed enough to distinguish between a ridge and a valley. With only air on the back side, the signal level of the received signal was on the order of $700\ \mu\text{V}$, and the standard deviation of the signal was measured to be $40\ \mu\text{V}$. When the ridge was underneath the transducer, or when the solid block itself was placed underneath the transducer the signal level dropped to the range of $300\text{-}400\ \mu\text{V}$, well above the noise

levels. The image of the captured region is overlaid onto a photograph of the phantom in Figure 7.10.

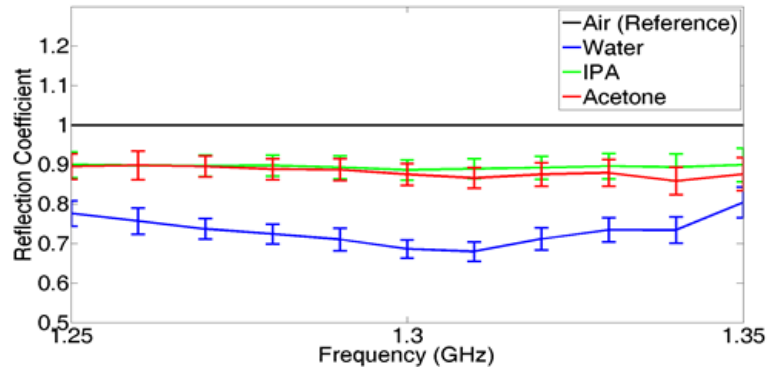


Figure 7.11: Frequency dependent result reflection coefficient for 3 different materials

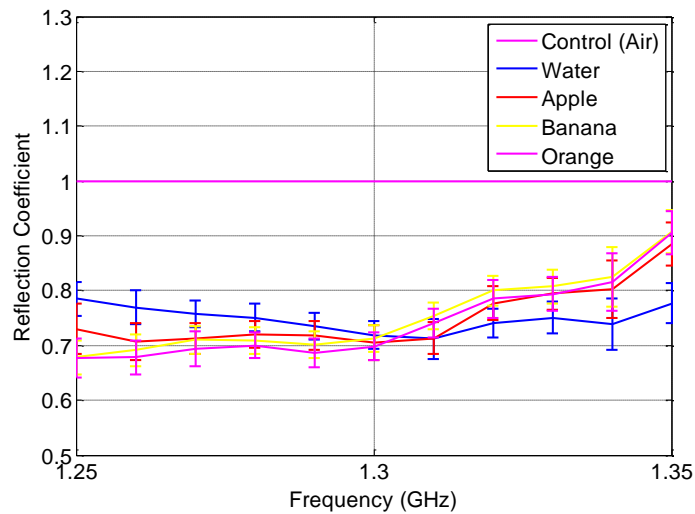


Figure 7.12: Frequency scans of reflection co-efficients for different fruits showing different frequency dependent behavior

Figure 7.11 shows the magnitude of the reflection coefficient for the three liquids. They are in close agreement with the values calculated in the theory section. Given the relatively low loss of the liquids, the relatively narrow frequency range of the scan and the sensitivity of our measurement system, not much can be said of their loss values.

Furthermore, additional experiments were done to show the characteristics of different fruits and are shown below.

7.6 Conclusion and Future Work

Here an image of the ultrasonic impedance contrast of the fingerprint phantom has been successfully demonstrated. This demonstrates the feasibility of the system to image fingerprints using ultrasonic properties of tissue rather than optical properties, at frequencies greater than 1 GHz. Additionally, a system of 16 pixels in a line has been developed. This system provides a basis which can be scaled to incorporate additional pixels. Future work is progressing in developing a single chip CMOS integrated system. With the initial success of the integrated amplifier reported on in Chapter 6.

Chapter 8

PVDF ULTRASONIC TRANSDUCERS

8.1 *Piezoelectric Polymer Transducers*

In addition to the work completed using Aluminum Nitride transducers, transducers made of the piezoelectric polymer material polyvinylidene fluoride - trifluoroethylene (PVDF-TrFE) were explored. There are several reasons to explore this polymer in addition to aluminum nitride for integrated acoustic applications: (1) the ease of fabrication, (2) lower frequency response and (3) lower acoustic impedance. In order to work with on chip ultrasonic devices, any transducer material must utilize CMOS compatible processes. The aluminum nitride process is CMOS compatible as it is low temperature and utilizes a CMOS compatible metal, aluminum. The challenge is that piezoelectric aluminum nitride requires specialized equipment and recipes. The advantage of PVDF-TrFE is that it can be dissolved in a solvent and then deposited onto the wafer using standard spin-coating process techniques, allowing for easy fabrication in CNF or other in house clean room facility. Also it is susceptible to many of the same solvents and etching processes of standard photoresists. Specifically an oxygen plasma is used to etch the transducers with a 1:1 selectivity with the masking resist.

Standard ultrasound applications such as imaging operate in the 10's of MHz range. The applications presented here using aluminum nitride take advantage of effects at higher frequencies, greater than 1 GHz. Due to the material properties of PVDF-TrFE the center frequency is much lower for similar thickness aluminum

nitride films. This allows for easier design of transducers in the range from 100 Mhz to 1 GHz.

The acoustic impedance of both silicon and aluminum nitride is rather high, on the order of 10s of MRayls. While the two impedances are similar, allowing for high efficiency in converting waves between the two mediums. It is difficult to propagate waves to lower impedance regions (such as biological tissue). The acoustic impedance of PVDF is 4.3 MRayls, which is much lower and closer to biological samples on the range of 1.5-2 MRayls. This allow for greater coupling of signals off chip into biological samples.

There are a few challenges which need to be considered when fabricating PVDF-TrFE transducers. First consider the following samples

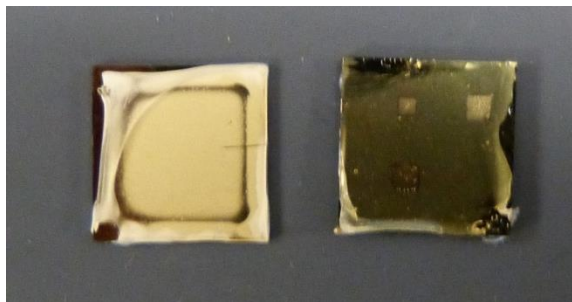


Figure 8.1: PVDF-TrFE spin coat samples. Left image is spun at 1000 rpm for 30 s. Right sample is spun at 2000 rpm for 120s

Original samples had a problem with adhesion (left in Figure 8.1), where films would peel off in the corners. Some of this was due to the square boundary condition of chip level processing. Adjustments were made to the spin recipe, where the spin

rate and time is increased which leads to better adhesion was shown (right in Figure 8.1). Even so the problems persisted when advancing to wafer level processing. Some of the resist strip chemicals such as 1165, while they do not etch the polymer, they undercut the adhesion such that the whole film peels off. The workaround implemented was after the photoresist was used to define the transducer area, a second long time exposure was used along with the developer again to remove the residual resist as the developer did not appear to have an adverse effect on the polymer's adhesion.

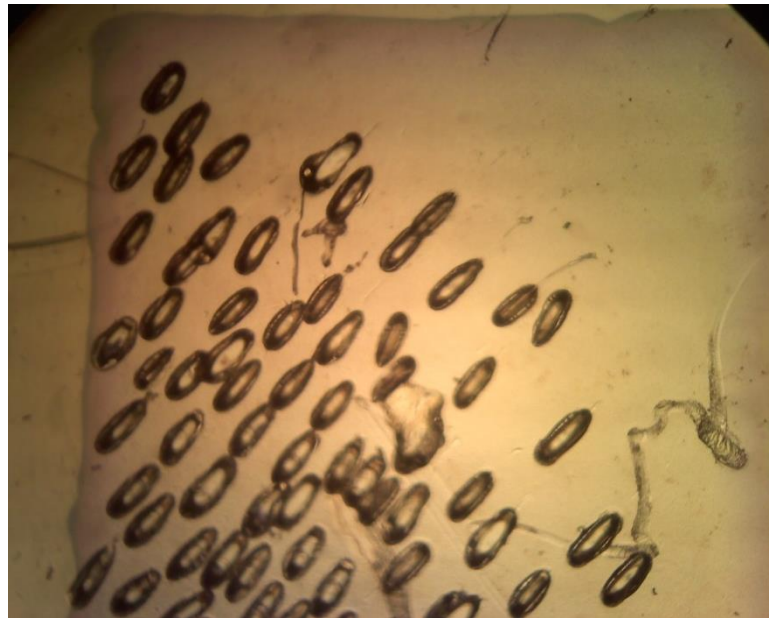


Figure 8.2: Transducer surface with wire bond marks left. These show how the bonder pressed against the film to create these pits

Another issue with the polymer is that it is mechanically very soft. The original process involved a large bottom electrode with a smaller electrode defining the top half of the transducer. When the wire-bond tool was brought into contact with this

surface it either, would not stick to the surface or would squish through the whole transducer and short the top and bottom electrodes. This can be seen below where the wire bond marks show damage to the top electrode.

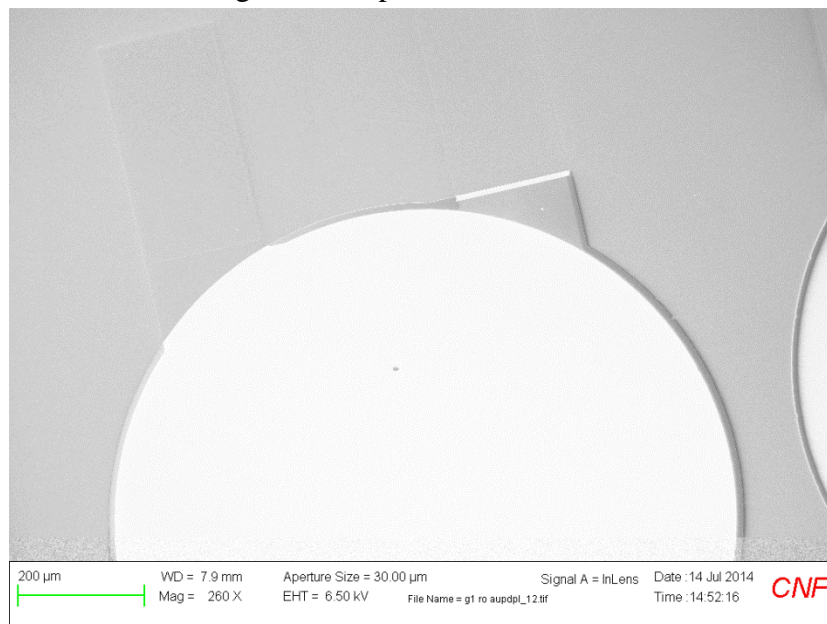


Figure 8.3: Transducers fabricated with bond sites away from the PVDF-TrFE layer

Typically in aluminum nitride processes, very little of the aluminum nitride is etched, with much of it remaining as a structural layer. This is not feasible with these devices since it is difficult to bond to a metal layer on top of the polymer. To overcome this difficulty a new structure was designed with the bond electrodes off of the transducer itself, where the PVDF layer is etched away everywhere except the transducer region. This would allow for the bond sites to be over silicon, as opposed to the transducer, as seen in Figure 8.3 below. The challenge with this structure is getting

a thick enough metal layer to ensure conductive connection from the bond pad site to the top metal electrode. The process flow for these devices is summarized in Figure 8.4.



Figure 8.4: Process flow for PVDF-TrFE Transducers

These devices were fabricated and successfully demonstrated ultrasonic wave generation and detection. A characterized pulse echo response is shown in the following

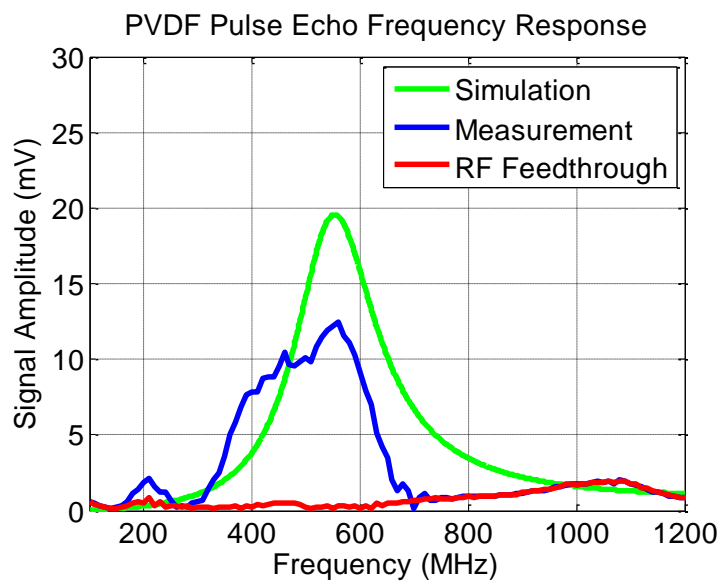


Figure 8.5: Pulse echo response fabricated transducers

Chapter 9

MATLAB FILES

```
%Plots the center frequency, gain and bandwidth of the transducer  
% as a function of the impedance ratio of the transmitting material  
% to the transducer
```

```
linet = 3;  
fons = 16;
```

```
N=10000;  
A = linspace(0.01,10,N);  
f0 = 1;  
b1 = find(A>sqrt(2),1,'first');  
b2 = find(A>sqrt(4+2*sqrt(2)),1,'first');
```

```
%Peak location  
fmax = f0*ones(1,N);  
fmax(b1:end) = f0/pi*acos(1./(1-A(b1:end).^2));
```

```
plot(A,fmax,'linewidth',linet);  
axis([0 10 0 1.2])  
set(gca,'fontsize',fons)  
grid on  
xlabel('Z2/ZC');  
ylabel('fm_a_x/f0');  
title('Peak Location')
```

```
%Peak Value  
ra_max = 4./A;  
ra_max(b1:end) = A(b1:end).^3./(A(b1:end).^2-1);  
figure  
plot(A,ra_max,'linewidth',linet)  
axis([0 10 0 10])  
set(gca,'fontsize',fons)  
grid on  
xlabel('Z2/ZC');  
ylabel('max(H(\pi\itf/\it{f_0}))');  
title('Peak Efficiency');
```

```
%Bandwidth  
a1 = A(1:b1-1);  
a2 = A(b1:b2);  
a3 = A(b2+1:end);  
B = a1.^2./(a1.^2-2);
```

```

bw1 = 2*f0*(1-1/pi*acos(-B-sqrt(B.^2+1)));
bw2 = 2*f0*(1-1/pi*acos((2-a2.^2./sqrt(a2.^2-1))./(2-a2.^2)));
bw3 = f0/pi*(acos((2+a3.^2./sqrt(a3.^2-1))./(2-a3.^2))-acos((2-
a3.^2./sqrt(a3.^2-1))./(2-a3.^2)));
BW = [bw1 bw2 bw3];
figure
plot(A,BW, 'linewidth',linet)
grid on
set(gca, 'fontsize', fons)

xlabel('Z_2/Z_C');
ylabel('Bandwidth/\itf_0');
title('Bandwidth')

%plots the frequency response of the transducer function H(j*omega)
%for the airbacked case with several different impedance ratios
%of transducer/transmitting medium

linet=3;
fons = 16;

As = [0.25 1 1.41 1.7 2];
colors = ['bgrmk'];
x = linspace(0,2,1000);
mid = find(x>1,1, 'first');

for jj = 1:length(As)

    A=As(jj);
    c = colors(jj);
    ra_hat = A*(1-cos(pi*x)).^2./(sin(pi*x).^2+A^2*cos(pi*x).^2);
    plot(x,ra_hat/ra_hat(mid),c, 'linewidth',linet)
    hold on
end

set(gca, 'fontsize', fons)
grid on
axis([0 2 0 1.5]);
xlabel('\itf / \it{f_0}')
ylabel('H(\pi\itf/\it{f_0})/H(\pi)')
% legend(['Z_2/Z_C = ' num2str(As(1))], ['Z_2/Z_C = '
num2str(As(2))], ...
%      ['Z_2/Z_C = ' num2str(As(3))], ['Z_2/Z_C = ' num2str(As(4))], ...
%      ['Z_2/Z_C = ' num2str(As(5))])
legend(num2str(As(1)), num2str(As(2)), num2str(As(3)), num2str(As(4)), nu
m2str(As(5)));

```

```

fhand =(gcf);
set(fhand,'Position',[-1200 100 620 420])

%Plots the numeric simulation of the KLM model to determine center
%frequency, gain and bandwidth of transducer response function

tic

linet = 2;
fons = 16;

Z1 = eps; %Z1-backing region
Zc = 1; %Zc-transducer material

f0 = 1; %normalized to resonant frequency
N = 2000; %number of points
fstart = 0.01; %starting frequency
fstop = 1.99*f0; %max frequency
f = linspace(fstart,fstop,N); %frequency array
w = 2*pi*f; %angular frequency
betal = pi*f/f0; %wavenumber

C0 = 1; %clamped capacitance (should cancel?)
kt = 0.5; %kt- (scaling factor?)

%KLM Model parameters
w0 = 2*pi*f0;
Zs = 0; %electrical source impedance (series)
Zr = inf*ones(size(w)); %receive impedance (parallel)
Cp = -C0./(kt^2*sinc(w/w0)); %klm negative capacitance
phi = kt*sqrt(pi/(w0*C0*Zc))*sinc(w/(2*w0)); %klm turns ratio
tic
As = logspace(-2,1,200);
% As = 1;
for jj = 1:length(As)
A = As(jj); %parameter to sweep Z2/Zc
Z2 = A; %Z2-transmitting region

%% Transducer Transmission Line Half
for ab = 1:N
%%KLM Parameters
AT(:, :, ab) = [cos(betal(ab)/2) j*Zc*sin(betal(ab)/2);...
j*sin(betal(ab)/2)/Zc cos(betal(ab)/2)]; %Transducer
half tx line
AC0(:, :, ab) = [1 1./(j*w(ab)*C0);0 1]; %Clamped
Capacitance
ACp(:, :, ab) = [1 1./(j*w(ab)*Cp(ab));0 1]; %klm negative
capacitance

```

```

    Axf(:, :, ab) = [phi(ab) 0; 0 1/phi(ab)];           %klm
transformer
    Ae(:, :, ab) = [1 Zs; 0 1];                       %electrical
source impedance
    Aer(:, :, ab) = [1 0; 1/Zr(ab) 1];                %receiver
impedance
    Ab(:, :, ab) = [1 0; 1/Z1 1];                     %backing
layer
    Al(:, :, ab) = [1 0; 1/Z2 1];                     %load layer

    %% AlN Directly on Silicon
    AF(:, :, ab) = AT(:, :, ab)*Al(:, :, ab);
    AR(:, :, ab) = [1 Z2; 0 1]*AT(:, :, ab);
    ZB = AT(:, :, ab)*Ab(:, :, ab);                   %backing
layer transformed nothing fancy
    AB(:, :, ab) = [1 0; ZB(2,1)/ZB(1,1) 1];          %parallel
resistance from "single stub tuner"

    Tfm(:, :, ab) =
Ae(:, :, ab)*AC0(:, :, ab)*ACp(:, :, ab)*Axf(:, :, ab)*AB(:, :, ab)*AF(:, :, ab);

    Trm(:, :, ab) = AR(:, :, ab)*AB(:, :, ab)*Axf(:, :, ab)^-
1*ACp(:, :, ab)*AC0(:, :, ab)*Aer(:, :, ab);

    A_total(:, :, ab) = Tfm(:, :, ab)*Trm(:, :, ab);
end

%impedance check, referenced to known input impedance equation
Z_in_tl = reshape(Tfm(1,1,:), 1,N)./reshape(Tfm(2,1,:), 1,N);
% semilogy(f,abs(Z_in_tl))
% hold on
%
% Z3 = 1./(j*w*C0).*(1+kt^2*(j*Z2*Zc*sin(betal)-2*Zc^2*(1-
cos(betal)))./( (Zc^2*sin(betal)-j*Zc*Z2*cos(betal)).*betal));
% plot(f,abs(Z3),'k')
% plot(f,abs(1./(j*w*C0)),'g')

%power in and out expressions
V_in_tl = ones(1,N);
I_in_tl = V_in_tl./Z_in_tl;

Htx = reshape(1./Tfm(1,1,:), 1,N);
Hrx = reshape(1./Trm(1,1,:), 1,N);

%Apparent power in
Pin = (V_in_tl.*I_in_tl);

%Acoustic Power generated
F2 = (V_in_tl.*Htx);

```

```

Pa = (F2.*conj(F2))/Z2;
% subplot(2,1,1)
% plot(f,abs(Pa./Pin))
% subplot(2,1,2)
% plot(f,180/pi*phase(Pa./Pin))

eta = Pa./Pin;

[eta_max, jjmax]=max(eta);
bw_lo = f(find(abs(eta)>abs(eta_max)/2,1,'first'));
bw_hi = f(find(abs(eta(jjmax:end))<abs(eta_max)/2,1,'first')+jjmax);

eff_max(jj) = eta_max;
f_max(jj) = f(jjmax);
bw(jj) = bw_hi-bw_lo;

end
toc
figure
plot(As,abs(eff_max));
title('Maximum Efficiency');
% axis([0 10 0 1.2]);
figure
plot(As,f_max);
title('Peak Response Frequency');
% axis([0 10 0 1.2]);
figure
plot(As,bw);
title('Bandwidth');
% axis([0 10 0 1.2]);
figure
plot(As,bw.*abs(eff_max));
title('Gain Bandwidth Product');

%plots KLM output frequency response of transducer for single
%acoustic matching condition

tic

linet = 2;
fons = 16;

Z1 = eps; %Z1-backing region
Zc = 1; %Zc-transducer material

f0 = 1; %normalized to resonant frequency

```

```

N = 2000; %number of points
fstart = 0.01; %starting frequency
fstop = 1.99*f0; %max frequency
f = linspace(fstart,fstop,N); %frequency array
w = 2*pi*f; %angular frequency
betal = pi*f/f0; %wavenumber

C0 = 1; %clamped capacitance (should cancel?)
kt = sqrt(0.07); %kt- (scaling factor?)

%KLM Model parameters
w0 = 2*pi*f0;
Zs = 0; %electrical source impedance (series)
Zr = inf*ones(size(w)); %receive impedance (parallel)
Cp = -C0./(kt^2*sinc(w/w0)); %klm negative capacitance
phi = kt*sqrt(pi/(w0*C0*Zc))*sinc(w/(2*w0)); %klm turns ratio
As = logspace(-2,1,200);
As = 120;
% for jj = 1:length(As)
jj=1;
A = As(jj);%parameter to sweep Z2/Zc
Z2 = 1; %Z2-transmitting region

%% Transducer Transmission Line Half
for ab = 1:N
    %%KLM Parameters
    AT(:, :, ab) = [cos(betal(ab)/2) j*Zc*sin(betal(ab)/2); ...
        j*sin(betal(ab)/2)/Zc cos(betal(ab)/2)]; %Transducer
    half tx line
    AC0(:, :, ab) = [1 1./(j*w(ab)*C0); 0 1]; %Clamped
    Capacitance
    ACp(:, :, ab) = [1 1./(j*w(ab)*Cp(ab)); 0 1]; %klm negative
    capacitance
    Axf(:, :, ab) = [phi(ab) 0; 0 1/phi(ab)]; %klm
    transformer
    Ae(:, :, ab) = [1 Zs; 0 1]; %electrical
    source impedance
    Aer(:, :, ab) = [1 0; 1/Zr(ab) 1]; %receiver
    impedance
    Ab(:, :, ab) = [1 0; 1/Z1 1]; %backing
    layer
    Al(:, :, ab) = [1 0; 1/Z2 1]; %load layer

    % AlN Directly on Silicon
    AF(:, :, ab) = AT(:, :, ab)*Al(:, :, ab);
    AR(:, :, ab) = [1 Z2; 0 1]*AT(:, :, ab);
    ZB = AT(:, :, ab)*Ab(:, :, ab); %backing
    layer transformed nothing fancy
    AB(:, :, ab) = [1 0; ZB(2,1)/ZB(1,1) 1]; %parallel
    resistance from "single stub tuner"

```

```

    Tfm(:, :, ab) =
Ae(:, :, ab)*AC0(:, :, ab)*ACp(:, :, ab)*Axf(:, :, ab)*AB(:, :, ab)*AF(:, :, ab);

    Trm(:, :, ab) = AR(:, :, ab)*AB(:, :, ab)*Axf(:, :, ab)^-
1*ACp(:, :, ab)*AC0(:, :, ab)*Aer(:, :, ab);

    A_total(:, :, ab) = Tfm(:, :, ab)*Trm(:, :, ab);
end

%impedance check, referenced to known input impedance equation
Z_in_tl = reshape(Tfm(1,1,:),1,N)./reshape(Tfm(2,1,:),1,N);
% semilogy(f,abs(Z_in_tl))
% hold on
%
% Z3 = 1./(j*w*C0).*(1+kt^2*(j*Z2*Zc*sin(betal)-2*Zc^2*(1-
cos(betal)))./((Zc^2*sin(betal)-j*Zc*Z2*cos(betal)).*betal));
% plot(f,abs(Z3),'k')
% plot(f,abs(1./(j*w*C0)),'g')

%power in and out expressions
V_in_tl = ones(1,N);
I_in_tl = V_in_tl./Z_in_tl;

Htx = reshape(1./Tfm(1,1,:),1,N);
Hrx = reshape(1./Trm(1,1,:),1,N);

%Apparent power in
Pin = (V_in_tl.*conj(I_in_tl));

%Acoustic Power generated
F2 = (V_in_tl.*Htx);
Pa = (F2.*conj(F2))/Z2;
% subplot(2,1,1)
plot(f,abs(Pa./Pin))
% subplot(2,1,2)
% plot(f,180/pi*phase(Pa./Pin))

eta = Pa./abs(Pin);

[eta_max, jjmax]=max(eta);
bw_lo = f(find(abs(eta)>abs(eta_max)/2,1,'first'));
bw_hi = f(find(abs(eta(jjmax:end))<abs(eta_max)/2,1,'first')+jjmax);

eff_max(jj) = eta_max;
f_max(jj) = f(jjmax);
bw(jj) = bw_hi-bw_lo;

```

```

%power loss determined by the input impedance model

linet = 2;
fons = 16;
Z1 = eps;
Zc = 1;

f0 = 1;
N = 2000;           %number of points
fstart = 0.01;     %starting frequency
fstop = 1.99*f0;   %max frequency
f = linspace(fstart, fstop, N); %frequency array
w = 2*pi*f;        %angular frequency
betal = pi*f/f0;   %wavenumber

C0 = 1;            %clamped capacitance (should cancel?)
kt = 0.09;         %kt- (scaling factor?)

%KLM Model parameters
w0 = 2*pi*f0;

A = 1;
Z2 = A;

pre_a = (kt^2./(w*C0)).*(1./(betal));

xr_den = sin(betal).^2+A^2*cos(betal).^2;

xahat_num = sin(betal).*(2+(A^2-2)*cos(betal));
rahat_num = A*(1-cos(betal)).^2;

xahat = xahat_num./xr_den;
rahat = rahat_num./xr_den;

xa = pre_a.*xahat;
ra = pre_a.*rahat;

pf = ra./sqrt(ra.^2+(-1./(w*C0)+xa).^2);

```

```

plot(f,pf)
eta = pf;
[eta_max, jjmax]=max(pf);
f_max = f(jjmax)

bw_lo = f(find(abs(eta)>abs(eta_max)/2,1,'first'));
bw_hi = f(find(abs(eta(jjmax:end))<abs(eta_max)/2,1,'first')+jjmax);
bw = bw_hi-bw_lo

eff_max = eta_max

z3num = j*A*sin(betal)-2*(1-cos(betal));
z3den = sin(betal)-j*A*cos(betal);

Z3 = 1./(j*w*C0).*(1+kt^2*z3num./(z3den.*betal));
I3 = 1./Z3;

%Calculates the center point of the radiation pattern as a function
of the
%fresnel parameter S

dS = 0.001;

a = 5;           %radius of transducer

dx = a/10;
dy = a/10;

S = 0.1:dS:2;

z = a.^2*S;

x = dx:dx:a;

cir_pat=zeros(size(z));
sqr_pat=cir_pat;
oct_pat=cir_pat;

tic
for jj = 1:length(z)
    int_sum=0;
    for ll = 1:length(x)
        y = 0:dy:sqrt(a^2-x(ll)^2);
        R = sqrt(x(ll)^2+y.^2+z(jj)^2);

```

```

        int1 = exp(-j*2*pi*R)./R;
        int2 = z(jj)./R;
        int3 = j*2*pi+1./R;
        integrand = int1.*int2.*int3.*dx.*dy;
        int_sum = int_sum+sum(integrand);
    end
    cir_pat(jj) = (1/(2*pi))*(4*int_sum);
end
toc
%
% uz = exp(-j*2*pi*z)-z./(a^2+z.^2).^0.5.*exp(-j*2*pi*sqrt(a^2+z.^2));

tic
for jj = 1:length(z)
    int_sum=0;
    for ll = 1:length(x)
        y = 0:dy:a;
        R = sqrt(x(ll)^2+y.^2+z(jj)^2);
        int1 = exp(-j*2*pi*R)./R;
        int2 = z(jj)./R;
        int3 = j*2*pi+1./R;
        integrand = int1.*int2.*int3.*dx.*dy;
        int_sum = int_sum+sum(integrand);
    end
    sqr_pat(jj) = (1/(2*pi))*(4*int_sum);
end
toc

tic
b = 2*a/(1+sqrt(2));
for jj = 1:length(z)
    int_sum=0;
    for ll = 1:length(x)
        if x(ll)<b/2
            ymax(jj) = a;
        else
            ymax(jj) = -x(ll)+(2+sqrt(2))/(1+sqrt(2))*a;
        end
        y=0:dy:ymax(jj);
        R = sqrt(x(ll)^2+y.^2+z(jj)^2);
        int1 = exp(-j*2*pi*R)./R;
        int2 = z(jj)./R;
        int3 = j*2*pi+1./R;
        integrand = int1.*int2.*int3.*dx.*dy;
        int_sum = int_sum+sum(integrand);
    end
    oct_pat(jj) = (1/(2*pi))*(4*int_sum);
end
end

```

```
toc
```

```
figure
plot(S,abs(cir_pat));
hold on
plot(S,abs(sqr_pat),'g');
plot(S,abs(oct_pat),'r');

legend('Circle','Square','Octagon')

%Determines the BER considering all loss mechanisms

Va_silicon = 8125; %m/s
V_aln = 1.1077e4; %m/s
t_silicon = 1300e-6; %m

% t_silicon = linspace(1e-3,2e-3,10);
f0s=[0.5e9 1e9 5e9 10e9];

for jj = 1:length(f0s)
    %% Diffraction Loss
    S = 1; %for diffraction loss location

    f0 = f0s(jj); %resonance frequency;
    t_aln = V_aln/(2*f0); %aln transducer thickness
    lambda0 = Va_silicon/f0; %wavelength

    z = t_silicon/lambda0;
    a = sqrt(z/S);
    as(jj) = a;
    dx = a/25;
    dy = a/25;
    x = -a:dx:a;
    temp = ones(length(x),1);
    X = temp*x;
    Y = X';
    xr = 0:dx:a;
    yr = 0:dy:a;
    rec_pat = zeros(length(xr),length(yr));

    for kk = 1:length(xr)
        for ll = 1:length(yr)
            int_sum=0;
            R = sqrt((X-xr(kk)).^2+(Y-yr(ll)).^2+z^2);
            int1 = exp(-j*2*pi*R)./R;
            int2 = z./R;
```

```

        int3 = j*2*pi+1./R;
        integrand = int1.*int2.*int3.*dx.*dy;
        int_sum = int_sum+sum(sum(integrand));
        sqr_pat(kk,ll) = (int_sum/(2*pi));
    end
end

%blue is the center line x/y = 0;

blue = sqr_pat(1,:);
blue = [blue(end:-1:1) blue(2:end)];
%orange is 1/4 without x/y center line but with y/x center line
orange = sqr_pat(2:end,:);
%pnk is 1/4 without x/y center line or y/x center line
pnk = sqr_pat(2:end,2:end);
%hilite = half without center line
hilite = [orange(:,end:-1:1) pnk];
%sqr_full is full pattern generated from the quarter
sqr_full = [hilite(end:-1:1,:);blue;hilite];

intens = sqr_full.*conj(sqr_full);
intens_in = ones(size(intens));

power_in = sum(sum(intens_in))*dx*dy;
power_out = sum(sum(intens))*dx*dy;
DL(jj) = -10*log10(power_out/power_in);

%% Conversion and Circuit Loss

Z1 = eps; %Z1-backing region
Zc = 1; %Zc-transducer material
Z2 = 1;
N = 2000; %number of points
fstart = 0.01*f0; %starting frequency
fstop = 1.99*f0; %max frequency
f = linspace(fstart,fstop,N); %frequency array
w = 2*pi*f; %angular frequency
betal = pi*f/f0; %wavenumber

e0 = 8.854e-12;
C0 = 9.9*e0*(a*lambda0)^2/t_aln; %clamped capacitance
kt = sqrt(0.07); %kt- (scaling factor?)

w0 = 2*pi*f0;
Zs = 0; %electrical source impedance (series)

```

```

%      Z3 = (1./(j*w*C0)).*(1+kt^2*(j*(Z1+Z2)*Zc*sin(betal)-2*Zc^2*(1-
cos(betal)))./(((Zc^2+Z1*Z2)*sin(betal)-
j*Zc*(Z1+Z2)*cos(betal)).*betal));
%      rl_i = find(f>f0,1,'first');
%      Rl = abs(Z3(rl_i));

Rl = 1/(w0*C0);
%      Rl = inf;
Zr = Rl*ones(size(w)); %receive impedance (parallel)
Cp = -C0./(kt^2*sinc(w/w0)); %klm negative capacitance
phi = kt*sqrt(pi/(w0*C0*Zc))*sinc(w/(2*w0)); %klm turns ratio

%      Z1 = Z1*(a*lambda0)^2;
%      Z2 = Z2*(a*lambda0)^2;
%      Zc = Zc*(a*lambda0)^2;
for ab = 1:N
    %%KLM Parameters
    AT(:, :, ab) = [cos(betal(ab)/2) j*Zc*sin(betal(ab)/2); ...
        j*sin(betal(ab)/2)/Zc cos(betal(ab)/2)]; %Transducer
half tx line
    AC0(:, :, ab) = [1 1./(j*w(ab)*C0);0 1]; %Clamped
Capacitance
    ACp(:, :, ab) = [1 1./(j*w(ab)*Cp(ab));0 1]; %klm
negative capacitance
    Axf(:, :, ab) = [phi(ab) 0; 0 1/phi(ab)]; %klm
transformer
    Ae(:, :, ab) = [1 Zs;0
1]; %electrical source impedance
    Aer(:, :, ab) = [1 0;1/Zr(ab) 1]; %receiver
impedance
    Ab(:, :, ab) = [1 0;1/Z1 1]; %backing
layer
    Al(:, :, ab) = [1 0;1/Z2 1]; %load
layer

    %%AlN Directly on Silicon
    AF(:, :, ab) = AT(:, :, ab)*Al(:, :, ab);
    AR(:, :, ab) = [1 Z2;0 1]*AT(:, :, ab);
    ZB = AT(:, :, ab)*Ab(:, :, ab); %backing
layer transformed nothing fancy
    AB(:, :, ab) = [1 0; ZB(2,1)/ZB(1,1) 1]; %parallel
resistance from "single stub tuner"

    Tfm(:, :, ab) =
Ae(:, :, ab)*AC0(:, :, ab)*ACp(:, :, ab)*Axf(:, :, ab)*AB(:, :, ab)*AF(:, :, ab);

    Trm(:, :, ab) = AR(:, :, ab)*AB(:, :, ab)*Axf(:, :, ab)^-
1*ACp(:, :, ab)*AC0(:, :, ab)*Aer(:, :, ab);

```

```

    A_total(:,:,ab) = Tfm(:,:,ab)*Trm(:,:,ab);
end
%Apparent power in
Z_in_tl =
reshape(Tfm(1,1,:),1,N)./reshape(Tfm(2,1,:),1,N); %input impedance
V_in_tl = ones(1,N);
I_in_tl = V_in_tl./Z_in_tl;

Pin = (V_in_tl.*conj(I_in_tl));

%transfer functions
Htx = reshape(1./Tfm(1,1,:),1,N);
Hrx = reshape(1./Trm(1,1,:),1,N);

%Acoustic Power generated
F2 = (V_in_tl.*Htx);
V2 = (F2.*Hrx);
Pa = (F2.*conj(F2))/(Z2*(a*lambda0)^2);
Pr = V2.*conj(V2)./Z_in_tl;

conv_eff = Pr./Pin;
conv_db = 10*log10(abs(conv_eff));
conv_loss(jj) = -10*log10(abs(max(conv_eff)));
bwl = f(find(conv_db>max(conv_db)-3,1,'first'));
bwh = f(find(conv_db>max(conv_db)-3,1,'last'));
bw=bwh-bwl;
%% Intrinsic Material Loss
at_10 = 4000; %dB/m, attenuation at 10 GHz
at_f = at_10/(10e9)^2; %dB/(m*hz^2)

at = at_f*f0^2;

%loss due to attenuation
at_loss(jj) = at*t_silicon; %dB

%% total loss
total_loss(jj) = DL(jj)+conv_loss(jj)+at_loss(jj);

%% noise sources
%acoustic noise
K = 1.38e-23; %J/K
T = 300; %room temperature (K)
R_silicon = 1.17404e7*(a*lambda0)^2;
f_n_2 = 4*K*T*R_silicon; %Fn/Hz

Vrn_f = abs(Hrx).^2*f_n_2.*abs(Rl./(Rl+Z_in_tl)).^2;

V_n_a = sum(Vrn_f)*(f(2)-f(1));

```

```

V_n_rl = 4*K*T*Rl*(bw);

V_n_total = V_n_a + V_n_rl;

P_n_total = V_n_total/Rl;

P_db = 10*log10(P_n_total);

P_sig_min = P_n_total;
P_in_min(jj) = P_sig_min*10^(total_loss(jj)/10);
M = 10000;
P_ins(jj,:) = linspace(P_in_min(jj),100*P_in_min(jj),M);
SNR = (P_ins(jj,:)*10^(-total_loss(jj)/10))/P_sig_min;
BER(jj,:) = 0.5*erfc(sqrt(SNR));
end
loglog(P_ins(1,:),BER(1,:), 'b')
hold on
loglog(P_ins(2,:),BER(2,:), 'r')
loglog(P_ins(3,:),BER(3,:), 'g')
loglog(P_ins(4,:),BER(4,:), 'm')
xlabel('Input Power (Watts)')
ylabel('Bit Error Rate')
legend('0.5 GHz', '1 GHz', '5 GHz', '10 GHz');

```

Chapter 10 References

- [1] C. Batten, et al. “Designing Chip-Level Nanophotonic Interconnection Networks”, IEEE Journal on Emerging and Selected Topics in Circuits and Systems, Vol. 2, No. 2, June 2012
- [2] G. M. Amdahl, “Validity of the Single Processor Approach to Achieving Large Scale Computing Capabilities” AFIPS Conference Proceedings, Vol. 30, pp 483-485, 1967
- [3] J. W. Goodman et al. “Optical Interconnections for VLSI Systems” Proceedings of the IEEE, Vol. 72, No. 7, July 1984
- [4] National Technology Roadmap for Semiconductors: Semiconductor Industry Association, 1997
- [5] K. C. Saraswat and F. Mohammadi, “Effect of Scaling of Interconnections on the Time Delay of VLSI Circuits” IEEE Transactions on Electron Devices, vol. ED-29, No. 4, April 1982
- [6] M. T. Bohr, “Interconnect Scaling – The Real Limiter to High Performance ULSI” IEDM 1995, pp. 241-244
- [7] D. Sylbester and K. Keutzer, “A Global Wiring Paradigm for Deep Submicron Design” IEEE Transactions on Computer Aided Design of Integrated Circuits and Systems, Vol. 19, No. 2, Feb 2000
- [8] R. Ho, et al. “The Future of Wires” Proceedings of the IEEE, Vol. 89, No. 4, April 2001
- [9] Picture from Computer History Museum, 1401 N Shoreline Blvd. Mountain View CA, obtain from <http://ed-thelen.org/comp-hist/vs-univac-mercury-memory.jpg>
- [10] W. Shockley “Semiconductor Amplifier” U.S. Patent 2,502,488 (filed: 24 Sept 1948, issued: 4 April 1950)
- [11] P. Eckstein, ‘Jack Kilby (1923-2005),’ Annals of the History of Computing, IEEE, Vol. 29 Issue 1, pp. 90-95, 2007

- [12] R. Slater 'Portraits in Silicon', Robert Noyce pages: 152-161, MIT Press eBook Chapters, 1989
- [13] Robert N. Noyce "Semiconductor Device-and-Lead Structure" U.S. Patent 2,981,877 (filed: 30 July 1959, issued: 25 April 1961)
- [14] W. M. Kaufman and S. Garrett, "Tapered Distributed Filters" IRE Transactions on Circuit Theory 1962, Vol 9, Issue 4, pages 329-336
- [15] R. H. Dennard et al. "Design of Ion-Implanted MOSFETs with Very Small Physical Dimensions" IEEE Journal of Solid-State Circuits 1974, Vol. 9, Issue 5, pages: 256-268
- [16] R. W. Keyes "The Evolution of Digital Electronics Towards VLSI" IEEE Transactions on Electron Devices, Vol. ED-26, No. 4, April 1979
- [17] D. A. B. Miller and H. M. Ozaktas, "Limit to the Bit-Rate Capacity of Electrical Interconnects from an Aspect Ratio of the System Architecture" Journal of Parallel and Distributed Computing 41, 42-52 1997, Article No. PC961285
- [18] D. Sylvester and K. Keutzer, "Getting to the Bottom of Deep Submicron" IEEE/ACM International Conference on Computer-Aided Design, 1998, pp 203-211
- [19] IARPA Trusted Integrated Circuits (TIC) Program
- [20] E. Mensink, et al. "Power Efficient Gigabit Communication Over Capacitively Driven RC-Limited On-Chip Interconnects" IEEE Journal of Solid-State Circuits, vol. 45, No. 2, February 2010
- [21] T. H. Maiman, "Stimulated Optical Radiation in Ruby" Nature **187**, 493-494 (06 August 1960)
- [22] K. C. Kao, "Dielectric-fibre surface waveguide for optical frequencies" Proc. IEEE, Vol. 113, No. 7, July 1966
- [23] S. E. Miller "Integrated Optics: An Introduction" The Bell System Technical Journal, Vol. 48, No. 7, September 1969

- [24] D. A. B. Miller, "Device Requirements for Optical Interconnects to Silicon Chips" Proceedings of the IEEE, Vol. 97, No. 7, July 2009
- [25] J. H. Collet et. al. "Performance Constraints for Onchip Optical Interconnects" IEEE Journal of Selected Topics in Quantum Electronics, Vol. 9, No. 2 March/April 2003
- [26] G. Tosik et al, "Clock Skew Analysis in Optical Clock Distribution Network" CADSM 2007, Poyana UKRAINE, February 20-24, 2007
- [27] M. S. Bakir and James D. Meindl "Integrated Interconnect Technologies for 3D Nanoelectronic Systems" Artech House, 2009 685 Canton Street, Norwood MA 02062
- [28] M.C.F. Chang, et al. "RF/Wireless Interconnect for Inter- and Intra-Chip Communication" Proceedings of the IEEE, Vol. 89, No. 4, April 2001
- [29] Y. Kim, et al. "Analysis of Noncoherent ASK Modulation-Based RF-Interconnect for Memory Interface" IEEE Journal on Emerging and Selected Topics in Circuits and Systems, Vol. 2, No. 2, June 2012
- [30] D. Zhao et al. "Design of Wireless Test Control Network With Radio-On-Chip Technology for Nanometer System-on-a-chip" IEEE Transactions on Computer-Aided Design of Integrated Circuits and Systems, Vol. 25, No. 7, July 2006
- [31] H.S. Yeh and K. L. Mende "Development of 60-GHz Wireless Interconnects for Interchip Data Transmission" IEEE Transactions on Components, Packaging, and Manufacturing Technology, Vol. 3, No. 11, November 2013
- [32] R. H. Olsson III, et. al., "Post-CMOS Compatible Aluminum Nitride MEMS Filters and Resonant Sensors" 2007 IEEE EFTFs, pp. 412-419
- [33] Francis Galton "Inquiries into Human Faculty and its Development," First Electronic Edition 2001, Original Print Macmillian 1883
- [34] Lord Rayleigh, John William Strutt, "The Theory of Sound", vol. II Chapter xxi, 1896

- [35] E.N. Da C. Andrade, "The Sensitive Flame" The Proceedings of the Physical Society Vol. 53, Part 4 no. 298 Twenty Fifth Guthrie Lecture, 1941
- [36] Image from: The University of Sydney, School of Psychology, Alison Turtle Memorial Psychology Collection; http://www.psych.usyd.edu.au/museum/alison_turtle_museum/collectionA.shtml
- [37] "Developpement par compression de l'electricite polaire dans les cristaux hemiedres a faces inclines" Bulletin de la Societe minerologique de France, vol. 3 pages 90-93.
- [38] "Principe de la conservation de l'electricite" Annals de chimie et de physique 24: 145
- [39] "Contractions et dilations produites par des tensions dans les cristaux hemiedres a faces inclines" Comptes rendus..., vol. 93, pages 1137-1140
- [40] Voigt *Lehrbuch der Kristallphysik* Berlin, Germany: B. G. Teubner, 1910.
- [41] W. P. Mason, "Uses of Ultrasonics in Radio, Radar, and Sonar Systems" Proceedings of the IRE, 1961, pp 1374-1384
- [42] W. Mason "Professor Walter G. Cady's contributions to piezoelectricity and what followed from them" J. Acoust. Soc. Am., Vol. 58, No. 2, August 1975
- [43] Walter G. Cady "Piezo-electric Resonator" U.S. Patent 1,450,246 (filed: 28 Jan 1920, issued: 3 April 1923)
- [44] W. G. Cady "The Piezoelectric resonator" Phys Rev A 1921;17:521-2
- [45] W. G. Cady "The piezo-electric resonator" Proc. IRE 1922;10:83-114
- [46] A. G. Emslie and R. L. McConnel, "Radar Systems Engineering," McGraw-Hill Book Co., Inc., New York, N. Y., vol. 1, ch. 16; 1947
- [47] Eckstein, P. "J. Presper Eckert" *IEEE Annals of the History of Computing*, Vol. 18, No. 1, 1996
- [48] J. M. Stanley "The Signal Corps Synthetic Quartz Program" IRE Trans. On Military Electronics, vol. MIL-4, pp. 438-447; October, 1960.

- [49] K. M. Lakin, J. S. Wang, G. R. Kline, A. R. Landin, and J. D. Hunt, "Thin film Resonators and filters," in Proc. IEEE Ultrason. Symp., 1982, p. 466
- [50] W. P. Mason "Electromechanical Transducers and Wave Filters" D. Van Nostrand Company, Inc New York 1942
- [51] T. R. Sliker and D. A. Roberts "A Thin-Film CdS-Quartz Composite Resonator" Journal of Applied Physics **38**, 2350 (1967)
- [52] D. J. Page "A Cadmium Sulfide-Silicon Composite Resonator", Proceedings of the IEEE, 56, pp 1748-1749, October 1968
- [53] R. Ruby and P. Merchant, "Micromachined Thin Film Bulk Acoustic Resonators," IEEE International Frequency Control Symposium, 1994
- [54] J. D. Larson et al. "A BAW Antenna Duplexer for the 1900 MHz PCS Band," IEEE Ultrasonics Symposium, p. 887-890, 1999
- [55] J. V. Rajendran, et al. "Is Split Manufacturing Secure?" *Design, Automation & Test in Europe Conference & Exhibition (DATE)*, pages 1259-1264, 2013
- [56] S. Mitra, "Stopping Hardware Trojans in Their Tracks" IEEE Spectrum, Posted 20 Jan 2015, retrieved 10 Nov 2015, <http://spectrum.ieee.org/semiconductors/design/stopping-hardware-trojans-in-their-tracks>
- [57] J. A. Roy et al. "EPIC: Ending Piracy of Integrated Circuits" *Proc. Of Design, Automation and Test in Europe*, pages 1069-1074, 2008
- [58] R. S. Chakraborty, "HARPOON: An Obfuscation-Based SoC Design Methodology for Hardware Protection" IEEE Transactions on Computer-Aided Design of Integrated Circuits and Systems, Vol. 28, No. 10, October 2009
- [59] S. Adee, "The Hunt for the Kill Switch" IEEE Spectrum, Posted 1 May 2008, retrieved 10 Nov 2015, <http://spectrum.ieee.org/semiconductors/design/the-hunt-for-the-kill-switch>

- [60] D. Sawyer “Counterfeit threat taking malicious turn?” Military Embedded Systems Article, Retrieved 11 Nov 2015, <http://mil-embedded.com/articles/counterfeit-taking-malicious-turn/>
- [61] Defence Advanced Research Projects Agency. Trusted Integrated Circuits (TRUST) Program <http://www.darpa.mil/program/trusted-integrated-circuits>
- [62] Intelligence Advanced Research Projects Agency. Trusted Integrated Circuits (TIC) Program <http://www.iarpa.gov/index.php/research-programs/tic>
- [63] J. A. Carballo, et al. “ITRS 2.0: Toward a re-framing of the semiconductor Technology Roadmap” 32nd IEEE International Conference on Computer Design (ICCD) 2014
- [64] W. P. Mason “Electromechanical Transducers and Wave Filters” D. Van Nostrand Company, Inc. New York, New York, 250 Fourth Avenue 1942
- [65] Lord Rayleigh, John William Strutt, “The Theory of Sound”, vol I-II, 1896
- [66] A.E.H. Love, “The Propagation of Wave-Motion in an Isotropic Elastic Solid Medium” Proc. London Math Soc. 1904
- [67] H. Lamb, “On the Propagation of Tremors over the Surface of an Elastic Solid” Philosophical Transactions of the Royal Society A, 1903
- [68] R. D. Oldham “The Constitution of the Interior of the Earth as revealed by Earthquakes” The Quarterly Journal of Geological Society of London Vol. 62, 1906 pp 456-475
- [69] Kino, G. Acoustic Waves: Devices, Imaging and Analog Signal Processing Englewood Cliffs NY, Prentice Hall, 1987
- [70] Mason, Warren P., “6 - Effect of Impurities and Phonon Processes on the Ultrasonic Attenuation of Germanium, Crystal Quartz, and Silicon”, In: WARREN P. MASON, Editor(s), Physical Acoustics, Academic Press, 1965, Volume 3, Part B, Pages 235-286, ISSN 0893-388X, ISBN 9780123956699, <http://dx.doi.org/10.1016/B978-0-12-395669-9.50013-8>.
(<http://www.sciencedirect.com/science/article/pii/B9780123956699500138>)

- [71] Q. Chen, "Property characterization of AlN thin films in composite resonator structure" *Journal of Applied Physics* **101**, 084103 (2007)
- [72] H. Zhang, "High-tone bulk acoustic resonators on sapphire, crystal quartz, fused silica, and silicon substrates" *Journal of Applied Physics* **99** 124911 (2006)
- [73] S.E. Park and T. R. ShROUT, "Characteristics of Relaxor-Based Piezoelectric Single Crystals for Ultrasonic Transducers" *IEEE Transactions on Ultrasonics, Ferroelectrics, and Frequency Control*, Vol. 44, No. 5, September 1997
- [74] M. Redwood "Transient performance of a piezoelectric transducer", *J. Acoust. Soc. Amer.*, 1961, 33, pp. 527-536
- [75] R. Krimholtz, D. A. Leedom, and G. L. Matthaei, "New Equivalent Circuits for Elementary Piezoelectric Transducer", *Electronics Letters*, 25th June 1970, Vol. 6, No. 13
- [76] "Aluminum Nitride (AlN) RF MEMS Resonator Design Manual", SANDIA National Labs, Albuquerque, NM, Rev 1.4, 2012
- [77] J. Hoople et al. "Optimized Response of AlN Stack for Chipscale GHz Ultrasonics" *IEEE International Ultrasonics Symposium*, October 2015
- [78] C. G. Oakley, "Calculation of Ultrasonic Transducer Signal-to-Noise Ratios Using the KLM Model" *IEEE Transactions on Ultrasonics Ferroelectrics, and Frequency Control*, Vol. 44, No. 5, September 1997
- [79] T. L. Rhyne, "Characterizing Ultrasonic Transducers Using Radiation Efficiency and Reception Noise Figure" *IEEE Transactions on Ultrasonics, Ferroelectrics, and Frequency Control*, Vol. 45, No.. 3, May 1998
- [80] Balanis, C. *Antenna Theory and Design* Hoboken NJ, John Wiley & Sons Inc. 2005
- [81] Cobbold, R. *Foundations of Biomedical Ultrasound* New York, New York, Oxford University Press, Inc. 2007

- [82] Archel-Hall, J. A. and Gee, D. "Computing particle velocity and intensity in diffracting systems", *Ultrasonics*, Volume 20, Issue 5, September 1982, Pages 224-230, ISSN 0041-624X
- [83] M. Skolnik, *Introduction to Radar Systems*, McGraw-Hill 1962
- [84] Hodges, D. et al. *Analysis and Design of Digital Integrated Circuits in Deep Submicron Technology* New York NY, McGraw-Hill 2004
- [85] B. Kim and V. Stojanovic, "Equalized Interconnects for On-Chip Networks: Modeling and Optimization Framework" *Computer-Aided Design*, 2007. ICCAD 2007
- [86] S. Manipatruni, et al. "Device Scaling Considerations for Nanophotonic CMOS Global Interconnects" *IEEE Journal of Selected Topics in Quantum Electronics*, Vol. 19, No.2, March/April 2013
- [87] Hopcroft, M. A., et. al. "What is the Young's Modulus of Silicon?" *Journal of Microelectromechanical Systems*, Vol.. 19, No. 2, April 2010
- [88] T. H. Lee *The Design of CMOS Radio-Frequency Integrated Circuits 2nd Edition* Cambridge, United Kingdom, The Press Syndicate of the University of Cambridge
- [89] K. V. Larin and Y. Cheng, "Three-dimensional imaging of artificial fingerprint by Optical Coherence Tomography," in *Biometric Technology for Human Identification V, March 18, 2008 - March 19, 2008*, Orlando, FL, United states, 2008, pp. The Society of Photo-Optical Instrumentation Engineers (SPIE).
- [90] S. Palka and B. A. Hamilton, "Fingerprint readers: vulnerabilities to front-and back-end attacks," in *2007 First IEEE International Conference on Biometrics: Theory, Applications, and Systems - BTAS '07, 27-29 Sept. 2007*, Piscataway, NJ, USA, 2007, pp. 142-6.
- [91] C. W. Tsai, P. J. Wang, and J. A. Yeh, "Compact touchless fingerprint reader based on digital variable- Focus liquid lens," in *17th Conference of Novel Optical Systems Design and Optimization, August 17, 2014 - August 19, 2014*, San Diego,

CA, United states, 2014, pp. The Society of Photo-Optical Instrumentation Engineers (SPIE).

- [92] C. Harrison, M. Sato, and I. Poupyrev, "Capacitive fingerprinting: Exploring user differentiation by sensing electrical properties of the human body," in *25th Annual ACM Symposium on User Interface Software and Technology, UIST 2012, October 7, 2012 - October 10, 2012*, Cambridge, MA, United states, 2012, pp. 537-543.
- [93] S. Meng-Lieh, L. Chih-Kuan, H. Wei-Hung, and Y. Hong-Ming, "A novel capacitive sensing scheme for fingerprint acquisition," in *2005 IEEE Conference on Electron Devices and Solid-State Circuits, 19-21 Dec. 2005*, Piscataway, NJ, USA, 2005, pp. 627-30.
- [94] T. Shimamura, H. Morimura, S. Shigematsu, M. Nakanishi, and K. Machida, "Capacitive-Sensing Circuit Technique for Image Quality Improvement on Fingerprint Sensor LSIs," *IEEE Journal of Solid-State Circuits*, vol. 45, pp. 1080-7, 05/ 2010.
- [95] N. Shimoyama, S. Shigematsu, H. Morimura, T. Shimamura, T. Kumazaki, M. Nakanishi, *et al.*, "Effect of scratch stress on the surface hardness and inner structures of a capacitive fingerprint sensor LSI," in *2007 IEEE International Reliability Physics Symposium Proceedings, 15-19 April 2007*, Piscataway, NJ, USA, 2007, p. 5 pp.
- [96] W. Bicz, D. Banasiak, P. Bruciak, Z. Gumienny, S. Gumulinski, D. Kosz, *et al.*, "Ultrasonic camera for finger ridge pattern imaging," *Archives of Acoustics*, vol. 23, pp. 139-48, / 1998.
- [97] A. Iula, A. Savoia, and G. Caliano, "Capacitive micro-fabricated ultrasonic transducers for biometric applications," *Microelectronic Engineering*, vol. 88, pp. 2278-80, 08/ 2011.
- [98] Y. Lu, H. Tang, S. Fung, Q. Wang, J. M. Tsai, M. Daneman, *et al.*, "Ultrasonic fingerprint sensor using a piezoelectric micromachined ultrasonic transducer array

- integrated with complementary metal oxide semiconductor electronics," *Applied Physics Letters*, vol. 106, p. 263503 (4 pp.), 06/29 2015.
- [99] A. Maeva and F. Severin, "High Resolution Ultrasonic Method for 3D Fingerprint Recognizable Characteristics In Biometrics Identification," in *2009 IEEE International Ultrasonics Symposium, 20-23 Sept. 2009*, Piscataway, NJ, USA, 2009, pp. 2260-3.
- [100] H. Tang, Y. Lu, S. Fung, J. M. Tsai, M. Daneman, D. A. Horsley, *et al.*, "Pulse-echo ultrasonic fingerprint sensor on a chip," in *2015 Transducers - 18th International Conference on Solid-State Sensors, Actuators and Microsystems (TRANSDUCERS), 21-25 June 2015*, Piscataway, NJ, USA, 2015, pp. 674-7.
- [101] Sonavation, www.sonavation.com
- [102] Qualcomm, www.qualcomm.com/products/snapdragon/security/sense-id
- [103] J. Hoople, J. Kuo, S. Ardanuc, and A. Lal, "Chip-scale sonic communication using AlN transducers," in *Ultrasonics Symposium (IUS), 2013 IEEE International*, 2013, pp. 1934-1937.
- [104] J. Hoople, J. Kuo, S. Ardanuc, and A. Lal, "Chip-scale reconfigurable phased-array sonic communication," in *Ultrasonics Symposium (IUS), 2014 IEEE International*, 2014, pp. 479-482.
- [105] J. Kuo, J. Hoople, S. Ardanuc, and A. Lal, "Towards ultrasonic through-silicon vias (UTSV)," in *Ultrasonics Symposium (IUS), 2014 IEEE International*, 2014, pp. 483-486.
- [106] A. Lal, S. Ardanuc, J. Hoople, and J. Kuo, "COMPUTATION DEVICES AND ARTIFICIAL NEURONS BASED ON NANO-ELECTROMECHANICAL SYSTEMS ", 2014.
- [107] A. Briggs and O. Kolosov, *Acoustic Microscopy*: Oxford, 2009.
- [108] <http://www.quran-m.com/firas/en1/index.php/human/197-fingerprints-and-the-human-identity.html>